UNIVERSIDAD POLITÉCNICA DE MADRID
Escuela Técnica Superior de Ingenieros de Telecomunicación

Solidly Mounted Resonator gas sensors for harsh environment applications

TESIS DOCTORAL

Presentada para optar al título de Doctor por:

José Manuel Carmona Cejas
Máster en Nanofísica y Materiales Avanzados

Madrid, 2024

UNIVERSIDAD POLITÉCNICA DE MADRID
Escuela Técnica Superior de Ingenieros de Telecomunicación

Doctorado en Ingeniería de Sistemas Electrónicos

Solidly Mounted Resonator gas sensors for harsh environment applications

TESIS DOCTORAL

Presentada para optar al título de Doctor por:

José Manuel Carmona Cejas
Máster en Nanofísica y Materiales Avanzados

Bajo la dirección de:
Dra. Jimena Olivares Roza (Directora)
Dra. Teona Mirea (Directora)

Madrid, 2024

Título: Solidly Mounted Resonator gas sensors for harsh environments applications

Autor: José Manuel Carmona Cejas

Programa de Doctorado: Ingeniería de Sistemas Electrónicos

Dirección de tesis:

Dra. Jimena Olivares Roza, Profesora Titular del Dpto. de Ingenería Electrónica, Universidad Politécnica de Madrid (Directora)

Dra. Teona Mirea, Profesora Contratado Doctor del Dpto. de Ingeniería Electrónica, Universidad Politécnica de Madrid (Directora)

Revisores externos:

Tribunal de tesis:

Fecha de defensa:

Esta tesis ha sido parcialmente financiada por Ministerio de Ciencia e Innovación de España y Agencia Estatal de Investigación a través de los proyectos TEC2017-84817-C2-1-R y PID2020-118410RB-C22. El contrato predoctoral PRE2018-086657, financiado por el Ministerio de Ciencia e Innovación de España, ha servido para contratar al doctorando durante el periodo de realización de la tesis doctoral. Una parte experimental de la tesis ha sido llevada a cabo en el Departamento de Ingeniería Eléctrica de la Universidad de Cambridge (UK), durante la estancia de investigación del doctorando (abril-julio de 2022).

"It is unimaginably hard to do this, to stay conscious and alive in the adult world day in and day out. Which means yet another grand cliché turns out to be true: your education really IS the job of a lifetime. And it commences: now.

I wish you way more than luck."

David Foster Wallace (1962-2008),
This Is Water: Some Thoughts, Delivered on a Significant Occasion, about Living a Compassionate Life, 2009.

Agradecimientos

Quienes me conocen saben que no soy una persona excesivamente planificadora y que siempre me ha gustado más fluir, tomar decisiones en función del momento vital en el que me encontraba y no pensar mucho en el largo plazo. Vamos, casi como una cadena de Markov. Este proceso de toma de decisiones trae consigo un problema del que no me había dado cuenta hasta ahora, y es que no te proporciona muchos momentos para reflexionar, para ser capaz de ver la imagen completa de tu vida, a nivel personal y profesional. Por eso, la escritura de esta tesis ha sido en cierto modo como una ruptura abrupta con la rutina, un tiempo en el que he podido organizar la investigación llevada a cabo durante este periodo, pero también un tiempo que me ha hecho ser consciente de quién me acompaña, y de a quién creo que necesito expresar mi gratitud en estas líneas.

Me gustaría empezar dando las gracias al GMME. Desde aquel día en el que me entrevistasteis para ofrecerme la FPI me habéis hecho sentir como en casa. Además de compañeros de trabajo, sois prácticamente mi familia aquí en Madrid y os agradezco enormemente la oportunidad que me brindasteis. Gracias a mis directoras, la Dra. Jimena Olivares y la Dra. Teona Mirea por los consejos, por haberme guiado, pero dándome libertad para construir mi propio camino. Me habéis ayudado muchísimo, incluso cuando pensabais que no lo estabais haciendo. Gracias a la Dra. Marta Clement, porque parte de esta tesis también es tuya. Gracias por nuestras discusiones sobre cocina, que sin duda han conseguido que eleve mi nivel de cocinillas. Si hoy me puedo considerar algo parecido a un investigador es gracias a vuestra inestimable ayuda. Gracias a Ricardo Hervás, por estar siempre disponible para echarme una mano en la sala limpia, por ser un manitas y ser capaz de arreglar prácticamente cualquier cosa. Por tomarnos una cerveza de vez en cuando y hablar de videojuegos o de boxeo. Por supuesto, me gustaría dar las gracias también al Dr. Jesús Sangrador y al Dr. Mario De Miguel por vuestro cariño y apoyo, pasar un rato con vosotros es siempre un placer y sois personas de las que tengo muchísimo que aprender. Por último, me gustaría dar las gracias al Dr. Enrique Iborra por haber sido pieza fundamental en la creación de todo este entorno en el que es tan fácil trabajar y convivir con los demás. Aunque no nos hayamos visto nunca, siento que te conozco y que esta tesis no habría sido posible sin ti.

I would like to thank Prof. Andrew Flewitt for receiving me and covering my clean room costs during my time in the University of Cambridge. Thank you for your supervision and guidance. I would also like to thank my friend Alkausil for helping

me with everything when I was around, and for cooking Chicken Biryani. Outside science, thank you to Fer and Rebe for showing me Cambridge and helping me settle. Thank you for being so kind to me. And of course, huge thanks to my friends Tina and Adri, for making me feel at home in Hammersmith.

Muchas gracias a mis amigos, a los de toda la vida, por apoyarme y por mantenerme con los pies en el suelo. Gracias a todo Vysy, por ser como sois y por acompañarme durante tanto tiempo. Gracias especialmente a Lomo, al Gome (y señora), a Borja, al Seillo y a Navajas, por ser los mejores amigos que se puede tener en la vida, porque estáis ahí para todo, y porque ya es muy tarde para descambiaros. Gracias Violeta por tu amistad, y por estar siempre dispuesta a apuntarte a un bombardeo.

Muchas gracias a los amigos que he hecho durante mi estancia en Madrid. Sobre todo, muchas gracias a los ex MS, con los que mantengo un vínculo especial, forjado en la torre más alta (Torre Picasso) de Mordor (Azca). Dani, muchas gracias por convertirte prácticamente en mi tutor y guía durante mi tiempo allí, y por compartir siempre que puedes un poquito de tu sabiduría, que es casi interminable, conmigo. Ve calentando, que a ti ya mismo te toca pasar por esto. Alberto, gracias por ser como eres, por tus llamadas desde el coche para ponernos al día y acabar hablando durante horas. Gracias por ser una de las mejores personas que conozco. Y, por supuestísimo, gracias a Paula, aunque contigo creo que la palabra gracias se queda corta. Desde el primer momento has sido increíblemente generosa, atenta y cariñosa conmigo, especialmente en los momentos que más lo necesito. Somos familia.

Hablando de familia, gracias a mi abuela Carmen y a mi abuela Conchi. Gracias por haberme criado, por estar siempre pendientes de mí cuando era un crío, por haberme dado de comer, por reñirme cuando me lo merecía y por consentirme un poco también. Gracias por haberme hecho callos, macarrones con chorizo, bizcocho, tarta de manzana o churros. Gracias por quererme incondicionalmente. A mi abuelo José y mi abuelo Manolo, gracias por ser mis referentes en la vida, por poder hablar de vosotros con todo el orgullo del mundo. Os debo mi nombre, y sé que es una tarea prácticamente imposible estar a la altura de semejantes artistas.

Gracias a mis tías y a mis tíos por querer tanto a su sobrino, aunque a veces no lo vean mucho. Gracias a mi tía Paqui por haber sido prácticamente una hermana mayor. Gracias a mi tío Antonio por escucharme. Gracias a mi tío Jose por alimentar mi curiosidad desde que era un enano, y por echarme una mano siempre que lo

necesito. Gracias también a mi primo Víctor, que para mí ha sido siempre como un hermano mayor.

Ah, se me olvidaba. Tengo que dar las gracias a mis abuelos por otra cosa que supieron hacer muy bien. Gracias por haber criado a mis padres, Pachi y Lola. Papá, mamá, gracias por educarme y por motivarme siempre a seguir mi propio camino. Gracias por enseñarme Cosmos, por escucharme con entusiasmo siempre que os hablo de cualquier cosa. Sois la principal razón de que hoy pueda estar aquí, y eso es algo que nunca os podré agradecer lo suficiente. Os quiero.

Y, por último, gracias a la persona más importante de mi vida. Maritere, gracias por haberme dado el último empujoncito para lanzarme al vacío, gracias por haberme acompañado a través de este camino (y por haberlo liderado casi todo el tiempo). Gracias por seguir mirándome con el mismo brillito en los ojos que cuando estudiábamos en Granada. Gracias por compartirlo todo conmigo. Te quiero más que al queso.

José Manuel Carmona Cejas
Madrid, marzo de 2024

Abstract

Sensors play a fundamental role in today's society as information gathering elements. Sensors exist for all types of applications, operating in numerous environments. However, developing devices capable of providing reliable detection and transmission of information when operating outside the typical room temperature conditions can be challenging. Thin film bulk acoustic resonators have been widely studied in the last decades as a transducer element for different types of sensors due to their versatility, high sensitivity, low fabrication cost and easy handling. Specifically, in their solidly mounted resonator (SMR) configurations, robustness, and the possibility to design a straightforward fabrication route are added to all the mentioned advantages.

The main objective of this thesis is to design, fabricate and characterize SMR based sensors for gas detection under harsh conditions, such as high and low temperature. To perform these experiments, the design, build, and test of an appropriate experimental setup is necessary. A gas injection system consisting of two characterization chambers, one for high temperature sensors (up to 450 °C) and one for low temperature sensors (reaching −40 °C) was developed. The experimental setup was subjected to use tests consisting of generating controlled atmospheres of ethanol vapors to characterize its detection with SMRs functionalized with carbon nanotube forests.

The study of the devices included in this thesis was first approached considering the involved materials. For this purpose, different configurations of acoustic reflectors were proposed: four based on dielectric materials (AlN/SiO_2, ZnO/SiO_2, Ta_2O_5/SiO_2 and HfN/SiO_2) and one alternating metallic and dielectric materials (Mo/SiO_2). SMRs were manufactured using these configurations to characterize their electrical response and acoustic insulation properties, together with their thermal behavior. Although fully dielectric reflectors show good performance, the devices intended for high temperature applications were manufactured on Mo/SiO_2 reflectors as they offer higher thermal stability. Potential electrodes were also studied, with particular emphasis on top electrodes for high temperature applications. To avoid potential oxidation issues, a Mo/Au is proposed, in which a thin Au layer plays the role of passivation layer. Moreover, AlN and $Al_{0.7}Sc_{0.3}N$ were assessed as piezoelectric materials. Despite showing better piezoelectric activity, $Al_{0.7}Sc_{0.3}N$ films lack the necessary thermal stability to be suitable for certain sensor applications or functionalization processes.

The proposed sensors in this thesis can be divided into three main categories depending on the operating temperature:

- Room temperature: detection of NO gas molecules was achieved using AlN-based SMRs functionalized with thermally evaporated pentacene layers, with sensitivity of 0.88 kHz/ppm.
- Low temperature: using dual mode SMRs, the possibility of discriminating temperature and humidity effects from the response of resonant frequencies was demonstrated, operating in the −20 °C to room temperature range.
- High temperature: AlN-based SMR sensors functionalized with sputtered WO_3 films were designed and characterized. The sensors are able to operate in the 200-350 °C range, and show high sensitivity towards NO gas molecules, achieving sensitivities even above 5 kHz/ppm, which leaves open the possibility to detect gas concentrations in the ppb range.

Resumen

En la sociedad actual, los sensores juegan un papel fundamental como elementos recopiladores de información. Existen sensores para todo tipo de aplicaciones, operando en ambientes muy diversos. Sin embargo, desarrollar dispositivos capaces de ofrecer detección y transmisión de la información fiables cuando nos alejamos de condiciones de temperatura ambiente supone todo un desafío. Los resonadores acústicos de película delgada han sido estudiados durante los últimos años como elemento transductor para distintas familias de sensores debido a su versatilidad, alta sensibilidad, bajo coste de fabricación y manejabilidad. Más específicamente, en su configuración sobre reflectores acústicos (SMR, *solidly mounted resonators*), a todas las ventajas mencionadas se suman la robustez y la posibilidad diseñar una ruta de fabricación sencilla.

El principal objetivo de esta tesis es diseñar, fabricar y caracterizar sensores basados en SMRs para aplicaciones de detección de gases en condiciones extremas, como las altas y bajas temperaturas. El otro gran objetivo es diseñar, construir y probar un sistema experimental que permita realizar la caracterización de dichos sensores. Para ello, se ha puesto a punto un sistema de inyección de gases que consta de dos cámaras independientes con entradas de gases reguladas con controladores de flujo para generar atmósferas controladas. La primera cámara se utiliza para la caracterización de los sensores a alta temperatura (hasta 450°C), mientras que en la otra se realiza la caracterización a baja temperatura (hasta −40°C). El montaje experimental fue sometido a pruebas de uso consistentes en generar atmósferas controladas de vapores de etanol para caracterizar su detección con SMRs funcionalizados con bosques de nanotubos de carbono.

El estudio de los dispositivos ha sido planteado primero desde el punto de vista de los materiales involucrados. Para ello, se han propuesto diferentes configuraciones de reflectores acústicos: cuatro basadas en materiales aislantes (AlN/SiO_2, ZnO/SiO_2, Ta_2O_5/SiO_2 y HfN/SiO_2) y una que alterna un metal y un aislante (Mo/SiO_2). Para caracterizarlos, se han fabricado SMRs usando estas configuraciones y se han medido sus respuestas eléctricas, su capacidad de aislamiento acústico y su comportamiento térmico. Aunque los reflectores basados en materiales aislantes ofrecen buen rendimiento, los sensores a alta temperatura se han fabricado sobre reflectores de Mo/SiO_2 debido a que ofrecen mayor estabilidad térmica. También se han estudiado los potenciales electrodos, con especial énfasis en el electrodo superior para las aplicaciones a alta temperatura.

Para evitar problemas de oxidación, se ha propuesto un electrodo de Mo/Au, en el que una fina capa de Au actúa como capa de pasivación. Por último, se han estudiado dos materiales piezoeléctricos: AlN y $Al_{0.7}Sc_{0.3}N$. Pese a ofrecer mejor actividad piezoeléctrica, las películas de $Al_{0.7}Sc_{0.3}N$ estudiadas ofrecen mayor inestabilidad al someterlas a altas temperaturas, lo que puede suponer un inconveniente para determinadas aplicaciones o procesos de funcionalización.

Los sensores propuestos en esta tesis se pueden dividir en tres categorías en función de la temperatura a la que operan:

- Temperatura ambiente: se ha detectado NO con SMRs basados en AlN funcionalizados con capas de pentaceno evaporado térmicamente, con una sensibilidad de 0.88 kHz/ppm.
- Baja temperatura: usando SMRs que presentan dos modos de resonancia, se han discriminado los efectos de la temperatura y la humedad sobre las frecuencias de resonancia, operando entre $-20°C$ y temperatura ambiente.
- Alta temperatura: se han diseñado y caracterizado sensores basados en SMRs de AlN funcionalizados con capas de WO_3 depositadas por pulverización catódica. Estos sensores operan en el rango entre 200 y 350°C, y ofrecen gran sensibilidad para detectar NO con valores por encima de 5 kHz/ppm, lo que deja abierta la posibilidad a detectar concentraciones de gas en el rango de las ppb.

Publicaciones

Artículos en revistas indexadas

i. **J. M. Carmona-Cejas,** T. Mirea, J. Nieto, J. Olivares, V. Felmetsger and M. Clement, "Homogeneity and Thermal Stability of Sputtered $Al_{0.7}Sc_{0.3}N$ Thin Films," *Materials*, vol. 16, no. 6, 2169, Mar. 2023, doi: 10.3390/ma16062169.

ii. **J. M. Carmona-Cejas,** T. Mirea, R. Hervás-García, J. Olivares and M. Clement, "Dual-mode SMR-based sensor for discriminating temperature humidity effects," *Sensors,* 2024 (under review).

iii. **J. M. Carmona-Cejas,** T. Mirea, J. Olivares, R. Hervás-García and M. Clement, "AlN-based Solid Mounted Resonators functionalized with WO_3 films for NO detection," *Sens. and Actuators B: Chem.*, 2024 (under review).

iv. E. Lugo-Hernández, T. Mirea, **J. M. Carmona-Cejas,** M. Clement, J. Olivares, J. C. Collado and J. Mateu, "Analysis of spurious peaks at series resonance in solidly mounted resonators by combined BVD-Mason modelling," *Ultrasonics*, vol. 131, 106958, May 2023, doi: 10.1016/j.ultras.2023.106958

Trabajos presentados a congresos

i. **J. M. Carmona-Cejas,** T. Mirea, M. Clement and J. Olivares, "Comparative study of fully-dielectric acoustic reflectors in solidly mounted resonators" *IEEE Intern. Ultrason. Symp., IUS*, Virtual, Sept. 2021, doi: 10.1109/IUS52206.2021.9593421. **(póster)**

ii. **J. M. Carmona-Cejas,** T. Mirea, J. Nieto, J. Olivares, V. Felmetsger and M. Clement, "Temperature stability of $Al_{0.7}Sc_{0.3}N$ sputtered thin films," *IEEE Intern. Ultrason. Symp., IUS*, Virtual, Sept. 2021, doi: 10.1109/IUS52206.2021.9593320. **(oral)**

iii. E. Lugo-Hernández, T. Mirea, **J. M. Carmona-Cejas,** M. Clement, J. Olivares, J. C. Collado and J. Mateu, "High temperatures BVD model for AlN-based solidly mounted resonators," *IEEE Intern. Ultrason. Symp., IUS*, Virtual, Sept. 2021, doi: 10.1109/IUS52206.2021.9593400. **(póster)**

iv. E. Lugo-Hernandez, C. Collado, J. Mateu, T. Mirea, T., **J. M. Carmona-Cejas,** M. Clement and J. Olivares, "Modified Mason's and BVD Models For Analysis of Spurious Modes Due To Ohmic Losses in BAW Resonators," *2021 Joint Conf. of the European Freq. and Time Forum and IEEE Intern. Freq. Control Symp., EFTF/IFCS 2021*, Virtual, Apr. 2021, doi: 10.1109/EFTF/IFCS52194.2021.9604279. **(póster)**

v. **J. M. Carmona-Cejas,** T. Mirea, M. Clement and J. Olivares, "Solidly Mounted Resonators Based on ZnO/SiO_2 Acoustic Reflectors and Their Performance After High-temperature Exposure," *2022 Joint Conf. of the European Freq. and Time Forum and IEEE Intern. Freq. Control Symp., EFTF/IFCS 2022*, París, France, Apr. 2022 doi: 10.1109/EFTF/IFCS54560.2022.9850963. **(póster)**

vi. E. Lugo-Hernandez, C. Collado, J. Mateu, **J. M. Carmona-Cejas,** T. Mirea and J. Olivares, "Updated BVD Modeling of AlN-based Solidly Mounted Resonators Working at Cryogenic and High Temperatures: From-160 °C up to 130 °C," *2022 Joint Conf. of the European Freq. and Time Forum and IEEE Intern. Freq. Control Symp., EFTF/IFCS 2022*, París, France, Apr. 2022, doi: 10.1109/EFTF/IFCS54560.2022.9850489. **(póster)**

vii. **J. M. Carmona-Cejas,** T. Mirea, R. Garcia-Hervas, M. Moreno, M. de Miguel-Ramos, J. Olivares and M. Clement, "Decoupling of Humidity and Temperature Effects with a single Solidly Mounted Resonator Sensor," *IEEE Intern. Ultrason. Symp., IUS,* Venice, Italy, Oct. 2022, doi: 10.1109/IUS54386.2022.9957176. **(póster)**

viii. **J. M. Carmona-Cejas,** T. Mirea, R. Garcia-Hervas, J. Olivares and M. Clement, "Film bulk acoustic resonators for nitrogen monoxide detection at 250˚C," *Eurosensors XXXIV*, Lecce, Italy, Sept. 2023. **(póster)**

ix. **J. M. Carmona-Cejas,** T. Mirea, R. Garcia-Hervas, J. Olivares and M. Clement, "Nitrogen monoxide detection with pentacene based film bulk acoustic resonators," *Eurosensors XXXIV*, Lecce, Italy, Sept. 2023. **(oral)**

Índice

Lista de Figuras

Lista de Tablas

Abreviaturas y acrónimos

EA	Electroacoustic
QCM	Quartz Crystal Microbalance
BAW	Bulk Acoustic Wave
SAW	Surface Acoustic Wave
TSM	Thickness Shear Mode
FBAR	Film Bulk Acoustic Resonator
SMR	Solidly Mounted Resonator
IDT	Interdigital Transducer
LWR	Lamb Wave Resonator
SH-SAW	Shear Horizontal SAW
HBAR	High Overtone Bulk Acoustic Resonator
TCF	Temperature Coefficient of Frequency
HCF	Humidity Coefficient of Frequency
PVD	Physical Vapor Deposition
HiTUS	High Target Utilization Sputtering
CVD	Chemical Vapor Deposition
CNT	Carbon Nanotube
RIE	Reactive Ion Etching
XRD	X-Ray Diffraction
FWHM	Full Width at Half Maximum
RC	Rocking Curve
XRR	X-Ray Reflectometry
RBS	Rutherford Backscattering Spectroscopy
AFM	Atomic Force Microscopy
SEM	Scanning Electron Microscopy
VNA	Vector Network Analyzer

MFC	Mass Flow Controller
NP	Nanoparticle

1

INTRODUCTION

Sensors are devices capable of responding to a physical stimulus and translating it into measurable signals, which can be interpreted by a readout system. For instance, the necessity of determining how hot or how cold things are led to the invention of the thermometer, an instrument that, apart from its main purpose, has significantly influenced numerous scientific advances throughout history [1]. Today, sensor devices are present in nearly every aspect of our lives, as the applications where they can be found are almost limitless: from pressure [2], temperature [3] and humidity control [4], to detection of chemical species in different sectors such as food industry [5], waste management [6] or in the monitorization of products in industrial processes [7]. Healthcare is another sector in which the relevance of sensing technologies has spiked up over the years, as they can be developed to detect many biological species that would help in the diagnosis of diseases and in drug development and testing [8].

Depending on their work principle, a wide range of different types of sensors can be considered for the abovementioned applications. Capacitive, conductive, and inductive sensors see their electrical properties modified when exposed to the desired target [9]–[11], same as resistive sensors and their electrical resistance [12]. Optical sensors usually take advantage of the changes in refraction index of the active area [13], i.e., the part of the sensor that interacts with the target or physical stimulus we are interested in. Photovoltaic sensors experience a change in voltage when they are illuminated with light of a certain energy [14], whereas photoconductive sensors experience a change in their resistance based on the light they are exposed to [15]. Acoustic energy can also be exploited as the basis to build a sensor, since, when confined in a structure, it can be affected by the interaction with external factors and such changes can be monitored. Thus, the resulting acoustic devices can offer quick response, high sensitivity, small size, and low

production costs, which are some of the most attractive properties for such a demanding and growing sector.

Electroacoustic (EA) resonators can be functionalized in numerous ways, making them ideal candidates as transducers for different types of sensors. These devices present a characteristic called resonance, by which they vibrate at a known frequency. When the functionalization layer interacts with the target analyte, this frequency experiences a shift that can be measured, which results in a functional sensor. From temperature and humidity [16], [17], to biochemical [18] and gas species [19], [20], EA resonators have been widely studied in sensor applications during the last decades. In this thesis, the focus is put on their ability to work as gas sensors, with special consideration in their potential operation under harsh conditions, such as low or high temperature environments.

1.1. ELECTROACOUSTIC DEVICES

1.1.1. Piezoelectric effect and acoustic waves

Acoustic waves are a type of mechanical waves that travel through a medium by the movement of its atoms These waves can travel in both longitudinal and transverse modes when propagating through a solid medium. Acoustic waves can be generated when an electric field is applied to a certain type of material by means of the (reverse) piezoelectric effect. These materials are called piezoelectric materials, and they are the main components in an EA device.

The piezoelectric effect can be described as the ability of a material to generate an electric field when being mechanically deformed. When the opposite happens, it is called reverse piezoelectric effect. A brief microscopic explanation would be that the crystalline structure of a piezoelectric material should manifest a lattice asymmetry such that it would let a mechanical deformation create electric dipoles. Their dipolar momentum would not annihilate each other and thus an electric field would be generated. Macroscopically, this effect can be explained by combining Hooke's Law and Maxwell's constitutive equation [21]:

$$T = cS - eE \tag{1.1}$$

$$D = \epsilon E + eS \tag{1.2}$$

where T is the stress (force), c is the stiffness tensor, S is the strain, E is the electric field, D is the electric displacement, ϵ is the electrical permittivity tensor and e is the piezoelectric stress tensor. When the parameters of the equations are measured at constant electrical field and strain, they are denoted as c^E and ϵ^S. The coupling term, i.e., the part of the equations describing the piezoelectric effect, is the part multiplied by e in each case. To quantify the conversion rate between mechanical and electrical energy, we can define the electromechanical coupling factor, k^2, from the parameters introduced in equations 1.1 and 1.2. The idea behind this quantity is to find the following ratio [22]:

$$k^2 = (\text{Stored mechanical energy}/\text{Input electrical energy}) \tag{1.3}$$

This ratio can also be expressed when the opposite happens. In the case of eq. 1.3, when an electric field E is applied to a piezoelectric material, the electrical energy per unit volume is described as

$$\text{Input electrical energy} = \frac{1}{2}\epsilon^S \mathrm{E}^2 \tag{1.4}$$

and the mechanical energy per unit volume can be described as

$$\text{Stored mechanical energy} = \frac{1}{2}\frac{(\mathrm{dE})^2}{\mathrm{c}^\mathrm{E}} \tag{1.5}$$

By combining both expressions:

$$k^2 = \left(\frac{1}{2}\frac{(\mathrm{dE})^2}{\mathrm{c}^\mathrm{E}}\right)\Big/\left(\frac{1}{2}\epsilon^S \mathrm{E}^2\right) = \frac{\mathrm{e}^2}{\mathrm{c}\cdot\epsilon} \tag{1.6}$$

Since e, c and ϵ are tensors, the value of k^2 depends on the direction of the applied fields. In our case, since our devices will mainly display longitudinal modes, the most important coefficients will be the ones attached to this type of mode. In the case of the piezoelectric tensor, this will be the e_{33} coefficient.

When the acoustic waves are generated within the piezoelectric material, their propagation can be studied combining the following equations:

Newton's second law: $$\mathrm{F} = \mathrm{ma} \tag{1.7}$$

Particle velocity: $$\mathrm{v} = \frac{\partial \mathrm{u}}{\partial \mathrm{t}} \tag{1.8}$$

Definition of strain: $$\mathrm{S} = \frac{\partial \mathrm{u}}{\partial \mathrm{z}} \tag{1.9}$$

Hooke's law: $$\mathrm{T} = \mathrm{cS} \tag{1.10}$$

Working in one dimension for simplification purposes, we obtain a wave equation in a solid material:

$$\frac{1}{\rho}\frac{\partial^2 \mathrm{T}}{\partial \mathrm{z}^2} = \frac{1}{\mathrm{c}}\frac{\partial^2 \mathrm{T}}{\partial \mathrm{t}^2} \tag{1.11}$$

where ρ is the density of the material and z the direction of propagation. The solution of this equation is a wave with phase velocity [21]:

$$v_a = \sqrt{\frac{\mathrm{c}}{\rho}} \tag{1.12}$$

Another important magnitude of the medium in which the acoustic wave is propagating is the acoustic impedance, which is the relation between T and the particle velocity v [21]:

$$Z = -\frac{\mathrm{T}}{v} = \frac{jc\omega u}{v \cdot v_a} = \frac{cv}{v \cdot v_a} = \frac{c}{v_a} = \rho v_a \tag{1.13}$$

Acoustic impedance units are $\mathrm{kg/s \cdot m^2}$. Phase velocity and acoustic impedance are properties of the medium in which the acoustic wave is propagating, so they are very important when designing an EA device.

Quartz is the most studied piezoelectric material, and the core of the quartz crystal microbalance (QCM), which is the most typical example of an EA device. It consists of a piece of quartz, cut in a specific way, sandwiched between two metallic electrodes. These electrodes are used for applying the electric field that generates the acoustic waves within the piezoelectric material. The interfaces between quartz and electrodes make the waves suffer a reflection and therefore, interferences can happen. When a constructive interference takes place, a resonance arises. The frequency of this resonance follows this expression:

$$f_r = \frac{Nv}{2d} = \frac{v}{\lambda} \tag{1.14}$$

being

$$d = \frac{N\lambda}{2}; N = \{1, 3, 5, 7, \dots\} \tag{1.15}$$

the constructive interference condition. Here, v is the velocity of the acoustic wave, d is the thickness of the piezoelectric material and λ is the wavelength of the acoustic wave. $N = 1$ denotes the fundamental frequency of the resonant mode [23].

1.1.2. Types of piezoelectric resonators

Piezoelectric resonators have been widely studied since the 60s [24] and mainly used in telecommunication industry [25], [26]. As they provide sharp and tunable resonances they can be used as filters for radiofrequency (RF) communications, and they are an important component of this technology even in today's world, as some state-of-the-art studies demonstrate [27]. In parallel, their study and implementation as transducing mechanisms in sensor applications has been carried out [28], [29]. As said before, the most mature and developed technology within the piezoelectric resonators is the QCM, which has quartz as its main component and acting as piezoelectric material.

Piezoelectric materials are the key component of the EA devices we are going to study throughout this thesis. When a pair of electrodes are placed in contact with a piezoelectric material and used to generate an electric field, hence creating mechanical waves, it is called a piezoelectric resonator. Depending on its configuration and the type of wave they take advantage of, we can classify them into three main categories. Figure 1.1 shows these three main categories: (a) and (b) belong to the bulk acoustic wave (BAW) family, (c) belongs to the surface acoustic wave (SAW) family and (d) to the plate wave family.

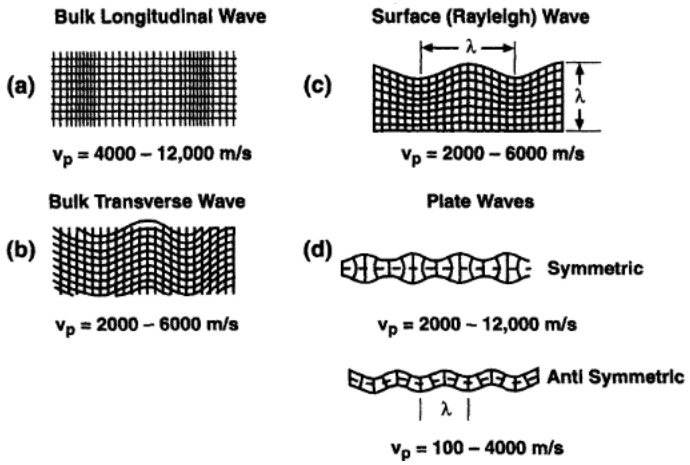

Figure 1.1. Graphical representation of different types of acoustic waves in solids: (a) Longitudinal and (b) Shear BAWs, (c) SAWs and (d) plate waves [23].

BAW devices are based on acoustic waves that can travel through the bulk of the piezoelectric material. These waves can be longitudinal (compressional) or shear (transverse) depending on how they propagate through the material,

generating different resonances with specific properties. Figure 1.2 shows the main difference between compressional and transverse acoustic waves, that is particle displacement. When particle displacement goes in the same direction as wave propagation, we call it a longitudinal BAW, whereas when particle displacement is orthogonal to wave propagation, we call it a shear BAW. In this case, we could have a horizontal shear wave or a vertical shear wave. If longitudinal and transverse waves propagate through a material at the same time, the composition of those waves would be called an elliptical wave [30]. In these devices, the resonant frequency is often determined by the thickness of the piezoelectric material, which is sandwiched between two metal electrodes that are used as the electrical excitation mechanism to produce the acoustic waves.

Figure 1.2. Diagrams showing the particle displacement (in small arrows) direction and the wave propagation direction (big arrows) for compressional and transverse acoustic waves.

As mentioned, QCMs are the most mature technology within the piezoelectric resonators, and they fall into the BAW device category. The acoustic wave generated in the material is a thickness shear mode (TSM) that travels from one electrode to the other. Figure 1.3 depicts a diagram of the side and top view of a QCM. Following equation 1.15, when $N = 1$ we have the fundamental resonant mode and, therefore, the thickness of the QCM plate should be equal to half a wavelength of the TSM. These devices were the first to be studied and successfully implemented in the telecommunications industry as RF filters [31], since their fundamental mode usually resonates in the few MHz range. They are also commonly used as thickness sensors in many microfabrication techniques, such as thermal evaporation [28], [32].

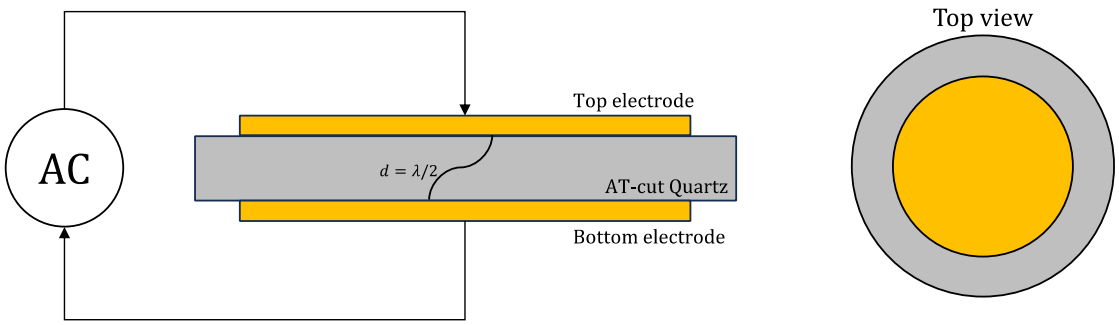

Figure 1.3. Diagram of the side and top view of a typical QCM.

Frequency-wise, QCMs present a major limitation, since the quartz plates cannot be thinned to reach higher frequency values. To overcome that, BAWs can be generated in thin films from other piezoelectric materials, such as AlN, $LiNbO_3$ or ZnO, among others [33]–[39]. With these materials, it is possible to obtain thinner films that allow us to have smaller devices working in higher frequency ranges. These devices are called film bulk acoustic resonators (FBAR), and they can be presented in different configurations. The resonator part is very similar to the QCM, although this time the piezoelectric material is presented in thin film form. To help confine the acoustic wave within the piezoelectric layer, the substrate on which the resonator was fabricated can be etched, leaving an air cavity that drastically improves the acoustic insulation of the system [40]. This configuration is usually called free standing FBAR. A representation of one is shown in Figure 1.4(a). Figure 1.4(b) shows the other main FBAR configuration called solidly mounted resonator (SMR). In short, the acoustic resonator is placed on top of alternate layers of high and low acoustic impedance [41]–[43], which serves a similar purpose as the air cavity in the free standing FBAR configuration. This design will be furthered explained. On the one hand, free standing FBARs usually provide great acoustic insulation, but, on the other hand, since SMRs are not suspended in air, they are less fragile and improves potential heat spreading issues while providing good acoustic insulation [26].

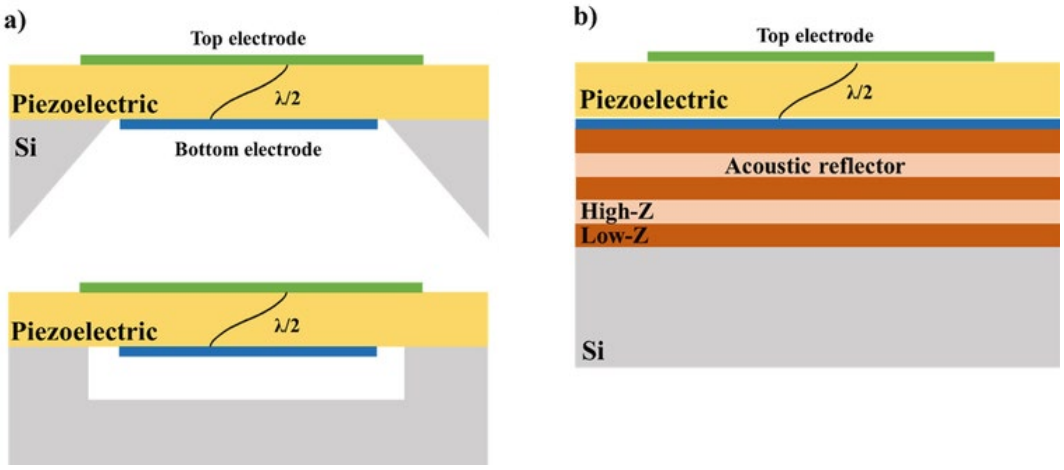

Figure 1.4. Representation of the cross-section of (a) free standing FBARs; and (b) an SMR [44], [45].

SAW devices work under the principle of acoustic waves with their energy being confined near the surface of the piezoelectric material. For this purpose, a large number of metallic comb-like electrodes are patterned on the surface of the material, and they are called interdigital transducers (IDTs). These electrodes are responsible for the excitation and detection of the SAWs. There are mainly two types of SAW devices: one-port and two-port resonators [46], [47], and two-port delay lines [48]. Figure 1.5(a) and Figure 1.5(b) show diagrams of these two configurations. As it can be seen the resonator configuration is also provided with two reflector gratings that confine the acoustic energy generated between the input and output IDTs. In the case of one-port resonators, the same IDT is used for excitation and read-out. The resonant frequency of these devices can be tuned by modifying the period of the IDTs and the reflectors, and the distance between them. It also depends strongly on the acoustic properties of the substrate [49]. The delay line configuration is similar, but it does not need the reflectors, because, in this case, the acoustic wave generated at the input IDT is collected at the output after travelling across the surface of the substrate. Thus, the point of this device is to characterize this wave after a finite delay in time.

SAW devices work in a broad range of frequencies, going from few MHz [48] to even GHz [46]. Owing to the advances reached in photolithography techniques, smaller separations can be achieved between the comb-like electrodes of the IDTs, thus resulting in the generation of acoustic waves with lower wavelengths. Single crystalline materials like quartz or $LiNbO_3$ [47], [50] are commonly used for manufacturing SAW devices, although thin films have been explored in recent years,

and materials like AlN or AlScN [46], [51] have gained the attention of researchers and industry as key components of this type of EA resonators.

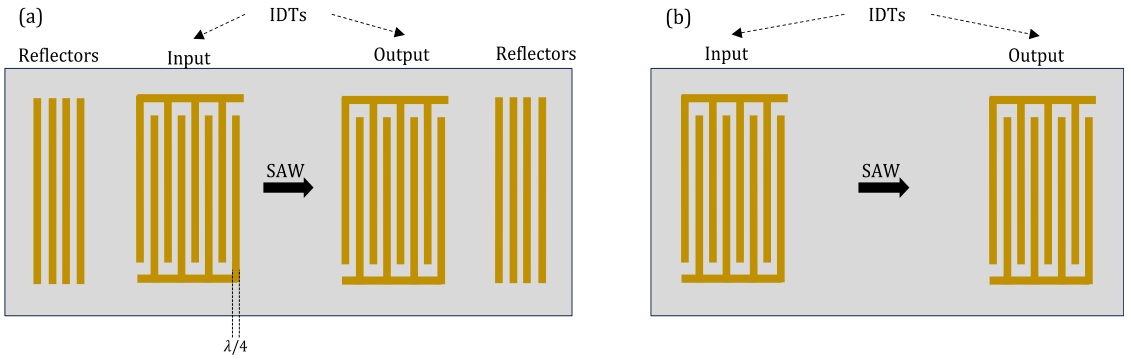

Figure 1.5. Representation of (a) a two-port SAW resonator and (b) a SAW delay line device.

Plate wave devices are mainly based on a composition of longitudinal and shear vertical waves, called Lamb waves, propagating across a very thin film, with thickness comparable to λ or even smaller. Their study and development began in the early 2000s [52], so they are a technology younger than BAW and SAW devices. These devices, also called Lamb wave resonators (LWR), use IDTs to produce the acoustic waves, in a similar way to SAW devices [53], [54]. They can be fabricated in two different topologies, depending on their acoustic isolation. Figure 1.6(a) shows a typical design of a LWR with reflector gratings, which would create a resonant cavity very similar to the ones present in SAW resonators. Figure 1.6(b) shows a resonator with edge reflection, also called contour mode resonators [55], [56]. These resonators usually work in the range of MHz, although in recent years, their operating frequency has been improved to the GHz range [53]. As can be seen from Figure 1.1(d), Lamb modes can be either symmetric or antisymmetric, denoted as S_n and A_n, respectively. The n subscript refers to the mode order, as these devices are often based on higher order modes, and not only the fundamental mode one [57]. When the resonator is based on A_n modes, they are usually called flexural plate wave resonators [58]. There are also plate wave devices based on shear horizontal SAWs (SH-SAW) [59], whose operation is based on the same layouts as SAWs and LWRs but taking advantage of different cuts of the piezoelectric layers, i.e., using piezoelectric thin films with different crystal orientations. The most common piezoelectric materials used for this family of devices are $LiTaO_3$ [53], [59] and $LiNbO_3$ [57], although other piezoelectric materials such as AlN [55] and AlScN [56] have been studied over the last years.

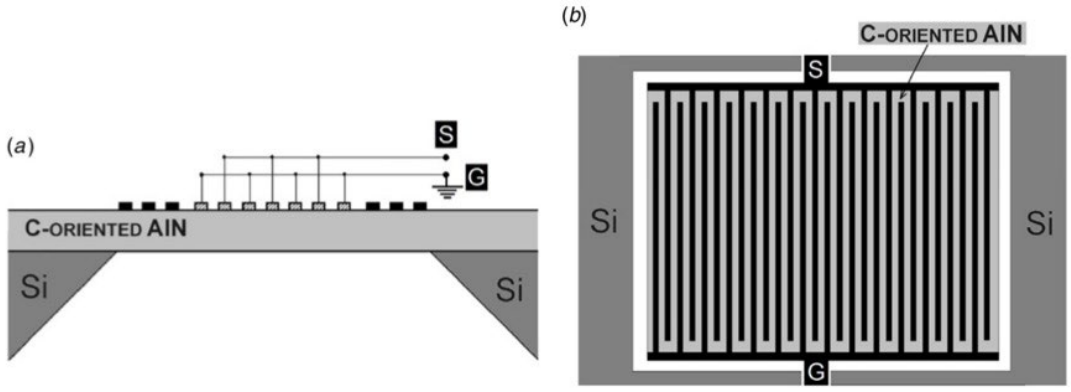

Figure 1.6. LWRs with (a) reflector gratings and (b) edge isolation [60].

In recent years, new types of resonators have come up as alternatives to the devices already mentioned. For instance, new types of LWRs, called laterally excited bulk acoustic resonators, have been developed using ZY cut $LiNbO_3$ very thin films and Al IDTs. In this case, electrical excitation produces shear vertical A_1 Lamb modes, operating at ~4.8 GHz and resulting in large electromechanical coupling factors [61]. Another example is the high overtone bulk acoustic resonator (HBAR), in which a thin piezoelectric film is placed on a low acoustic loss substrate to act as cavity to confine the acoustic waves while supporting the thin film. Figure 1.7 shows a diagram of a typical HBAR configuration. This coupled system induces a series of narrow resonances with modulated amplitudes [62]. Using these resonances, the operating frequencies of the HBARs are usually in the GHz range and with very low acoustic losses.

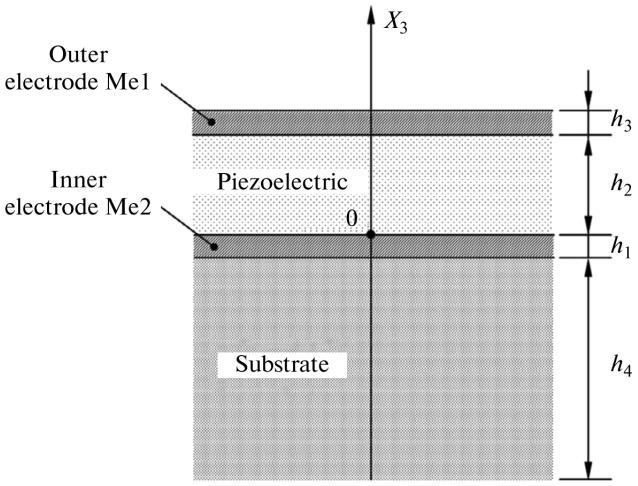

Figure 1.7. Representation of the cross section of an HBAR [63].

1.1.3. Solidly mounted resonators

Within FBAR devices, SMRs have caught the attention of many researchers in the last decades. The first approaches to this type of EA device came in the 60s [24]. As mentioned in previous section, SMRs consist of a piezoelectric thin film sandwiched between two electrodes and placed on a specific heterostructure, called acoustic reflector, consisting of alternating high and low acoustic impedance layers [42]. This structure must be specifically designed to provide optimum acoustic isolation to the resonances generated within the piezoelectric slab. For this purpose, the thickness of the layers must be set to $\lambda/4$ in each specific material. When the reflector meets this criterium, it is called a Bragg mirror, due to its similarities to the structures used in optics [64]. Figure 1.8(a) shows the diagram of a Bragg mirror design intended to form part of an AlN-based SMR operating at 3 GHz in longitudinal mode. Figure 1.8(b) shows its transmittance curve, revealing a minimum at the desired frequency. This means that the reflector has a reflectance maximum in that region, therefore acoustic energy generated at those frequencies is better confined inside the piezoelectric resonator. As it can be observed, the acoustic reflector shows a different transmittance minimum for shear modes, so it is necessary to have this in mind when designing devices intended to operate under this type of modes. A quite usual number of layers to make the reflector is five [37], although in this thesis almost all the designs will consist of seven layers for further isolation, starting and finishing with the low acoustic impedance material [65].

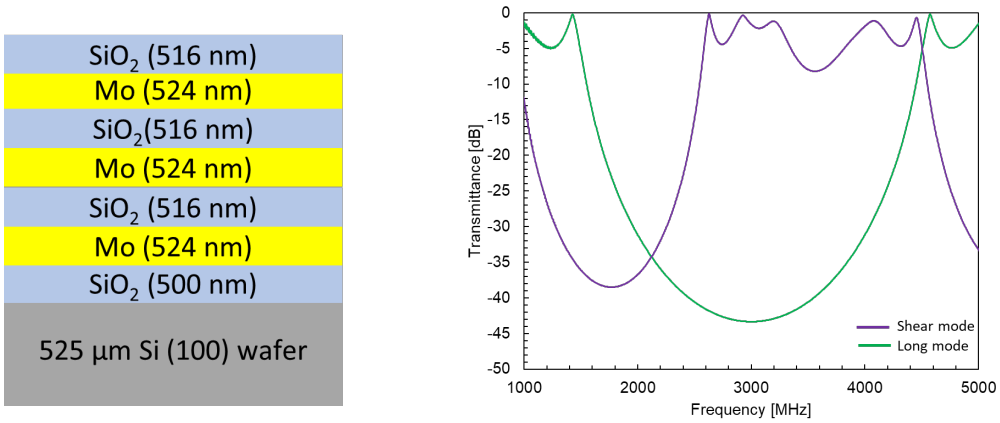

(a) (b)

Figure 1.8. (a) Representation of a Bragg mirror with $\lambda/4$ for each layer. (b) Simulated transmittance of a typical Bragg mirror used for the SMRs fabricated for this thesis.

One of the most important things to keep in mind when designing one is that there needs to be a great difference in acoustic impedance (eq. 1.13) between the two materials involved. For the low acoustic impedance layers, the most common material is SiO_2 due to its low density and acoustic velocity. Its deposition process through sputtering techniques is also well developed and very easy to control and monitor [66], resulting in a mature technology both for research and production purposes. There are some alternatives to SiO_2, such as silicon oxicarbide (SiOC) [67], or even some metallic materials like Ti [41]. Regarding the high acoustic impedance materials, Mo [35], W [68], [69] or even Al [70] are the most common choices. Other metals such as Pt [71] or Ir [72] have been explored, too. These materials are usually the most convenient high acoustic impedance layers due to both their high density and acoustic velocity. However, some applications require the acoustic reflector not to be conductive because undesired spurious modes can appear in the frequency response of the SMR. To avoid this, dielectric materials such as AlN [73] and Ta_2O_5 [74], [75] are employed as high acoustic impedance layers. Other insulators like HfN [76], HfO_2 [77] or SiN [67] have been studied, as well as ZnO [78]. A comparison between some of these materials will be presented in the forthcoming chapters of this thesis.

Typical frequency response of an AlN-based SMR is shown in Figure 1.9(a), with their resonant and anti-resonant frequencies indicated. In this case, the resonator follows a similar configuration to the one shown in Figure 1.8 (a) and the displayed mode is longitudinal. As seen in previous subsection, this means that wave propagation and particle displacement share the same direction. In terms of crystalline structure, this means that the c-axis of the AlN wurtzite structure is orthogonal to the bottom electrode surface. A SEM micrograph of this type of AlN film is shown in Figure 1.9(b), where the c-axis orientation can be observed [79].

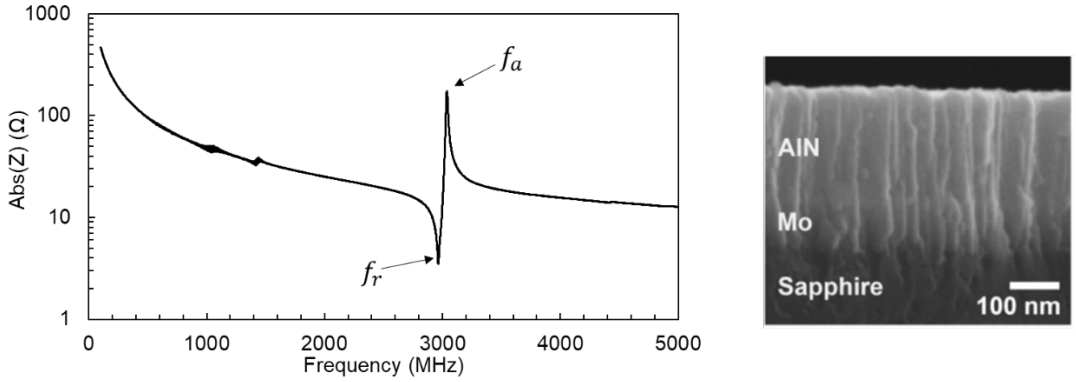

(a) (b)

Figure 1.9. (a) Frequency response of an AlN-based SMR. The resonant (f_r) and anti-resonant (f_a) frequencies are indicated on the plot. (b) SEM micrograph of a c-axis oriented AlN film [79].

SMRs can also display shear mode excitation. A typical frequency response measurement of a shear mode SMR is depicted in Figure 1.10(a). It can be noted that, in this case, both shear and longitudinal modes appear in the resonator response. This can be explained by the orientation of the AlN grains in the piezoelectric film, as it can be observed from Figure 1.10(b). In this case the c-axis of the wurtzite structure is not aligned with the vertical and this tilt is the responsible of the shear mode appearance. Also, this same reason, the generated longitudinal mode is attenuated compared to the one in Figure 1.9(a), where the vertical c-axis orientation is stronger, and no apparent tilt is observed.

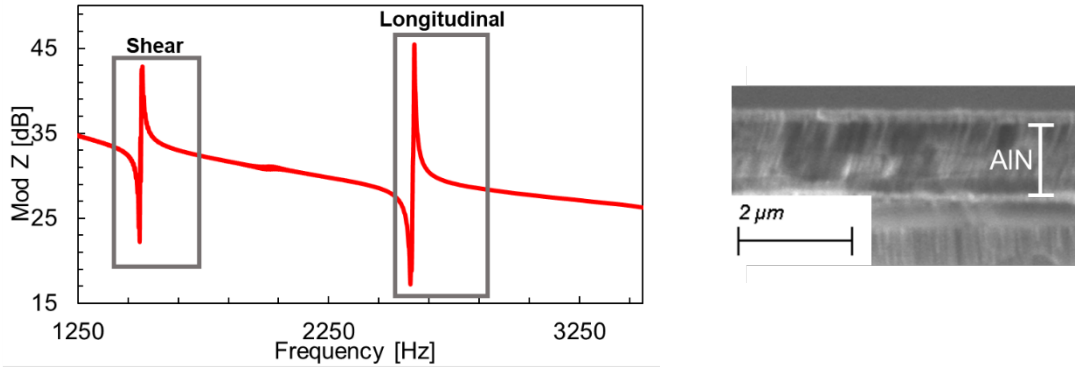

(a) (b)

Figure 1.10. (a) Frequency response of an AlN-based SMR displaying a shear mode. The two modes are indicated on the plot. (b) SEM micrograph of a tilted c-axis oriented AlN film.

As already mentioned, the ability of a piezoelectric material to transform electrical energy into mechanical energy, or vice versa, is expressed by the electromechanical coupling coefficient, k^2, defined in eq. 1.6. However, when the whole resonator is taken into consideration, this value is not completely precise. For this purpose, the effective electromechanical coupling coefficient, k_{eff}^2, is introduced. The most accepted definition for this coefficient is the one proposed by the IEEE Standard on piezoelectricity [80]:

$$k_{eff}^2 = \frac{\pi}{2}\frac{f_r}{f_a}\frac{1}{\tan\left(\frac{\pi}{2}\frac{f_r}{f_a}\right)} \tag{1.17}$$

expression that can be simplified to [81]:

$$k_{eff}^2 \approx \left(\frac{\pi}{2}\right)^2 \frac{f_r - f_a}{f_a} \tag{1.18}$$

This formulation demonstrates that k_{eff}^2 is proportional to the bandwidth of the mode, $f_r - f_a$. This quantity is key for RF applications in communications, as larger bandwidths are needed to meet the requirements of 5G standards in telecom industry [82]. For sensor applications, although being important, this remains on a secondary level. The other important quantity to be considered when measuring the performance of an SMR is its quality factor, or Q factor, which is a measure of the energy losses of the device. The most common approach to define it is using the ratio of the energy stored in the resonator to the dissipated energy per cycle [21]:

$$Q = 2\pi \frac{\text{Energy stored}}{\text{Energy dissipated}} \tag{1.19}$$

To express this ratio in terms of the characteristic properties of an SMR (and any piezoelectric resonator in general), two similar approaches are often used, being the first one the following:

$$Q_{r,a} = \frac{f_{r,a}}{(\Delta f)_{FWHM}} \tag{1.20}$$

where $(\Delta f)_{FWHM}$ is the full width at half maximum of the real part of the admittance (or impedance) curve at the position of resonance (or anti-resonance). The second approach can be expressed as

$$Q_{r,a} = \frac{f_{r,a}}{2}\left(\frac{\mathrm{d}\phi(Z)}{\mathrm{d}f}\right)_{f_{r,a}} \tag{1.21}$$

where $\phi(Z)$ is the phase of the impedance. Therefore, Q factor is proportional to the steepness of the phase of the impedance at resonant (or anti-resonant) frequency. Figure 1.11 shows a comparison between resonators displaying higher (Resonance 1) and lower (Resonance 2) Q factors together with their phase curves. It can be noted how the phase shift for the resonant frequency is better defined in the resonator with higher Q factor, and the same happens for the anti-resonant frequency. Using eq. 1.21, the calculated Q factors are $Q_r = 659.6$ and $Q_a = 645.9$ for Resonance 1 and $Q_r = 286.4$ and $Q_a = 280.4$ for Resonance 2. For sensing applications, this magnitude is key because higher values mean sharper resonances, which are easier to track and display lower noise, resulting in sensors with better properties, such as lower limits of detection [83].

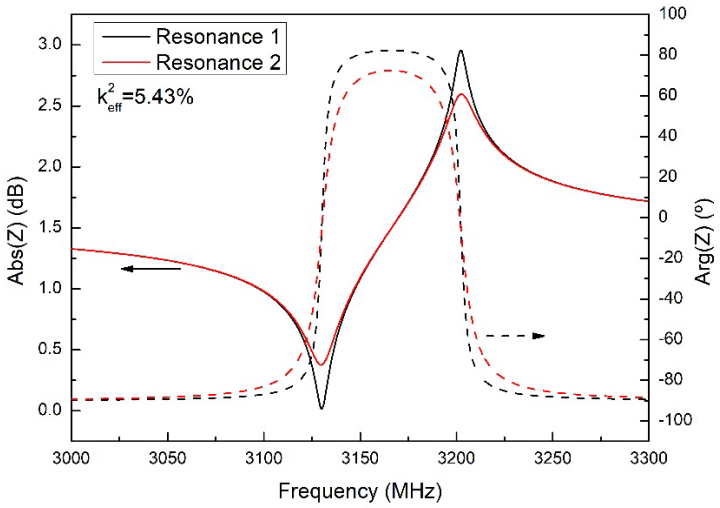

Figure 1.11. Comparison between high Q factor and low Q factor resonances.

1.2. ELECTROACOUSTIC SENSORS

EA resonators offer a set of properties that can make them good candidates to work as transducers for sensor applications. A small change in their electrical or elastic properties can have a significant influence on their response, so by identifying the cause of this change we can detect and quantify the involved magnitudes. If the sensing target is a specific species, such as gas or biomolecules, the functionalization of the resonator surface is required to act as a sensing layer that, after interaction with the desired species, influences the response of the resonator. The magnitudes that give sense of the performance of a resonator, already mentioned, are their operating frequencies f_r and f_a, their effective coupling factor k_{eff}^2, and their Q

factor values, Q_r and Q_a. However, for sensing applications, the performance of the device will be also determined by the following magnitudes:

- Sensitivity (S): the relationship between of the sensor's change in response and the change in the target magnitude. For an EA sensor, this would be translated to the measured shift in frequency divided by the change in the magnitude we aim to detect. For instance, if the target is a specific gas species, S would be expressed as:

$$S = \frac{f - f_0}{[\text{target gas}]} \tag{1.22}$$

  where f_0 is the original resonant frequency, before exposing the target species to the sensor, and [target gas] is the concentration of the analyte exposed to the sensor. S can also be expressed as a percentage:

$$S\ (\%) = \frac{1}{f_0}\frac{f - f_0}{[\text{target gas}]} \times 100 \tag{1.23}$$

- Limit of detection (LOD): the smallest change in the target magnitude that the sensor is capable to detect. It can be calculated as three times the standard deviation of the background noise divided by the sensitivity [84]:

$$\text{LOD} = \frac{3\sigma}{S} \tag{1.24}$$

- Resolution (R): smallest change in the target magnitude that can be recognized in the output signal. The most usual way of reading the output signal is using a readout circuit based on an oscillating loop with the resonator in the feedback branch. Therefore, the potential signal noise added by the circuit is of key importance to acknowledge this property. A good approximation is the resolution factor (R_F):

$$R_F = \frac{3 \times 10^{-7}}{Q \times S} \tag{1.25}$$

  - where Q is the quality factor of the resonator and 10^{-7} is a constant extracted from the IEEE standard 1139-1988 for frequency stability measurement described in terms of the Allan deviation [85]. Thus, to

obtain a low resolution factor, the product $Q \times S$ must be as high as possible.

- Response and recovery times (t_{resp} and t_{rec}): The response time is that required to reach 90% of the steady-state value after exposition to the target magnitude. The recovery time is defined as the time required to reach 90% of the baseline value once the sensor gets to the initial state [86].
- Selectivity: the ability of the sensor to only detect the target magnitude or analyte concentration and not provide false positives [87].
- Stability over time: the ability of the sensor to provide the same response after a determined number of uses or after being used well after being tested for the first time [88].

1.2.1. Principle of work

EA-based sensors do not have a unique way of operation. Although their most common mode of operation is as a gravimetric sensor, this type of device offers more alternatives that makes it highly adaptable to work in a multitude of environments, and to detect a great range of species and/or changes in different magnitudes, depending on their functionalization.

Gravimetric sensing takes place when the target analyte is adsorbed onto the surface of the sensor. This process increases the mass being supported by the resonator and, therefore, the resonance suffers a shift in frequency. It can also be seen as a variation of the acoustic energy distribution due to changes on the device surface. This mechanism can be described by Sauerbrey's equation [89]:

$$\Delta f_r = -\frac{2f_0^2}{A\sqrt{\mu\rho}}M \tag{1.26}$$

where A is the area of the sensing layer, μ is the shear modulus and ρ the density of the piezoelectric material, and M is the mass of the target analyte. The minus sign means that the greater the mass adsorbed by the sensor, the lower the final frequency value will be. This is the most common approach for EA resonators in sensor applications, and it is also the first one reported [90].

Other properties of the resonators can be exploited to quantify certain magnitudes with great precision. For instance, an EA resonator can be designed

having in consideration the thermal expansion coefficients of the involved materials to fabricate a temperature sensor with high temperature coefficient of frequency (TCF), which can be defined as [58]

$$\mathrm{TCF}_{r,a} = \frac{\Delta f_{r,a}}{\Delta \mathrm{T}} \tag{1.27}$$

To detect changes in other environmental conditions, such as relative humidity, the changes in Young's modulus of the sensing layer can provoke a shift in the frequency response of the resonator [84], so a similar quantity to the TCF can be defined as

$$\mathrm{HCF}_{r,a} = \frac{\Delta f_{r,a}}{\Delta(\%\mathrm{RH})} \tag{1.28}$$

where HCF in this case stands for humidity coefficient of frequency.

The response generated by the sensing layer-resonator structure can be altered by changes in viscoelastic properties. When the resonators are functionalized with either polymers or biochemical layers, changes in viscosity can derive in a positive shift in frequency, which can be useful for biosensing applications [91].

Adsorbing certain gas species can induce changes in the electrical properties of the sensing layer. Therefore, measuring the changes in resistance at resonance it is possible to detect this adsorption process and quantify the concentration of the target [19]. This change in resistance can also induce a change in the elastic properties of the sensing layer and thus of the entire device [92]. This behavior also causes a shift in frequency that can be used to quantify the concentration of the target gas [93]. This last mechanism is also dependent on the thickness of the sensing layer and will be further discussed in Chapter 4.

1.2.2. State of the art

EA resonators, and QCMs in particular, were proposed as good candidates for sensor applications for the first time in the 1960s [90]. However, it was not until a few decades ago that they started to gain recognition in the research community and to be deeply studied for this purpose [91], [94], [95]. As already mentioned, this type of devices stands out especially for its versatility and low fabrication cost. QCMs are the standard when measuring thicknesses and deposition rates for thin film

technology fabrication techniques, such as thermal evaporation [96]. Many researchers have also explored the possibility of functionalizing QCMs to act as high-resolution humidity sensors. For instance, Wang et al. [97] developed a PAA/PVA functionalized QCM sensor at room temperature with good sensitivity in the 5-95% RH range. More recently, Li et al. [88] used an Sb-doped WO_3 nanostructure to act as humidity sensing layer on QCMs with fast recovery and response times for operation up to 85% in RH with a measured sensitivity of 36.5 Hz/%RH. For temperature measurement, Tsuchiya et al. [17] reported a specific designed QCM to work on a wide range of temperatures, from −190 to 125 °C, with good resolution and stability. Gas sensing and biosensing applications have also been studied in the last years for QCMs. Gomes et al [98] studied QCMs for detection of several gases, including CO_2 and NH_3, whereas Chen et al. [20] reported a graphene oxide/cuprous oxide nanocomposite functionalized QCM for trimethylamine detection in more recent years. In the biosensing field, many useful approaches have been explored for operation in air and in liquid media [99].

SAW devices have also been studied as candidates for sensing applications over the last years [100]. Temperature and humidity sensors with high sensitivity have been reported [101], [102], as well as pressure sensors [103], biosensors [104] and gas sensors based on this technology. For instance, Wang et al. [105] reported a SAW device functionalized with (Cu^{2+})PANI/WO_3 films for nitric oxide detection with great LOD, reaching values in the low ppb range.

FBAR technology, specifically focused on the SMR configuration, will be central to the developed work in this thesis. Several studies have affirmed the diverse range of environments and applications in which these devices can exhibit exceptional performance. Moreover, the higher operating frequencies they can achieve lead to higher sensitivities than QCM and SAW based sensors. In 2007, Chiu et al. [94] reported and AlN-based FBAR capable of working as pressure and temperature sensors, which then was developed into simultaneous detection taking advantage of a dual mode configuration by He et al. [106]. More recently, FBAR-based temperature sensors have been reported with highly improve sensitivity, reaching values up to 546 kHz/°C [107], [108]. In 2020, Liu et al. developed a PI-FBAR sensor for relative humidity quantification with a reported sensitivity of 67.3 kHz/%RH [16].

For gas and biosensing applications, FBARs are also a promising technology. Guo et al. proved the ability to detect epithelial tumor markers using AlN-based

SMRs with biotin-avidin functionalization [18]. Furthermore, as SMRs can work in shear mode configuration, this enables the possibility of operation in liquid [74]. For example, Liu et al. reported in 2020 a ZnO-based SMR capable of detecting cardiac biomarkers in biological fluids, such as serum [109]. Using a split mode configuration, Wajs et al. studied ZnO-based SMRs for detection of PSA in blood samples [110]. Regarding the gas sensing field, there are also many studies involving FBAR devices [111]. Song et al. reported AlN-based FBARs functionalized with CNT/polyethyleneimine for formaldehyde detection [112]. Chen et al. developed AlN-based SMRs with Pd functionalization for H_2 detection [113]. Hoffmann et al. also fabricated ZnO-based SMRs functionalized with polyamino-siloxane with high sensitivity towards CO_2 detection [93]. Another interesting approach is the one took by Gao et al., who took advantage of the shift in frequency and in resistance to propose a dual transduction method for a single FBAR device [19]. All these studies show the versatility of FBARs as they can be used to detect many different species and magnitudes as they are also compatible with typical functionalization techniques, such as dropcasting [19], spincoating [93], [114], evaporation [95], and sputtering [113], [115]. However, almost all the found literature stablish similar operation conditions for the sensors.

1.2.2.1. High temperature applications

The need for monitorization of gas species also extends to high temperature environments. Economy driver industries, such as the automotive sector, demand sensors capable of detecting different chemical species in this type of environments. For instance, the monitorization of exhaust contaminating gases in vehicles is crucial to keep optimal air quality levels, and to reach compliance with environmental policies and regulations. This would not be the only sector to benefit from pushing research on this topic, as industries like agriculture, energy and defense also share similar necessities [116].

SAW devices are the most studied for these applications, as they have been demonstrated to survive operation under harsh environments [117]. In 2006, Thiele et al. [118] reported a langasite SAW sensor able to detect C_2H_4 and H_2 in the 250 to 450°C range using WO_3/Pt electrodes as functionalization layer. A similar structure but using sputtered ZnO as sensing layer was studied by Zheng et al. [119], detecting different O_2 concentrations in the 500 to 700°C range. More recently, Ghosh et al.

[120] developed a Ca doped ZnO thin film used to functionalize a langasite SAW resonator to fabricate a CO_2 sensor for operation at temperatures up to 400°C.

There are few reported cases in where the operation temperature moves away from room temperature conditions for BAW device sensors. Seh et al. studied the potential of QCM resonators functionalized with $BaCO_3$ for NO_2 detection, reaching optimal operation for temperatures above 300°C [121]. In 2019, Zeng et al. reported an AlN-based SMR able to work under near 100°C operation temperatures to detect and discriminate between different VOCs [122]. However, BAW devices, and SMRs in particular, offer some design advantages compared to SAW devices for high temperature operation. Despite both being robust, SAW electrodes can suffer from destructive agglomeration, i.e., high frequency operation requires the IDTs to be extremely close and high temperatures might cause diffusion and short circuits. SAW devices are also harder to integrate due to the fact that they are based in bulk materials. In addition, design in SMRs tend to be more flexible, as the same frequencies can be reached with different electrode and piezoelectric layer thicknesses. This allows the electrodes to be thicker at higher temperatures if necessary, reducing thus the electrical resistance and allowing more power to be applied. Furthermore, viable operation for SMRs under high temperature conditions has already been studied in our group [123], [124], so the next logical step would be to develop SMR sensors intended to work at high temperatures.

1.3. OBJECTIVES OF THE THESIS

The scope of this thesis is to expand the knowledge in the field of **FBAR sensors** by designing, fabricating, and testing SMR-based sensors capable of **operating in harsh environments**, such as high (200-400 °C) and low (-20 °C) temperature conditions. For this purpose, three main objectives need to be accomplished:

- *Study of the properties and behavior of the materials involved in the fabrication process*. Starting from the acoustic reflector, a study between different configurations including materials like AlN, HfN, ZnO and Ta_2O_5 to form fully dielectric reflectors is proposed, and a comparative study from performance point of view with Mo/SiO_2 configurations. These configurations should provide the resonators with different characteristics, especially in terms of acoustic isolation and noise in their frequency response. A study of $Al_{1-x}Sc_xN$ as an alternative piezoelectric

material to AlN is also proposed, taking special consideration in its thermal stability. Finally, concerning the resonator, the choice of electrodes is also of utmost importance as they contribute to the quality of the provided response, and in the top electrode case, is the one that provides the interface with the environment and with the functionalization layer, which is key specially under harsh conditions. *The last step for this objective is to study the potential functionalization layers and their integration in order to obtain already operating devices with good response for sensing applications.*

- *Design, development and testing of a sensor characterization setup.* This setup needs to be prepared to provide the necessary characterization tools for operation at high and low temperatures. Furthermore, gas injection and exhaust systems are needed to expose the fabricated sensors to the target gases and a humidity generation system to set relative humidity conditions. The setup also must allow the devices to be probed to gather all the data from characterization measurements.
- *Fabrication and characterization of SMR-based sensors for gas detection under harsh conditions*. For this thesis, the gas of choice is nitric oxide (NO), as it of big relevance for high temperature applications, for instance in the combustion process of fossil fuels.

The contents of this thesis are organized in six chapters that will cover the work carried out during my predoctoral experience to meet the stated objectives.

Current chapter, labeled as Chapter 1, has introduced EA resonators and their fundamentals, with emphasis on SMR devices. The principle of work and state of the art of the sensor applications based on these devices has also been covered.

Chapter 2 describes the fabrication techniques used for the devices reported in this thesis. The characterization techniques used for assessing material properties and resonator performance are also discussed. Finally, a description of the design and manufacturing of the gas sensing setup is included.

Chapter 3 covers the fabrication of the SMR-based sensors. From the study of the materials involved in the acoustic reflectors, electrodes and piezoelectric layers to the fabrication route of the SMRs and their functionalization process.

Chapter 4 discusses the obtained results for the different sensors fabricated throughout the course of the thesis. It is divided into three sections depending on the temperature of operation. For low temperature conditions, a study of the

variations of relative humidity concentration and its influence on the response of the sensors is discussed, together with a proposal for discriminating them using dual mode configuration. For room temperature and high temperature conditions, the detection of NO is explored using two different functionalization methods: thermal evaporation of pentacene thin films and sputtering deposition of WO_3 films.

Chapter 5 gathers all the conclusions extracted from this thesis and Chapter 6 suggests some future lines of work that come up from the obtained results.

References

[1] W. E. Knowles Middleton, *A History of the Thermometer and Its Use in Meteorology*. Baltimore, Maryland, USA: The Johns Hopkins Press, 1966.

[2] S. R. A. Ruth, V. R. Feig, H. Tran, and Z. Bao, "Microengineering Pressure Sensor Active Layers for Improved Performance," *Adv. Functional Mater.*, vol. 30, no. 39. Wiley-VCH Verlag, Sep. 01, 2020. doi: 10.1002/adfm.202003491.

[3] V. K. Rai, "Temperature sensors and optical sensors," *Appl. Phys. B*, vol. 88, no. 2, pp. 297–303, Jul. 2007, doi: 10.1007/S00340-007-2717-4/METRICS.

[4] Z. Chen and C. Lu, "Humidity sensors: A review of materials and mechanisms," *Sensor Lett.*, vol. 3, no. 4. pp. 274–295, Dec. 2005. doi: 10.1166/sl.2005.045.

[5] H. Yousefi, H. M. Su, S. M. Imani, K. Alkhaldi, C. D. Filipe, and T. F. Didar, "Intelligent Food Packaging: A Review of Smart Sensing Technologies for Monitoring Food Quality," *ACS Sensors*, vol. 4, no. 4, pp. 808–821, Apr. 26, 2019. doi: 10.1021/acssensors.9b00440.

[6] F. Folianto, Y. S. Low, and W. L. Yeow, "Smartbin: Smart waste management system," *2015 IEEE 10th Intern. Conf. on Intell. Sensors, Sensor Netw. and Information Processing, ISSNIP 2015*, Singapore, May 2015, doi: 10.1109/ISSNIP.2015.7106974.

[7] R. Hopper, D. Popa, F. Udrea, S. Z. Ali, and P. Stanley-Marbell, "Miniaturized thermal acoustic gas sensor based on a CMOS microhotplate and MEMS microphone," *Sci. Rep.*, vol. 12, no. 1, pp. 1–6, Feb. 2022, doi: 10.1038/s41598-022-05613-0.

[8] J. Kim, A. S. Campbell, B. E. F. de Ávila, and J. Wang, "Wearable biosensors for healthcare monitoring," *Nature Biotech.*, vol. 37, no. 4, pp. 389–406, Apr. 01, 2019. doi: 10.1038/s41587-019-0045-y.

[9] J. Qin et al., "Flexible and Stretchable Capacitive Sensors with Different Microstructures," *Adv. Mater.*, vol. 33, no. 34, 2008267, Aug. 2021, doi: 10.1002/ADMA.202008267.

[10] N. Ahmed, A. Radchenko, D. Pommerenke, and Y. R. Zheng, "Design and Evaluation of Low-Cost and Energy-Efficient Magneto-Inductive Sensor Nodes for Wireless Sensor Networks," *IEEE Syst. J.*, vol. 13, no. 2, pp. 1135–1144, Jun. 2019, doi: 10.1109/JSYST.2018.2841872.

[11] M. D. Brown and M. H. Schoenfisch, “Electrochemical Nitric Oxide Sensors: Principles of Design and Characterization,” *Chemical Reviews*, vol. 119, no. 22, pp. 11551–11575, Nov. 27, 2019. doi: 10.1021/acs.chemrev.8b00797.

[12] R. J. Rath, S. Farajikhah, F. Oveissi, F. Dehghani, and S. Naficy, “Chemiresistive Sensor Arrays for Gas/Volatile Organic Compounds Monitoring: A Review,” *Adv. Eng. Mater.*, vol. 25, no. 3, 2200830, Feb. 2023, doi: 10.1002/ADEM.202200830.

[13] M. I. Zibaii, A. Kazemi, H. Latifi, M. K. Azar, S. M. Hosseini, and M. H. Ghezelaiagh, “Measuring bacterial growth by refractive index tapered fiber optic biosensor,” *J. Photochem. Photobiol. B*, vol. 101, no. 3, pp. 313–320, Dec. 2010, doi: 10.1016/J.JPHOTOBIOL.2010.07.017.

[14] Y. Kim et al., “2D Transition Metal Dichalcogenide Heterostructures for p- and n-Type Photovoltaic Self-Powered Gas Sensor,” *Adv. Funct. Mater.*, vol. 30, no. 43, 2003360, Oct. 2020, doi: 10.1002/ADFM.202003360.

[15] A. J. Gimenez, J. M. Yáñez-Limón, and J. M. Seminario, “ZnO-paper based photoconductive UV sensor,” *J. of Phys. Chem. C*, vol. 115, no. 1, pp. 282–287, Jan. 2011, doi: 10.1021/jp107812w.

[16] J. Liu, Z. Zhao, Z. Fang, Z. Liu, Y. Zhu, and L. Du, “High-performance FBAR humidity sensor based on the PI film as the multifunctional layer,” *Sens. Actuators B Chem.*, vol. 308, 127694, Apr. 2020, doi: 10.1016/j.snb.2020.127694.

[17] Y. Tsuchiya, H. Kukita, T. Shiobara, K. Yukumatsu, and E. Miyazaki, “Temperature Controllable QCM Sensor with Accurate Temperature Measurement for Outgas and Contamination Assessment,” *Proc. of IEEE Sensors*, vol. 2019-October, Oct. 2019, doi: 10.1109/SENSORS43011.2019.8956952.

[18] P. Guo et al., “A biosensor based on a film bulk acoustic resonator and biotin–avidin system for the detection of the epithelial tumor marker mucin 1,” *RSC Adv.*, vol. 5, no. 81, pp. 66355–66359, Jul. 2015, doi: 10.1039/C5RA06016H.

[19] F. Gao, W. Xuan, A. Bermak, F. Boussaid, C. Y. Tsui, and J. Luo, “Dual transduction on a single sensor for gas identification,” *Sens. Actuators B Chem.*, vol. 278, pp. 21–27, Jan. 2019, doi: 10.1016/J.SNB.2018.09.029.

[20] W. Chen, F. Deng, M. Xu, J. Wang, Z. Wei, and Y. Wang, “GO/Cu_2O nanocomposite based QCM gas sensor for trimethylamine detection under

low concentrations," *Sens. Actuators B Chem.*, vol. 273, pp. 498–504, Nov. 2018, doi: 10.1016/J.SNB.2018.06.062.

[21] J. Rosenbaum, *Bulk Acoustic Wave Theory and Devices*. Artech House, 1988.

[22] K. Uchino and J.-Claude. Debus, *Advanced Piezoelectric Materials*, Second. Woodhead Publishing Ltd, 2013.

[23] D. Ballantine Jr. ;Robert White; S. Martin; Antonio Ricco; E. Zellers; G. Frye; H. Wohltjen, *Acoustic Wave Sensors*. Academic Press Inc., 1996.

[24] W. E. Newell, "Face-Mounted Piezoelectric Resonators," *Proceedings of the IEEE*, 1965.

[25] G. Pillai and S. S. Li, "Piezoelectric MEMS Resonators: A Review*," IEEE Sensors J.*, vol. 21, no. 11, pp. 12589–12605, Jun. 01, 2021. doi: 10.1109/JSEN.2020.3039052.

[26] R. Aigner, "SAW and BAW technologies for rf filter applications: a review ofthe relative strengths and weaknesses," *Proc. IEEE Ultrason. Symp.*, pp. 582–589, 2008, doi: 10.1109/ULTSYM.2008.0140.

[27] K. Yang et al., "Advanced RF filters for wireless communications," *Chip*, 100058, Jul. 2023, doi: 10.1016/J.CHIP.2023.100058.

[28] S. J. Martin, V. E. Granstaff, G. C. Frye, and A. J. Ricco, "Using quartz crystal microbalances to simultaneously sense mass accumulation and solution properties," in *Transducers '91*, Publ by IEEE, 1991, pp. 785–788. doi: 10.1109/sensor.1991.149000.

[29] R. Lucklum, B. Henning, P. Hauptmann, K. D. Schierbaum, S. Vaihinger, and W. Göpel, "Quartz microbalance sensors for gas detection," *Sens. Actuators A Phys.*, vol. 27, no. 1–3, pp. 705–710, 1991, doi: 10.1016/0924-4247(91)87074-D.

[30] J. W. Grate and G. C. Frye, "Acoustic Wave Sensors," *Sensors Update*, vol. 2, 37–83, 1996, doi: https://doi.org/10.1002/1616-8984(199610)2:1%3C37::AID-SEUP37%3E3.0.CO;2-F.

[31] F. L. Walls and A. E. Wainwright, "Measurement of the Short-Term Stability of Quartz Crystal Resonators and the Implications for Crystal Oscillator Design and Applications," *IEEE Transactions on Instr. and Meas.*, 24(1), 15–20. https://doi.org/10.1109/TIM.1975.4314362.

[32] K. Bodenho, A. Hierlemann, G. Noetzel, U. Weimar, and W. Go, "Performances of Mass-Sensitive Devices for Gas Sensing: Thickness Shear Mode and Surface Acoustic Wave Transducers," *Analytical Chem.*, vol. 68, no. 13, pp. 2210-2218, Jul. 1996, doi: 10.1021/ac9600215.

[33] M.-A. Dubois, P. Muralt, H. Matsumoto, and V. Plessky, "Solidly mounted resonator based on aluminum nitride thin film," *Proc. of the IEEE Ultrason. Symp.*, 1, 909–912, 1998. https://doi.org/10.1109/ultsym.1998.762291

[34] E. Iborra, M. Clement, J. Capilla, J. Olivares, and V. Felmetsger, "Low-thickness high-quality aluminum nitride films for super high frequency solidly mounted resonators," *Thin Solid Films*, vol. 520, no. 7, pp. 3060–3063, Jan. 2012, doi: 10.1016/j.tsf.2011.11.007.

[35] S. Huang et al., "A Solidly Mounted Resonator Fabricated by $LiNbO_3$ Single-Crystalline Film on Flexible Polyimide Substrate," *IEEE Trans. Ultrason. Ferroelectr. Freq. Control*, vol. 68, no. 7, pp. 2585–2589, Jul. 2021, doi: 10.1109/TUFFC.2021.3066589.

[36] T. H. Hsu, K. J. Tseng, and M. H. Li, "Large Coupling Acoustic Wave Resonators Based on LiNbO/SiO/Si Functional Substrate," *IEEE Electron Dev. Lett.*, vol. 41, no. 12, pp. 1825–1828, Dec. 2020, doi: 10.1109/LED.2020.3030797.

[37] G. Rughoobur et al., "Room temperature sputtering of inclined c-axis ZnO for shear mode solidly mounted resonators," *Appl. Phys. Lett.*, vol. 108, no. 3, Jan. 2016, doi: 10.1063/1.4940683.

[38] X. Zhang, W. Xu, and J. Chae, "Temperature effects on a high Q FBAR in liquid," *Sens. Actuators A Phys.*, vol. 166, no. 2, pp. 264–268, 2011, doi: 10.1016/j.sna.2009.10.003.

[39] S. L. Pinkett, W. D. Hunt, B. P. Barber, and P. L. Gammel, "Determination of ZnO temperature coefficients using thin film bulk acoustic wave resonators," *IEEE Trans. Ultrason. Ferroelectr. Freq. Control,* vol. 49, no. 11, pp. 1491–1496, Nov. 2002, doi: 10.1109/TUFFC.2002.1049730.

[40] J. Wang, M. Park, S. Mertin, T. Pensala, F. Ayazi, and A. Ansari, "A Film Bulk Acoustic Resonator Based on Ferroelectric Aluminum Scandium Nitride Films," *J. of Microelectromech. Systems*, vol. 29, no. 5, pp. 741–747, Oct. 2020, doi: 10.1109/JMEMS.2020.3014584.

[41] C. J. Chung, Y. C. Chen, C. C. Cheng, C. L. Wei, and K. S. Kao, "Influence of surface roughness of Bragg reflectors on resonance characteristics of solidly-

mounted resonators," *IEEE Trans. Ultrason. Ferroelectr. Freq. Control*, vol. 54, no. 4, pp. 802–808, 2007, doi: 10.1109/TUFFC.2007.313.

[42] K. M. Lakin, K. T. Mccarron, and R. E. Rose, "SOLIDLY MOUNTED RESONATORS AND FILTERS," in *1995 IEEE Ultrason. Symp.*, 1995, pp. 905–908.

[43] D. Chen, Y. Xu, J. Wang, L. Zhang, X. Wang, and M. Liang, "The AlN based solidly mounted resonators consisted of the all-metal conductive acoustic Bragg reflectors," *Vacuum*, vol. 85, no. 2, pp. 302–306, Aug. 2010, doi: 10.1016/j.vacuum.2010.07.001.

[44] M. Li et al., "Ultralow-phase-noise oscillators based on BAW resonators," *IEEE Trans. Ultrason. Ferroelectr. Freq. Control*, vol. 61, no. 6, pp. 903–912, 2014, doi: 10.1109/TUFFC.2014.2986.

[45] T. Mirea, "FBAR Devices: Fundamentals, Fabrication and Applications," *in Springer Series on Chemical Sensors and Biosensors*, Berlin, Heidelberg: Springer, 2023. doi: 10.1007/5346_2023_27.

[46] J. G. Rodríguez-Madrid, G. F. Iriarte, O. A. Williams, and F. Calle, "High precision pressure sensors based on SAW devices in the GHz range," *Sens. Actuators A Phys.*, vol. 189, pp. 364–369, Jan. 2013, doi: 10.1016/J.SNA.2012.09.012.

[47] M. Penza, F. Antolini, and M. Antisari Vittori, "Carbon nanotubes as SAW chemical sensors materials," *Sens. Actuators B Chem.*, vol. 100, no. 1–2, pp. 47–59, Jun. 2004, doi: 10.1016/j.snb.2003.12.019.

[48] N. M. Tashtoush, J. D. N. Cheeke, and N. Eddy, "Surface acoustic wave humidity sensor based on a thin PolyXIO film," *Sens. Actuators B Chem.*, vol. 49, no. 3, pp. 218–225, Jul. 1998, doi: 10.1016/S0925-4005(98)00131-2.

[49] C. Campbell, *Surface Acoustic Wave Devices and their Signal Processing Applications*. Academic Press Inc., 1989. doi: 10.1016/b978-0-12-157345-4.x5001-2.

[50] A. Holm, Q. Stürzer, Y. Xu, and R. Weigel, "Investigation of surface acoustic waves on $LiNbO_3$, quartz, and $LiTaO_3$ by laser probing," *Microelectron. Eng.*, vol. 31, no. 1–4, pp. 123–127, Feb. 1996, doi: 10.1016/0167-9317(95)00334-7.

[51] N. Kurz et al., "Experimental determination of the electro-acoustic properties of thin film AlScN using surface acoustic wave resonators," *J. Appl. Phys.*, vol. 126, no. 7, p. 75106, Aug. 2019, doi: 10.1063/1.5094611.

[52] J. Bjurström, I. Katardjiev, and V. Yantchev, "Lateral-field-excited thin-film Lamb wave resonator," *Appl. Phys. Lett.*, vol. 86, no. 15, pp. 1–3, 2005, doi: 10.1063/1.1900312.

[53] N. Assila, M. Kadota, and S. Tanaka, "High-Frequency Resonator Using A1 Lamb Wave Mode in $LiTaO_3$ Plate," *IEEE Trans. Ultrason. Ferroelectr. Freq. Control*, vol. 66, no. 9, pp. 1529–1535, Sep. 2019, doi: 10.1109/TUFFC.2019.2923579.

[54] T. T. Yen et al., "Characterization of aluminum nitride lamb wave resonators operating at 600°C for harsh environment RF applications," *Proc. of the IEEE Intern. Conf. on Micro Electro Mechanical Systems (MEMS)*, pp. 731–734, 2010, doi: 10.1109/MEMSYS.2010.5442304.

[55] G. Piazza, P. J. Stephanou, and A. P. Pisano, "Piezoelectric aluminum nitride vibrating contour-mode MEMS resonators," *J. of Microelectromech. Systems*, vol. 15, no. 6, pp. 1406–1418, Dec. 2006, doi: 10.1109/JMEMS.2006.886012.

[56] A. Lozzi, E. Ting-Ta Yen, P. Muralt, and L. G. Villanueva, "$Al_{0.83}Sc_{0.17}N$ Contour-Mode Resonators with Electromechanical Coupling in Excess of 4.5%," *IEEE Trans. Ultrason. Ferroelectr. Freq. Control*, vol. 66, no. 1, pp. 146–153, Jan. 2019, doi: 10.1109/TUFFC.2018.2882073.

[57] T. Luo et al., "A High-Sensitivity Gravimetric Biosensor Based on S1 Mode Lamb Wave Resonator," *Sensors 2022*, Vol. 22, Page 5912, vol. 22, no. 15, p. 5912, Aug. 2022, doi: 10.3390/S22155912.

[58] M. Reusch, K. Holc, V. Lebedev, N. Kurz, A. Zukauskaite, and O. Ambacher, "Temperature Cross-Sensitivity of AlN-Based Flexural Plate Wave Sensors," *IEEE Sens. J.*, vol. 18, no. 19, pp. 7810–7818, Oct. 2018, doi: 10.1109/JSEN.2018.2853644.

[59] J. Ji et al., "A high sensitive SH-SAW biosensor based 36° Y-X black $LiTaO_3$ for label-free detection of Pseudomonas Aeruginosa," *Sens. Actuators B Chem.*, vol. 281, pp. 757–764, Feb. 2019, doi: 10.1016/J.SNB.2018.10.128.

[60] V. Yantchev and I. Katardjiev, "Thin film Lamb wave resonators in frequency control and sensing applications: A review," *J. of Micromech. and Microeng.*, vol. 23, no. 4. Apr. 2013. doi: 10.1088/0960-1317/23/4/043001.

[61] P. J. Turner et al., "5GHz Band n79 wideband microacoustic filter using thin Lithium Niobate membrane," *Electronic Lett.*, vol. 55, pp. 942–944, 2019, doi: https://doi.org/10.1049/el.2019.1658.

[62] D. Rabus, J. M. Friedt, S. Ballandras, T. Baron, E. Lebrasseur, and E. Carry, “High-overtone bulk-acoustic resonator gravimetric sensitivity: Towards wideband acoustic spectroscopy,” *J. Appl. Phys.*, vol. 118, no. 11, Sep. 2015, doi: 10.1063/1.4930032.

[63] B. P. Sorokin, G. M. Kvashnin, A. V. Telichko, G. I. Gordeev, S. I. Burkov, and V. D. Blank, “Study of high-overtone bulk acoustic resonators based on the Me1/AlN/Me2/(100) diamond piezoelectric layered structure,” *Acoust. Phys.*, vol. 61, no. 4, pp. 422–433, Jul. 2015, doi: 10.1134/S106377101503015X.

[64] E. Redel et al., “Electrochromic bragg mirror: ECBM,” *Advanced Materials*, vol. 24, no. 35, Sep. 2012, doi: 10.1002/adma.201202484.

[65] J. M. Carmona-Cejas, T. Mirea, M. Clement, and J. Olivares, “Comparative study of fully-dielectric acoustic reflectors in solidly mounted resonators,” in *IEEE Intern. Ultrason. Symp., IUS,* Virtual, 2021. doi: https://doi.org/10.1109/IUS52206.2021.9593421.

[66] J. Olivares, E. Wegmann, M. Clement, J. Capilla, E. Iborra, and J. Sangrador, “Wide bandwidth Bragg mirrors for multi-band filter chips,” *Proc. IEEE Ultrason. Symp.*, pp. 2119–2122, 2009, doi: 10.1109/ULTSYM.2009.5441498.

[67] A. Reinhardt et al., “Simulation of BAW resonators frequency adjustment,” in *Proc. - IEEE Ultras. Symp., 2007*, pp. 1444–1447. doi: 10.1109/ULTSYM.2007.363.

[68] R. Aigner et al., “Bulk-acoustic-wave filters: Performance optimization and volume manufacturing,” in *IEEE MTT-S Intern. Microw. Symp. Digest*, 2003, pp. 2001–2004. doi: 10.1109/mwsym.2003.1210552.

[69] C. Han et al., “Solidly mounted resonator sensor for biomolecule detections,” *RSC Adv.*, vol. 9, no. 37, pp. 21323–21328, 2019, doi: 10.1039/c9ra01695c.

[70] J. P. Specht, S. Esfahani, Y. Xing, A. Kock, M. Cole, and J. W. Gardner, “Thermally Modulated CMOS-Compatible Particle Sensor for Air Quality Monitoring,” *IEEE Trans. Instrum. Meas.*, vol. 71, 2022, doi: 10.1109/TIM.2022.3141151.

[71] G. N. Saddik, D. S. Boesch, S. Stemmer, and R. A. York, “Strontium titanate DC electric field switchable and tunable bulk acoustic wave solidly mounted resonator,” in *2008 IEEE MTT-S Intern. Microw. Symp. Digest*, pp. 1263–1266, Sep. 2008, doi: 10.1109/MWSYM.2008.4633289.

[72] J. Olivares, E. Wegmann, M. Clement, J. Capilla, E. Iborra, and J. Sangrador, "Assessment of solidly mounted resonators with wide-band asymmetric acoustic reflectors," *Proc. IEEE Ultrason. Symp.*, pp. 1677–1680, 2010, doi: 10.1109/ULTSYM.2010.5935777.

[73] L. Gordillo-Dagallier et al., "Integration of multilayered graphene on AlN based resonators as a functionalization platform for biosensors," 2017 *Joint Conf. of the European Freq. and Time Forum and IEEE Intern. Freq. Control Symp., EFTF/IFCS 2017 - Proceedings*, pp. 662–665, 2017, doi: 10.1109/FCS.2017.8088995.

[74] M. DeMiguel-Ramos et al., "Gravimetric biosensor based on a 1.3 GHz AlN shear-mode solidly mounted resonator," *Sens. Actuators B Chem.*, vol. 239, pp. 1282–1288, 2017, doi: 10.1016/j.snb.2016.09.079.

[75] J. Capilla, J. Olivares, M. Clement, J. Sangrador, E. Iborra, and A. Devos, "High-acoustic-impedance tantalum oxide layers for insulating acoustic reflectors," *IEEE Trans. Ultrason. Ferroelectr. Freq. Control*, vol. 59, no. 3, pp. 366–372, 2012, doi: 10.1109/TUFFC.2012.2205.

[76] M. Demiguel-Ramos et al., "Hafnium Nitride as High Acoustic Impedance Material for Fully Insulating Acoustic Reflectors," in *IEEE Intern. Ultrason. Symp., IUS, 2018*, pp. 14–17. doi: 10.1109/ULTSYM.2018.8579935.

[77] C. W. Seabury, "United States Patent (19)," 1992.

[78] L. Ma et al., "Bulk acoustic wave resonance characteristic modified by reducing the defects in ZnO-based solidly mounted resonators," *Mater. Sci. Semicond. Process*, vol. 137, p. 106216, Jan. 2022, doi: 10.1016/J.MSSP.2021.106216.

[79] J. Kim, "Low-temperature epitaxial growth of aln thin films on a mo electrode/sapphire substrate using reactive sputtering," *Coatings*, vol. 11, no. 4, Apr. 2021, doi: 10.3390/coatings11040443.

[80] *IEEE Standard on Piezoelectricity: An American National Standard*. ANSI/IEEE Std 176-1987, pp. 8–10, 1988, Accessed: Nov. 16, 2023. [Online]. Available: http://ieeexplore.ieee.org/stamp/stamp.jsp?tp=&arnumber=26560&isnumber=1019

[81] C. L. Wei, Y. C. Chen, C. C. Cheng, and K. S. Kao, "Solidly mounted resonators consisting of a molybdenum and titanium Bragg reflector," *Appl. Phys. A Mater.*

Sci. Process, vol. 90, no. 3, pp. 501–506, Mar. 2008, doi: 10.1007/s00339-007-4312-2.

[82] S. Mahon, "The 5G Effect on RF Filter Technologies," *IEEE Trans. on Semicond. Manuf.*, vol. 30, no. 4, pp. 494–499, Nov. 2017, doi: 10.1109/TSM.2017.2757879.

[83] S. Fanget et al., "Gas sensors based on gravimetric detection - A review," *Sens. Actuators B Chem.*, vol. 160, no. 1, pp. 804–821, Dec. 2011, doi: 10.1016/j.snb.2011.08.066.

[84] Y. Zhu, P. Xia, J. Liu, L. Du, Z. Fang, and Z. Zhao, "PI-Based Dual-Mode FBAR Humidity Sensor Toward Ultra-High Sensitivity and Self-Temperature-Compensation Capability," *IEEE Sens. J.*, vol. 21, no. 23, pp. 26574–26585, Dec. 2021, doi: 10.1109/JSEN.2021.3122805.

[85] *IEEE Standard Definitions of Physical Quantities for Fundamental Frequency and Time Metrology--Random Instabilities.* IEEE Standard 1139, 2008.

[86] F. Akhter, M. E. E. Alahi, H. R. Siddiquei, C. P. Gooneratne, and S. C. Mukhopadhyay, "Graphene Oxide (GO) Coated Impedimetric Gas Sensor for Selective Detection of Carbon Dioxide (CO_2) with Temperature and Humidity Compensation," *IEEE Sens. J.*, vol. 21, no. 4, pp. 4241–4249, Feb. 2021, doi: 10.1109/JSEN.2020.3035795.

[87] S. Ramanavičius, M. Petrulevičiene, J. Juodkazyte, A. Grigucevičiene, and A. Ramanavičius, "Selectivity of Tungsten Oxide Synthesized by Sol-Gel Method Towards Some Volatile Organic Compounds and Gaseous Materials in a Broad Range of Temperatures," *Materials* , vol. 13, no. 3, p. 523, Jan. 2020, doi: 10.3390/MA13030523.

[88] Z. Li et al., "Sb-doped WO_3 based QCM humidity sensor with self-recovery ability for real-time monitoring of respiration and wound," *Sens. Actuators B Chem.*, vol. 361, p. 131691, Jun. 2022, doi: 10.1016/J.SNB.2022.131691.

[89] G. Sauerbrey, "Verwendung von Schwingquarzen zur Wägung dünner Schichten und zur Mikrowägung," *Zeitschrift für Physik*, vol. 155, no. 2, pp. 206–222, 1959, doi: 10.1007/BF01337937.

[90] W. H. King, "Piezoelectric Sorption Detector," *Anal. Chem.*, vol. 36, no. 9, pp. 1735–1739, 1964, doi: 10.1021/ac60215a012.

[91] G. Wingqvist, H. Anderson, C. Lennartsson, T. Weissbach, V. Yantchev, and A. Lloyd Spetz, "On the applicability of high frequency acoustic shear mode biosensing in view of thickness limitations set by the film resonance," *Biosens. Bioelectron.*, vol. 24, no. 11, pp. 3387–3390, Jul. 2009, doi: 10.1016/J.BIOS.2009.04.021.

[92] L. Fan et al., "Influence of surface conductivity on sensitivity of acoustic wave gas sensors based on multilayered structures," *IEEE Trans. Ultrason. Ferroelectr. Freq. Control*, vol. 58, no. 2, pp. 451–460, Feb. 2011, doi: 10.1109/TUFFC.2011.1822.

[93] R. Hoffmann, M. Schreiter, and J. Heitmann, "The concept of thin film bulk acoustic resonators as selective CO_2 gas sensors," *J. of Sensors and Sensor Systems*, vol. 6, no. 1, pp. 87–96, 2017, doi: 10.5194/jsss-6-87-2017.

[94] K. H. Chiu, H. R. Chen, and S. R. S. Huang, "High-performance film bulk acoustic wave pressure and temperature sensors," *Japanese J. of Appl. Phys., Part 1: Reg. Papers and Short Notes and Review Papers*, vol. 46, no. 4 A, pp. 1392–1397, Apr. 2007, doi: 10.1143/JJAP.46.1392.

[95] A. Lin, H. Yu, M. S. Waters, E. S. Kim, and S. D. Goodman, "Explosive trace detection with FBAR-based sensor," *Proc. of the IEEE Intern. Conf. on Micro Electro Mech. Systems (MEMS)*, pp. 208–211, 2008, doi: 10.1109/MEMSYS.2008.4443629.

[96] M. Lindner and M. Schmid, "Thickness Measurement Methods for Physical Vapor Deposited Aluminum Coatings in Packaging Applications: A Review," *Coatings* 2017, Vol. 7, Page 9, vol. 7, no. 1, p. 9, Jan. 2017, doi: 10.3390/COATINGS7010009.

[97] X. Wang, B. Ding, J. Yu, M. Wang, and F. Pan, "A highly sensitive humidity sensor based on a nanofibrous membrane coated quartz crystal microbalance," *Nanotechnology*, vol. 21, no. 5, 2010, doi: 10.1088/0957-4484/21/5/055502.

[98] M. T. S. R. Gomes, P. S. T. Nogueira, and J. A. B. P. Oliveira, "Quantification of CO_2, SO_2, NH_3, and H_2S with a single coated piezoelectric quartz crystal," *Sens. Actuators B Chem.*, vol. 68, no. 1, pp. 218–222, 2000, doi: 10.1016/S0925-4005(00)00432-9.

[99] H. J. Lim, T. Saha, B. T. Tey, W. S. Tan, and C. W. Ooi, "Quartz crystal microbalance-based biosensors as rapid diagnostic devices for infectious

diseases," *Biosens. Bioelectron.*, vol. 168, p. 112513, Nov. 2020, doi: 10.1016/J.BIOS.2020.112513.

[100] B. Liu et al., "Surface acoustic wave devices for sensor applications," *J. of Semicond.*, vol. 37, no. 2, Feb. 01, 2016. doi: 10.1088/1674-4926/37/2/021001.

[101] X. Le et al., "A high performance humidity sensor based on surface acoustic wave and graphene oxide on AlN/Si layered structure," *Sens. Actuators B Chem.*, vol. 255, pp. 2454–2461, Feb. 2018, doi: 10.1016/J.SNB.2017.09.038.

[102] S. Zhgoon et al., "SAW temperature sensor on Quartz," *IEEE Trans. Ultrason. Ferroelectr. Freq. Control*, vol. 62, no. 6, pp. 1066–1075, Jun. 2015, doi: 10.1109/TUFFC.2014.006840.

[103] G. A. Borrero, J. P. Bravo, S. F. Mora, S. Velásquez, and F. E. Segura-Quijano, "Design and fabrication of SAW pressure, temperature and impedance sensors using novel multiphysics simulation models," *Sens. Actuators A Phys.*, vol. 203, pp. 204–214, 2013, doi: 10.1016/j.sna.2013.08.021.

[104] M. Agostini and M. Cecchini, "Ultra-high-frequency (UHF) surface-acoustic-wave (SAW) microfluidics and biosensors," *Nanotechnology*, vol. 32, no. 31. IOP Publishing Ltd, Jul. 01, 2021. doi: 10.1088/1361-6528/abfaba.

[105] S. H. Wang, C. Y. Shen, Z. J. Lien, and J. H. Wang, "Nitric oxide sensing properties of a surface acoustic wave sensor with copper-ion-doped polyaniline/tungsten oxide nanocomposite film," *Sens. Actuators B Chem.*, vol. 243, pp. 1075–1082, May 2017, doi: 10.1016/J.SNB.2016.12.101.

[106] X. L. He et al., "A single FBAR-based temperature and pressure sensors," in *Key Engineering Mater.*, Trans Tech Publications Ltd, 2013, pp. 188–191. doi: 10.4028/www.scientific.net/KEM.562-565.188.

[107] J. Zhao et al., "The research of dual-mode film bulk acoustic resonator for enhancing temperature sensitivity," *Semicond. Sci. Technol.*, vol. 36, no. 2, Feb. 2020, doi: 10.1088/1361-6641/abd15c.

[108] W. Lin et al., "Super-high sensitivity FBAR temperature sensor based on size effect of Ti insertion layer," *Mater. Res. Express*, vol. 8, no. 9, p. 095701, Sep. 2021, doi: 10.1088/2053-1591/AC2099.

[109] J. Liu et al., “A microfabricated thickness shear mode electroacoustic resonator for the label-free detection of cardiac troponin in serum,” *Talanta*, vol. 215, p. 120890, Aug. 2020, doi: 10.1016/j.talanta.2020.120890.

[110] E. Wajs, G. Rughoobur, K. Burling, A. George, A. J. Flewitt, and V. J. Gnanapragasam, “A novel split mode TFBAR device for quantitative measurements of prostate specific antigen in a small sample of whole blood,” *Nanoscale*, vol. 12, no. 17, pp. 9647–9652, May 2020, doi: 10.1039/D0NR00416B.

[111] A. Kumar and R. Prajesh, “The potential of acoustic wave devices for gas sensing applications,” *Sens. Actuators A Phys.*, vol. 339, p. 113498, Jun. 2022, doi: 10.1016/J.SNA.2022.113498.

[112] S. Song et al., “Film bulk acoustic formaldehyde sensor with polyethyleneimine-modified single-wall carbon nanotubes as sensitive layer,” *Sens. Actuators B Chem.*, vol. 266, pp. 204–212, Aug. 2018, doi: 10.1016/j.snb.2018.03.129.

[113] D. Chen, J. J. Wang, D. H. Li, and Y. Xu, “Hydrogen sensor based on Pd-functionalized film bulk acoustic resonator,” *Sens. and Actuators, B Chem.*, vol. 159, no. 1. pp. 234–237, 2011. doi: 10.1016/j.snb.2011.06.078.

[114] Y. Chang, Z. Hui, X. Wang, H. Qu, W. Pang, and X. Duan, “Dual-Mode Gas Sensor Composed of a Silicon Nanoribbon Field Effect Transistor and a Bulk Acoustic Wave Resonator: A Case Study in Freons,” *Sensors 2018*, Vol. 18, Page 343, vol. 18, no. 2, p. 343, Jan. 2018, doi: 10.3390/S18020343.

[115] X. Qiu, R. Tang, J. Zhu, H. Yu, J. Oiler, and Z. Wang, “Acetone sensor based on film bulk acoustic resonator,” *Proc. of IEEE Sensors*, pp. 1546–1549, 2010, doi: 10.1109/ICSENS.2010.5690310.

[116] A. Ghosh, C. Zhang, S. Q. Shi, and H. Zhang, “High-Temperature Gas Sensors for Harsh Environment Applications: A Review,” *Clean (Weinh),* vol. 47, no. 8, p. 1800491, Aug. 2019, doi: 10.1002/CLEN.201800491.

[117] S. A. Zhgoon, A. S. Shvetsov, S. A. Sakharov, and O. Elmazria, “High-Temperature SAW Resonator Sensors: Electrode Design Specifics,” *IEEE Trans. Ultrason. Ferroelectr. Freq. Control*, vol. 65, no. 4, pp. 657–664, Apr. 2018, doi: 10.1109/TUFFC.2018.2797093.

[118] J. A. Thiele and M. P. Da Cunha, “High temperature LGS SAW gas sensor,” *Sens. Actuators B Chem.*, vol. 113, no. 2, pp. 816–822, Feb. 2006, doi: 10.1016/J.SNB.2005.03.071.

[119] P. Zheng, T. L. Chin, D. Greve, I. Oppenheim, V. Malone, and L. Cao, “High-temperature langasite SAW oxygen sensor,” *IEEE Trans. Ultrason. Ferroelectr. Freq. Control*, vol. 58, no. 8, pp. 1538–1540, Aug. 2011, doi: 10.1109/TUFFC.2011.1979.

[120] A. Ghosh, C. Zhang, S. Shi, and H. Zhang, “High temperature CO_2 sensing and its cross-sensitivity towards H_2 and CO gas using calcium doped ZnO thin film coated langasite SAW sensor,” *Sens. Actuators B Chem.*, vol. 301, p. 126958, Dec. 2019, doi: 10.1016/J.SNB.2019.126958.

[121] H. Seh, T. Hyodo, and H. L. Tuller, “Bulk acoustic wave resonator as a sensing platform for NO_x at high temperatures,” *Sens. Actuators B Chem.*, vol. 108, no. 1–2, pp. 547–552, Jul. 2005, doi: 10.1016/J.SNB.2004.11.083.

[122] G. Zeng et al., “Detection and Discrimination of Volatile Organic Compounds using a Single Film Bulk Acoustic Wave Resonator with Temperature Modulation as a Multiparameter Virtual Sensor Array,” *ACS Sens.*, vol. 4, no. 6, pp. 1524–1533, Jun. 2019, doi: 10.1021/acssensors.8b01678.

[123] T. Mirea, J. Olivares, M. Clement, J. L. Olivera, J. Sangrador, and E. Iborra, “AlN-solidly mounted resonators sustaining up to 1000°C with TCF compensation,” *2017 Joint Conf. of the European Freq. and Time Forum and IEEE Intern. Freq. Control Symp., EFTF/IFC 2017 - Proceedings*, pp. 519–522, 2017, doi: 10.1109/FCS.2017.8088947.

[124] T. Mirea, J. Olivares, M. Clement and J. Sangrador, “AlN-based solidly mounted resonators at 400°C: In-situ performance monitoring,” *IEEE Intern. Ultras. Symp., IUS*, 1700–1702, Oct. 2019 https://doi.org/10.1109/ULTSYM.2019.8925697.

2

FABRICATION AND CHARACTERIZATION TECHNIQUES

In this chapter, the fabrication and characterization techniques used during this thesis are described. To manufacture SMR devices, it is necessary to know how to operate several microfabrication techniques, as it is a process that involves many steps. For this thesis, most of the steps require sputtering deposition and/or photolithography and etching processes. However, in some cases, other techniques such as thermal evaporation or chemical vapor deposition are needed.

Furthermore, the characterization techniques used to assess some of the most relevant properties of the materials involved in SMR fabrication are also described in this chapter. X-Ray techniques like X-ray diffraction and X-ray reflectometry, and Raman spectroscopy, are the ones utilized for extracting information about crystalline properties. Rutherford backscattering spectroscopy technique is also depicted, which is mainly used to study atomic composition. Imaging techniques for studying surface topography like atomic force and scanning electron microscopies are described. Concerning the electrical characterization and the performance of the devices, the description of the techniques used during the thesis is also included in this chapter. Finally, the last section covers the design of a gas sensing setup to be used as the main characterization tool to assess the performance of the SMR sensors manufactured within the context of this work. As indicated in Chapter 1, one of the main objectives of this thesis is to design, manufacture, and test a characterization setup capable of generating controllable gas atmospheres in different temperature ranges, and its use is essential to meet the rest of the established main objectives.

2.1. FABRICATION TECHNIQUES

The most relevant fabrication techniques for the manufacture of the SMR-based sensors are included in this section. A brief explanation of the fundamentals behind each technique can also be found. The specific parameter values for the SMR sensor fabrication steps will be discussed in Chapter 3.

2.1.1. Sputtering deposition

Physical vapor deposition (PVD) techniques are central to thin film technologies, as they are used in numerous fabrication processes involving mostly metallic, but also dielectric layers and semiconductors. Within the PVD family, sputtering deposition is characterized by the use of a sputtering gas between two electrodes, typically Ar, that is turned into plasma inside the sputtering chamber. Subsequently, Ar^+ ions are directed towards a solid target (cathode), causing atoms from the target to scatter as a result of collisions with the high-energy ions. The scattered atoms then are deposited on the surface of the substrate (anode) forming a thin film. The plasma needs to be generated by a power supply, which creates an electric field between the cathode and the anode. Depending on the applied voltage between the electrodes, the sputtering system can be classified as either DC, pulsed DC, or RF sputtering [1].

The deposition rates of these processes are relatively low compared to other thin film deposition techniques, like certain types of thermal evaporation. This issue can be overcome by lowering the sputtering pressure. By introducing magnetron-type systems, it is possible to work in lower sputtering pressure conditions than with typical DC or RF systems. A diagram of the inside of a magnetron-type sputtering system is shown in Figure 2.1. In these systems, a magnetic field parallel to the cathode generates a trapping effect to the electrons in the plasma, allowing more collisions with the sputtering gas atoms. Therefore, this effect increases the plasma density, which also increases the sputtering rate at the target. As the sputtered particles travel with lower collision rate from the cathode to the anode, the overall deposition rate is increased [1].

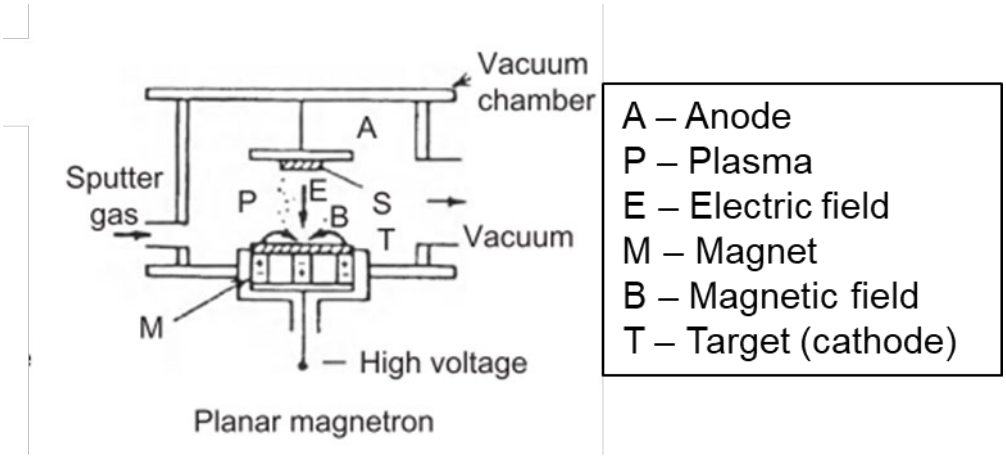

Figure 2.1. Typical magnetron spattering configuration [1].

Using a high purity metallic target and an inert gas like Ar as sputtering gas, the process will result in the deposition of a metallic film on the substrate. However, dielectric materials can be achieved in two different ways: by using compound targets or by introducing reactive gases inside the sputtering chamber. The latter is called reactive sputtering. By introducing gases like O_2 and N_2, it is possible to obtain SiO_2 and AlN films, to name a few [2]. For sputtering processes regarding deposition of dielectric films, DC voltage cannot sustain the sputtering process as positive charged ions would accumulate on the insulating material, repelling the Ar+ ions and switching the glowing discharge (plasma) off. To overcome this problem, RF and pulsed DC voltages can be applied, as this can ensure that the target is not positively charged, and therefore a successful deposition of insulators [1], [3].

Besides the applied voltage, there are other parameters that can be tuned during deposition and are of extreme relevance to obtain thin films with the appropriate characteristics for the desired application. Applied power to the target, initial chamber pressure, gas flow to control sputtering pressure and distance between target and substrate are some of the most important parameters to control in a sputtering process. The temperature of the substrate or the application of a substrate bias can also be important, specially to obtain films with improved crystalline orientations [4]. In reactive processes, the ratio between Ar and the reactive gas is also crucial to tune the stoichiometry of the resultant films [5]. Other less common parameters have also been explored during the last years, such as the angle between the target and the substrate, which has given name to a technique called Glancing Angle Deposition [6].

In this thesis, four different sputtering systems have been used. Most of the materials were deposited using a Leybold Z-550 sputtering system (shown in Figure 2.2). It uses a pulsed DC power supply, and both metallic and reactive sputtering operation are allowed. The chamber is pumped by a rotatory and turbomolecular pumps to the 10^{-4} Pa range. The most important feature of this system is that multiple targets are installed inside the chamber in separate positions, so that multilayer processes can be carried out without breaking vacuum. The targets are 6 inches in diameter and the target-substrate distance is 4.8 cm. The system also allows for substrate heating during deposition, although all the processes for this thesis were conducted without intentional heating of the substrate. Regarding SMR fabrication, this system was utilized for SiO_2, Ti, Mo (acoustic reflector and electrode), AlN (acoustic reflector), Ta_2O_5 and ZnO thin films. As it will be discussed in Chapter 4, WO_3 thin films were also deposited on the surface of the SMRs to act as a nitric oxide (NO) sensing layer.

Figure 2.2. Leybold Z-550 sputtering system.

A similar sputtering tool was used for the deposition of Au thin films to act as part of the top electrode (passivation) in high temperature operation sensors, as it will be further discussed in forthcoming chapters. A photograph of the system, named MRC, is featured in Figure 2.3. Similar to the Z-550, it works under pulsed DC voltage operation and the target-substrate distance is 8.0 cm. Multiple targets can also be utilized without breaking vacuum. However, the Au target for this system is 3 inches in diameter. Before sputtering process initialization, the system is also pumped down to the 10^{-4} Pa range with a rotatory and turbomolecular pumps.

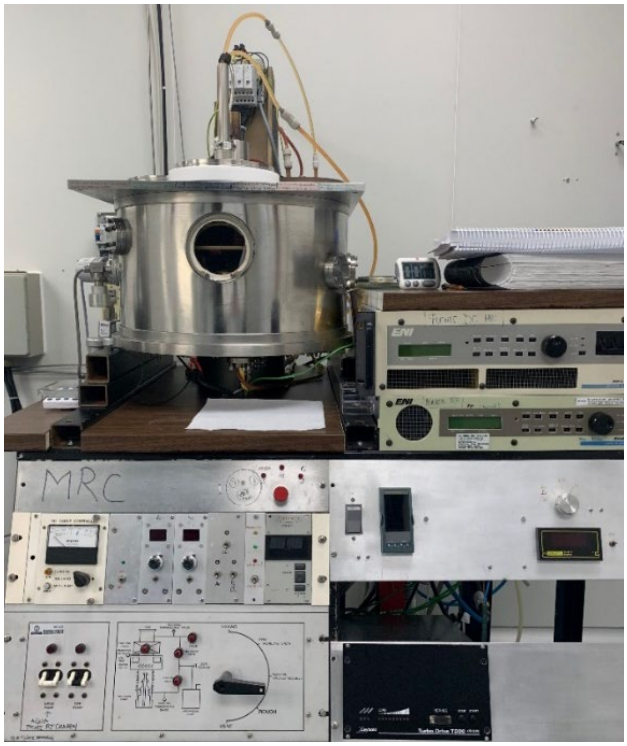

Figure 2.3. MRC sputtering system.

For piezoelectric thin films, an in-house ultra-high vacuum sputtering tool, with the nickname 'MAREA' (Figure 2.4), was used. It presents a dual chamber configuration, with the goal of obtaining the best possible vacuum conditions for the growth of high quality AlN piezoelectric films. The first chamber is utilized to load the substrates, and it can be pumped down to 10^{-4} Pa in short time with a rotatory and turbomolecular pumps. Then, the samples are transported to the deposition chamber, which can be pumped down to 10^{-6} Pa with the help of a cryogenic pump. The resulting films are sputtered from a 99.999 % Al target with a diameter of 6 inches and a cathode-substrate distance of 5.5 cm. The substrate holder allows for substrate heating and RF bias. A detailed description of the deposition processes carried out for this thesis is given in the next chapter.

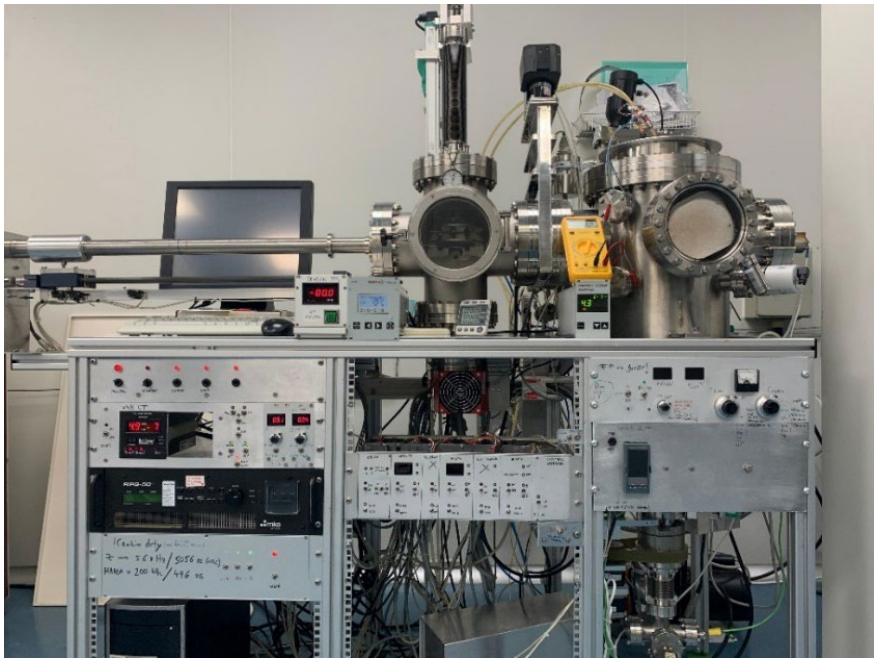

Figure 2.4. Ultra-high vacuum sputtering system for deposition of piezoelectric AlN films (MAREA).

The last sputtering system used for this thesis was the High Target Utilization Sputtering system (HiTUS), located in the cleanroom of the Electrical Engineering Department, University of Cambridge. It was mainly used for the fabrication of HfN/SiO_2 acoustic reflectors. A photograph of a HiTUS-type tool is depicted in Figure 2.5. It works under RF power supply, and the special feature of this type of sputtering system is that Ar plasma is generated outside the deposition chamber, which enables extra set of parameters for tuning plasma generation and management, leading to very low stress thin films even in multilayer processes. Similar to some of the already mentioned equipment, its chamber allows for multi target operation without breaking vacuum, which is ideal for SMR fabrication routes. Specific sputtering conditions for the HfN/SiO_2 stack is detailed in next chapter.

Figure 2.5. HiTUS sputtering system [7].

2.1.2. Thermal evaporation

Thermal evaporation is a PVD process in which a vaporization source is heated, and the released atoms or molecules reach the substrate with almost no collision from gas molecules due to the previously generated vacuum in the deposition chamber. In these processes, radiant energy from the evaporation source to the substrate needs to be avoided, so the source-substrate distance needs to be large enough to prevent this effect [8]. The thermal evaporation system used in this thesis is represented in Figure 2.6. After loading the sample, the deposition chamber is pumped down to 10^{-5} Pa to ensure good vacuum conditions during deposition. Two different methods for heating can be used: the most common one is the resistive heating method, in which the evaporation source is in contact with a hot surface, heated by Joule effect. The other method is the electron beam (e-beam) heating method, which is necessary for materials that require higher temperature to evaporate. Using an e-beam generator, consisting of a thermionic-emitting filament and high voltages to generate accelerated electrons, and electromagnetic fields to focus the beam onto the evaporation source, it is possible to apply higher energies than the ones provided with resistive heating [8].

Figure 2.6. Leybold L-560 thermal evaporation system.

E-beam heating was used to evaporate the Ir bottom electrodes on acoustic reflectors to manufacture the SMR devices used for this thesis. Resistive heating was mainly used for the evaporation process of pentacene films to act as sensing layers of NO at room temperature [9].

2.1.3. Chemical vapor deposition

Chemical vapor deposition (CVD) is a deposition process in which a thin film is deposited on a substrate after a chemical reaction involving volatile precursors is produced. These precursors are usually reactive gases that are injected into the CVD chamber. By adjusting experimental parameters such as substrate temperature, process pressure, composition of reactive gas mixture and gas flows, etc. it is possible to control the physical and chemical properties of the materials grown [10]. This deposition method is used nowadays to grow many different materials such as graphene [11], $LiNbO_3$ [12] or metal oxides [13], to name a few. In this thesis, the CVD system in Figure 2.7 was used for the selective growth of carbon nanotube (CNT) forests on the top electrode of SMRs for sensor applications [14].

Figure 2.7. Customized CVD tool for CNT growth.

2.1.4. Photolithography and etching techniques

Devices based on thin film technology usually have designs that require patterning techniques to be functional. For this purpose, photolithography and etching techniques are of key importance in microfabrication technologies. In a nutshell, photolithography uses the properties of certain photoresists to create patterns after illuminating them with a light of a specific wavelength. There are many types of lithography techniques, based on the energy source used to illuminate the photoresist, such as optical (or near optical) photolithography [15], which is the most common one, e-beam lithography [16] or X-ray lithography [17].

For the processes carried out in this thesis, optical photolithography using UV-light source was the technique of choice. The most common photoresists used for optical lithography are based on polymethyl methacrylate (PMMA) [18] and polydimethylglutarimide (PMGI) [19]. A typical lithography process starts by spincoating the surface of the sample with the photoresist, and doing a short-time heating treatment, called soft bake, to evaporate the solvent of the photoresist and make it more solid. Then, the photoresist is exposed to the UV-light source through a photolithography mask to only illuminate certain areas of the sample to create the desired pattern. This process is carried out using a mask aligner (see Figure 2.8).

Figure 2.8. Karl Suss mask aligner with UV-light source.

Photoresists can be either positive or negative: positive photoresists become more soluble after UV exposition, so it is possible to remove it from the surface of the sample using the appropriate developer, whereas negative photoresists present the opposite behavior: the soluble regions are the ones not exposed to UV light. Once the pattern is defined, the goal of the photoresist is to protect the underlying parts of the sample, so the etching process only removes the part of the material exposed to the etching agent, like it is represented in Figure 2.9, showing also the differences between positive and negative processes.

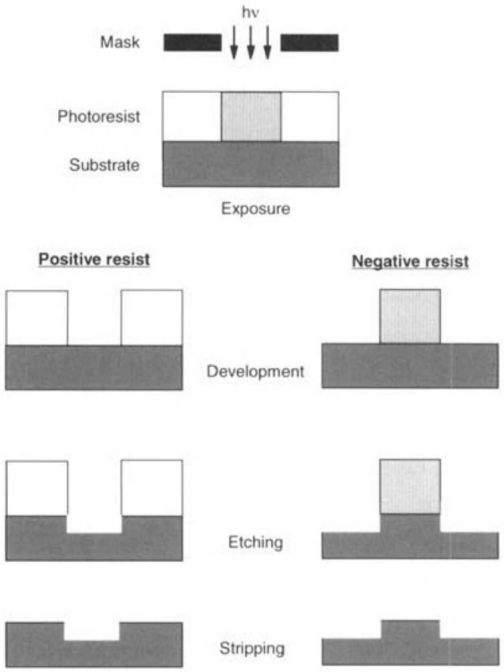

Figure 2.9. Differences in patterning process between positive and negative photoresists [20].

Depending on the target material, the photoresist or even the type of the device to manufacture, etching processes can differ significantly from one another. An easy way of classifying them could be as wet or dry etching. Wet etching happens when the sample is submerged in a solution and the material is removed from the sample through a chemical process. On the other hand, dry etching, like sputter or reactive ion etching (RIE) consists in generating a plasma to remove the exposed material by bombarding it with energetic ions. Sputter etching normally uses an Ar plasma, whereas RIE uses a reactive gas to chemically etch the target material, like SF_6 or CHF_3. The dry etching equipment showed in Figure 2.10 allows the possibility of using both techniques. Depending on the RIE etching recipe, masks based on other materials, besides photoresist, might be needed.

Figure 2.10. Dry Etching system.

The last patterning method covered in this thesis is the lift-off process. With this method, the photoresist is developed prior to the deposition of the target material on the sample. After deposition, the photoresist is removed and with it the parts of material deposited on top of it, leaving as pattern the previously uncoated areas with the photoresist, as shown in Figure 2.11. Depending on the deposition techniques involved in the fabrication route, this method can be the more straightforward as no etching techniques are required. For certain devices, it is also the best way to ensure that no short-circuits are left when defining their electrodes.

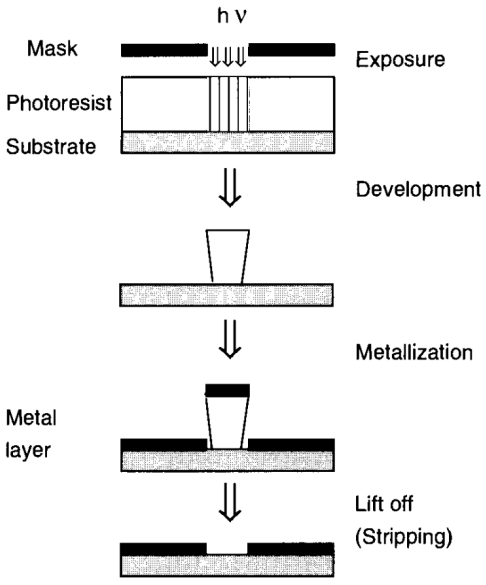

Figure 4-22. Process flow of the lift-off process.

Figure 2.11. Diagram of a typical lift-off process [20].

2.2. CHARACTERIZATION TECHNIQUES

This section contains the most important characterization techniques used to assess some of the most relevant properties of the materials involved in the fabrication of the SMR sensors manufactured during this thesis. The techniques used to evaluate the response of the resonators and their performance as sensors are also included here.

2.2.1. X-Ray diffraction and reflectometry

X-ray diffraction (XRD) is the most common technique to characterize crystalline structure in materials. This technique works by exposing the target material to an X-ray beam. If the atoms of the material follow a periodic arrangement, i.e., they show crystalline structure, the XRD diffractogram will show peaks at certain angles. These peaks correspond to the reflections of the X-rays with the diffraction planes of the crystalline material, following Bragg's law [21]:

$$n\lambda = 2d\sin\theta \tag{2.1}$$

Where λ is the wavelength of the X-rays, θ is the incident angle and d is the distance between the specific set of diffraction planes that causes the reflection peak. The crystalline structure of any given material can be described using sets of infinite planes that are orthogonal to certain crystalline directions, which are also labeled using their Miller indexes [21]. Therefore, using Bragg's law it is possible to know which planes are present in a sample by knowing at which angles they show a reflection.

As discussed in Chapter 1, piezoelectric effect is heavily dependent on the crystalline structure of the material. In fact, the presence of certain reflections is related to the appearance of certain resonances. In this thesis, XRD scans were used to assess the crystal orientation of AlN and AlScN piezoelectric films. As they are both arranged in wurtzite structure, their crystal orientation will be denoted by peaks in similar positions. For instance, high c-oriented grains show a high intensity (00·2) peak in $\theta - 2\theta$ reflection patterns [4], [22]. On the other hand, the presence of (10·1), (10·2) and (10·3) reflections indicates that the material has several tilted grains, which reduces the quality of the longitudinal modes but can lead to the appearance of shear modes. In Figure 2.12, the XRD patterns of AlN and $Al_{0.3}Sc_{0.7}N$

thin films grown on Si substrates are shown. The y-axis is represented in logarithmic scale. As it can be observed, both films show good c-axis orientation as their (00·2) reflections (centered around $2\theta = 36°$) are sharp and with high intensity relative to the rest of the peaks. As it will be discussed in next chapter, the inclusion of Sc atoms in the wurtzite structure of AlN causes a shift to lower 2θ angles.

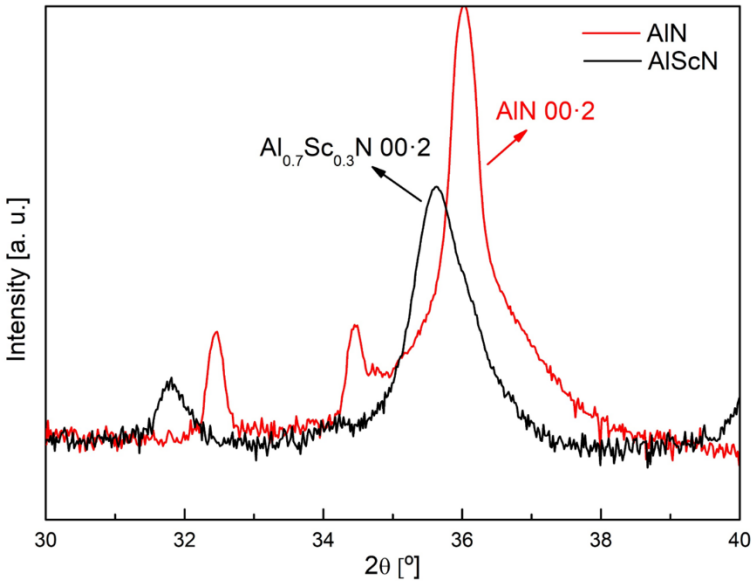

Figure 2.12. AlN and $Al_{0.7}Sc_{0.3}N$ XRD patterns.

To analyze the resulting diffractograms, the observed XRD peaks were fitted using pseudo-Voigt functions, which are the linear combination of Gaussian and Lorentzian curves. These functions have the following expression:

$$pV(x) = \eta \frac{1}{\sigma\sqrt{2\pi}} e^{-\frac{x-x_0}{2\sigma^2}} + (1-\eta)\frac{1}{\pi}\frac{\Gamma/2}{(x-x_0)^2 + (\Gamma/2)^2} \qquad (2.2)$$

where η is the parameter that shifts the profile more towards Gaussian or Lorentzian when approaching to 1 or 0, respectively. The rest of the parameters are the position of the maximum, x_0, the standard deviation of the Gaussian profile, σ, and the full width at half maximum (FWHM), Γ. All the fitting processes were carried out with the help of the `lmfit` library in Python [23]. Using the built-in models from this library, it is possible to fit an XRD pattern based on a set of starting parameters. These parameters are the number of functions, and their x_0, FWHM and height. If necessary, a baseline element can be added. Then, a least squares method is employed to fit these parameters, together with their fitting errors. An example of the result of a fitting process is shown in Figure 2.13. In this case, the process led to a deconvolution of one of the observed peaks into two pseudo-Voigt functions, with

the third peak being sufficiently separated. The obtained parameters for these functions are gathered in Table 2.1.

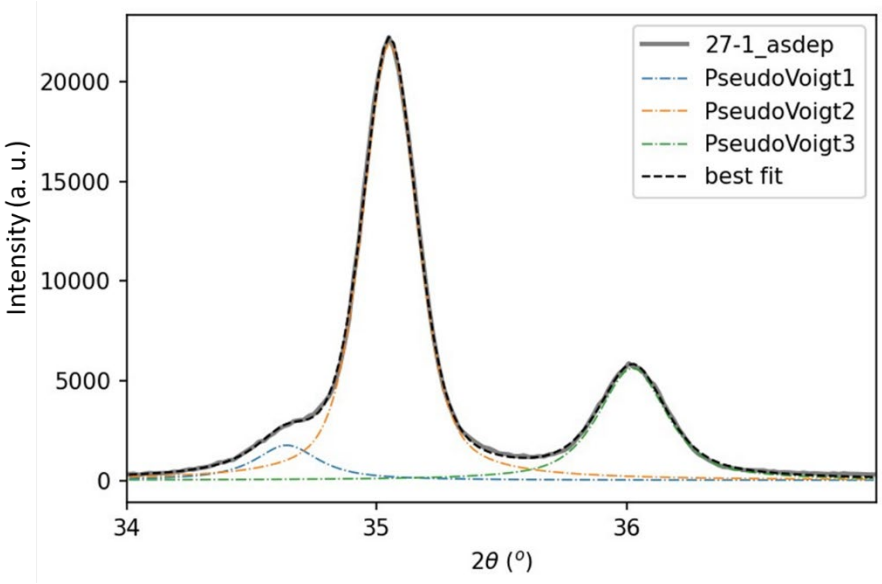

Figure 2.13. $Al_{0.7}Sc_{0.3}N$ XRD pattern fit.

Table 2.1. Fitting parameters for the functions used in the fitting process.

Parameters	Pseudo-Voigt 1	Pseudo-Voigt 2	Pseudo-Voigt 3
x_0	34.64	35.05	36.02
Height	1761.52	21961.31	5630.82
FWHM	0.30	0.26	0.32
η	0.91	0.60	0.75

A complementary measure of the quality of the crystalline structure is the Rocking Curve (RC) measurement. In this case, the incident beam and the detector are fixed at the specific angle of the reflection we aim to evaluate, and the sample is rocked (rotated) to measure the grade of misorientation of the diffraction planes. Good orientation is indicated by a low value in the FWHM values of the RC measurements. For AlN and AlScN 00·2 reflections, good FWHM are in the range of 1-2° [24]. The RC measurement for the AlN 00·2 reflection from Figure 2.12 is represented in Figure 2.14 with its FWHM value, indicating great crystalline orientation for the displaying of longitudinal modes in piezoelectric response. In this thesis, RCs of $Al_{0.7}Sc_{0.3}N$ 00·2 reflections were performed to study their homogeneity and thermal stability after being subjected to high temperatures. To obtain the FWHM value and the position of the peak, the RC data was fitted to Gaussian functions using the `lmfit` library in Python, in a similar process to the one employed for the $\theta - 2\theta$ pattern fittings.

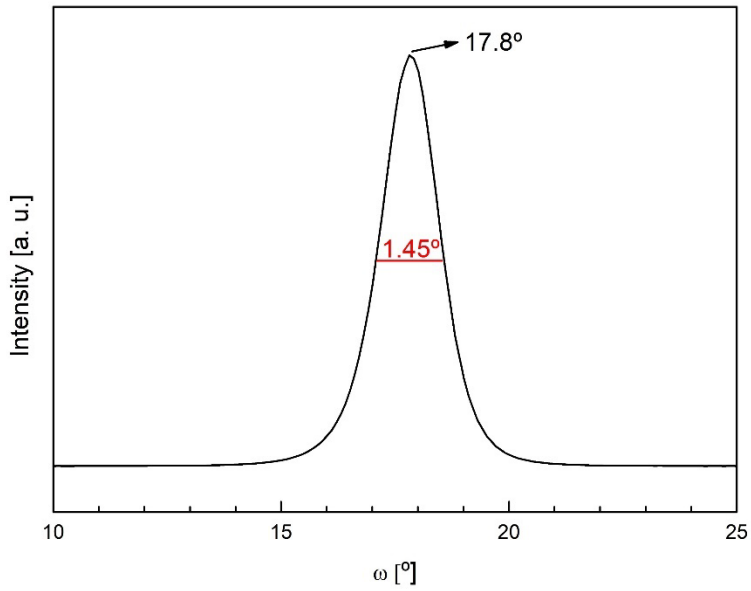

Figure 2.14. AlN 00·2 rocking curve.

The last X-Ray technique utilized in this thesis is X-Ray reflectometry (XRR). This technique is based on the measurement of the intensity of reflected X-Rays from a flat surface for low reflection angles. When the reflection angle is greater than the critical angle, incident rays penetrate into the material by refraction and therefore the intensity of the reflected beam decays dramatically. This critical angle is strongly related to the density of the material, and it can be expressed as:

$$\theta_c = \sqrt{\frac{r_0 \lambda^2}{\pi}\rho} \tag{2.3}$$

where r_0 is the Bohr radius and λ the wavelength of the incident radiation. In addition to density, with XRR it is possible to measure different film properties such as film thickness and roughness [25]. Furthermore, each property is associated to a specific part of the XRR measurement. Figure 2.15 shows an XRR measurement from an AlN thin film deposited on Si substrate. As already mentioned, by locating the position of the critical angle it is possible to obtain the density of the material. To obtain the roughness, it is necessary to fit the slope of the decay in intensity. The thickness of the film can be estimated by fitting the fringes in the experimental curve. However, in this case no fringes appear due to the AlN film being too thick, as the size of the fringes is inversely correlated with the thickness of the measured film.

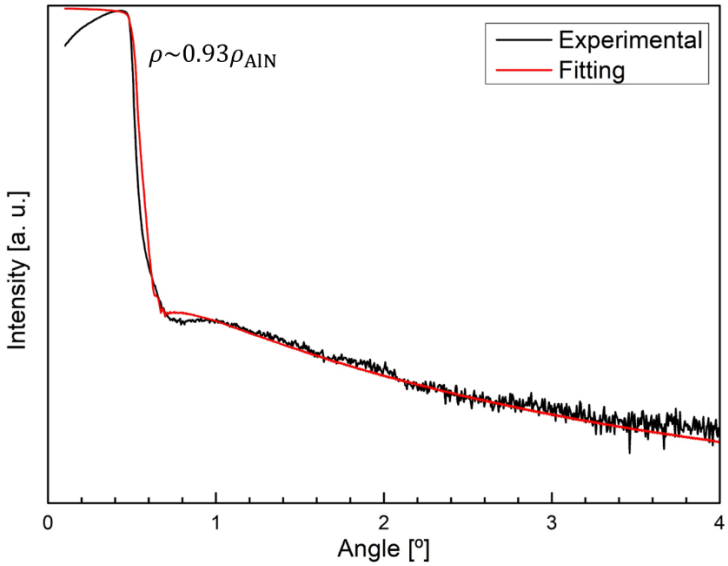

Figure 2.15. AlN XRR measurement and fitting.

XRR measurements were mainly used to estimate the densities of some of the materials composing the acoustic reflectors. All the results were obtained by fitting the experimental curves using RCRefSim software [26].

XRD, RC and XRR measurements carried out in this thesis were made in an X'PERT PRO-MRD high resolution diffractometer provided with a Cu anode at the CAI Técnicas Químicas, Universidad Complutense de Madrid.

2.2.2. Raman Spectroscopy

Crystalline structure can be assessed using Raman spectroscopy. Most of the photons from an incident light source (usually a laser) get reflected, absorbed or transmitted when they interact with the surface of a semiconductor. There is also an amount of them that are scattered in a Rayleigh process, i.e., they preserved their energy after the scattering process. However, a small amount of the photons undergoes an inelastic scattering process due to the interaction with the phonons of the target material. Therefore, the scattered photons have different energy than the incident. Depending on whether they lose or gain energy, the process is called Stokes and anti-Stokes scattering, respectively.

Since this technique measures the interaction between the photons and the phonons of the material, important information about the crystalline structure can be extracted from Raman measurements. In this thesis, Raman spectroscopy was

mainly used to characterize some of the sensing layers that were integrated onto the SMRs. In Figure 2.16, a typical Raman spectrum from the sputtered WO_3 thin films used as NO sensing layers at high temperature is showed. Each peak corresponds to a phonon interaction and, as it will be discussed in next chapter, are related to the monoclinic phase of WO_3 [27].

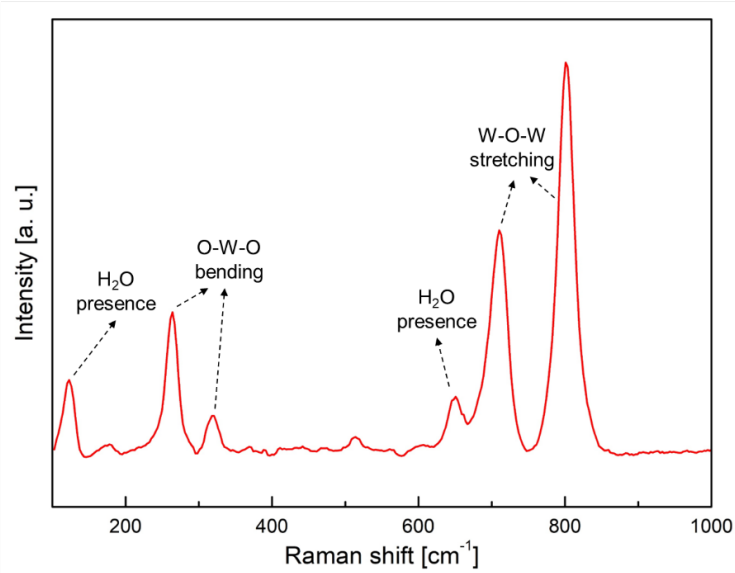

Figure 2.16. Raman spectrum of a WO_3 thin film.

Raman spectroscopy can be used not only for inorganic semiconductors, but for other types of materials, too. For instance, it is the standard technique to assess quality of graphene layers, and thus CNT quality, too [28], [29]. It can also be used for identifying the structure of certain polymers, such as pentacene [30]. In this thesis, Raman spectroscopy was employed to assess the structure of sputtered WO_3 and evaporated pentacene films.

To analyze the measured spectra, standard data treatment techniques were used using Python. First, the baseline of the results was calculated using asymmetrical least squares method and subtracted [31]. Then, to remove unwanted noise, a smoothing process was performed using the Savitzky-Golay algorithm. Since no presence of remarkable convoluted peaks was observed in the measured spectra for the different samples, no deconvolution methods were performed.

2.2.3. Rutherford backscattering spectroscopy

Characterizing the atomic composition of a sample can be extremely useful when studying properties such as homogeneity, and stoichiometry. One of the techniques used for this purpose is Rutherford backscattering spectroscopy (RBS), in which an energetic beam of particles collides with the atoms from the sample and the scattered particles are detected and quantified. The incident beam is usually made of He nuclei, although protons or other light particles are commonly used, in the MeV range. With RBS, it is possible to study, in addition to atomic composition, the depth profile of the sample off to 1 μm. This could include layer thickness, atomic diffusion, or analysis about the impurities of the sample [32].

In RBS, the incident particles, after interacting with the target material, experience an elastic backscattering process. A representation of this process is shown in Figure 2.17. In this type of interaction, the conservation of momentum and energy can be used for deriving the kinematic factor K, which is the ratio between the energies of the incident ion before and after collision.

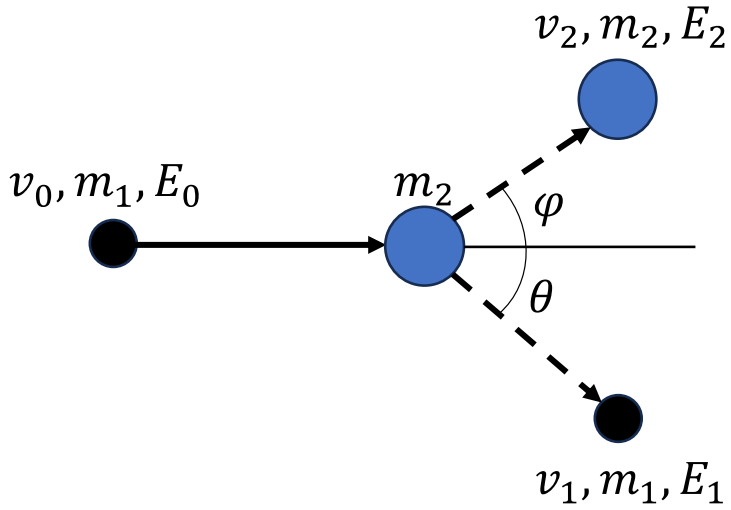

Figure 2.17. Classical kinematic collision.

The kinematic factor follows the expression:

$$K = \frac{E_1}{E_0} = \left[\frac{\sqrt{m_2^2 - m_1^2 \sin^2\theta} + m_1 \cos\theta}{m_1 + m_2}\right]^2 \tag{2.4}$$

where $m_2 > m_1$. The energy of the backscattered ion will be determined by the kinematic factor. For thin film measurements, a typical RBS setup is showcased

in Figure 2.18. In this case, the resulting energy also depends on how deep the incident ion penetrates into the film. Therefore, the energy is given by:

$$E_1 = K(E_0 - \Delta E_{in}) - \Delta E_{out} \tag{2.5}$$

where ΔE_{in} and ΔE_{out} are the energies lost by the particle while traveling in the material.

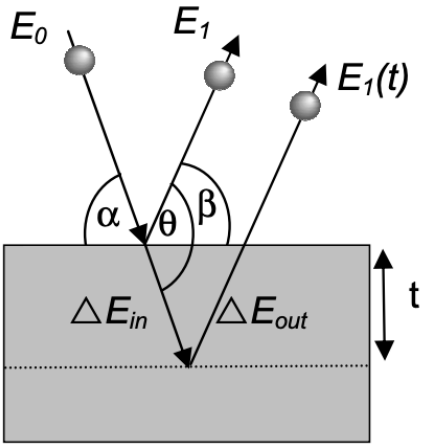

Figure 2.18. Typical RBS setup for thin film assessment [33].

The intensity of the signal corresponding to a determined element is given by its backscattering yield. If the element with highest atomic number, Z_{max}, is known, the relative height of a given element is:

$$\sigma_{rel} = \left(\frac{Z_x}{Z_{max}}\right)^2 \tag{2.6}$$

For samples composed of two or more elements, the backscattering yield increases with the concentration of the element:

$$Y_{rel} = \sigma_{rel} x_{rel} \tag{2.7}$$

In this technique, the incident energy plays an important role in the obtained measurement as some scattering processes are more likely to happen at certain energies. Specially for light elements, their scattering cross-section increases at certain incident energies as they start to deviate from standard Rutherford backscattering processes. These energies are called resonances [34]. For instance, whereas for the represented RBS spectrum at 2.3 MeV in Figure 2.19(a) the presence of light elements is not observed, when the energy of the incident particles is raised to 3.038 MeV, an oxygen resonance can be observed at around 350 in channel (corresponding to 1090 keV in energy), as depicted in Figure 2.19(b). The rest of the

RBS spectrum is similar to the ones measured at different energies because the sample is composed of heavier elements, which always show good sensitivity in RBS processes.

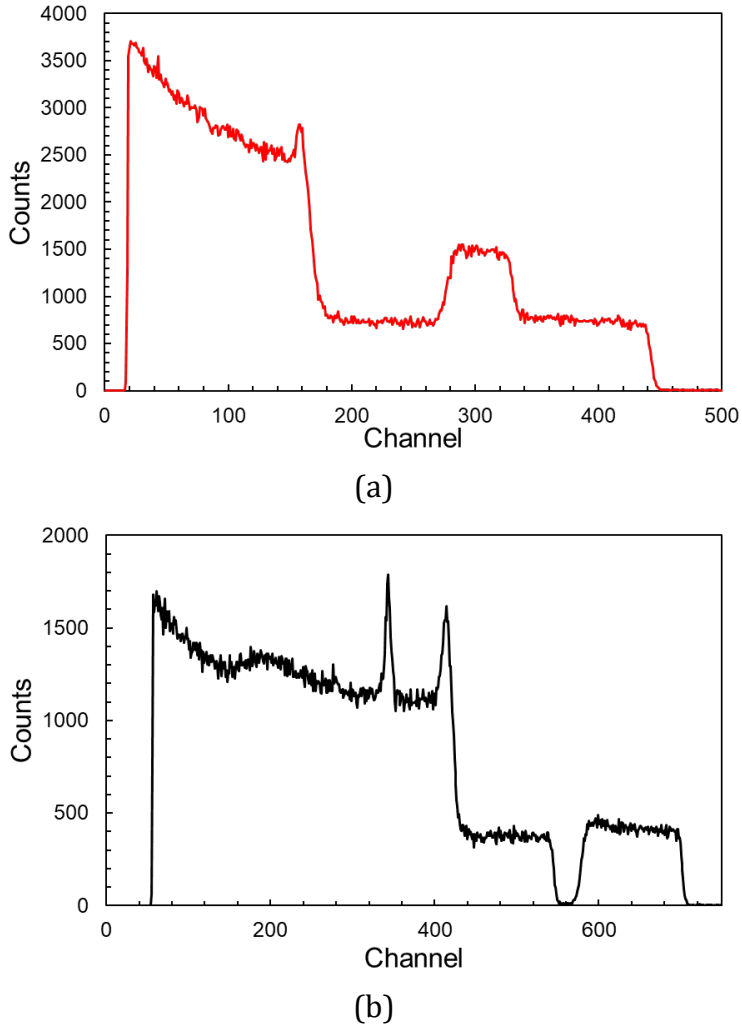

Figure 2.19. (a) RBS spectrum of $Al_{0.7}Sc_{0.3}N$ thin film at 2.3 MeV and (b) at 3.038 MeV.

To analyze the measurements, it is necessary to know the elements present in the sample and the calibration data from the experimental setup. It is possible to establish the relation between channel and energy from the channel where two known elements are located and their energy:

$$\frac{\text{Energy}}{\text{channel}} = \frac{\Delta E_{ch}}{\Delta\text{channel number}} \tag{2.8}$$

It is also possible to calculate the energy at channel zero (*offset*):

$$E_{ch0} = E_{chx} - \alpha \cdot (\text{channel number}) \tag{2.9}$$

where E_{chx} is the channel energy of element x and α is channel resolution (kEV/channel). Figure 2.20 shows the fitted spectra of an $Al_{0.7}Sc_{0.3}N$ sample on Si substrate, where the contribution from each element to the overall fit is depicted. The relation between energy and channel is also shown. At lower energies, the fitting function deviates from the experimental data because the fitting procedure only considerates binary scattering processes.

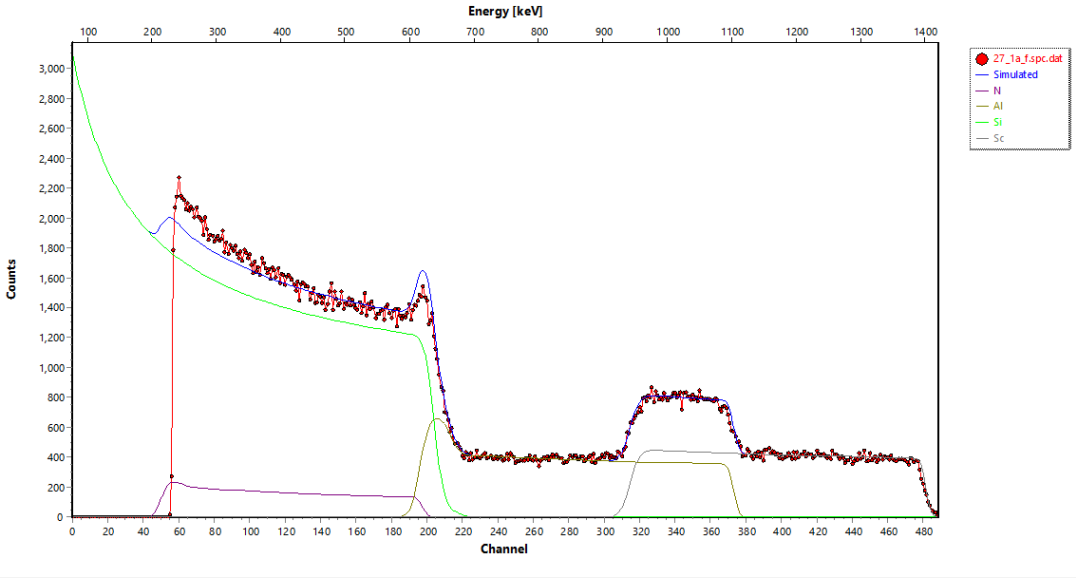

Figure 2.20. RBS spectrum fitting process using SIMNRA.

In this thesis, a study of the composition of $Al_{0.7}Sc_{0.3}N$ films was made using RBS techniques. The study was carried out taking samples from different positions of the sputtered films on full wafers following a radial distribution to study their homogeneity and depth profile. A first set of experiments was carried out using 4He+ ions at 2.3 MeV. The backscattered ions were measured using a solid-state surface barrier detector with a solid angle of 3.9 msr and a resolution of 20 keV. To study the possible distribution of adsorbed oxygen, a second set of experiments was performed varying the incident energy to 3.05 MeV, 3.1 MeV and 3.038 MeV. All the measurements were performed in a 5 MeV tandem accelerator at the CMAM, Universidad Autónoma de Madrid, and all the resultant spectra were fitted using SIMNRA software [35].

2.2.4. Atomic force microscopy

Atomic force microscopy (AFM) is a versatile technique based on short-range (few nm) interaction forces between two non-magnetic bodies. In AFM measurements, a small tip is attached at the end of a micro-cantilever to scan the sample. By means of Van der Waals force interaction between the tip and the sample, the micro-cantilever experiences a deflection that can be quantified. The most common case is to use a laser beam pointing to a photodetector to measure these deviations and be able to assess the topography of the sample. The AFM scans for this thesis were performed by a Molecular Imaging Pico-SPM atomic force microscope (see Figure 2.21) in contact mode and the results were analyzed using Gwyddion software [36].

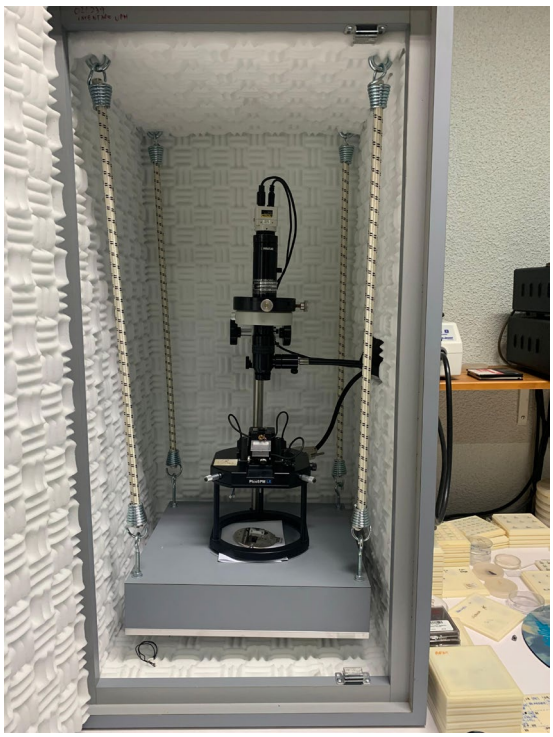

Figure 2.21. Molecular Imaging Pico-SPM 2100 AFM equipment.

Two main experiments were carried out using AFM measurements. The first one was regarding the $Al_{0.7}Sc_{0.3}N$ piezoelectric thin films to study their homogeneity in terms of topography, grain size and surface roughness, and the second one was to study low-power sputtered WO_3 layers to evaluate their surfaces in order to act as potential sensing layers in SMR-based high temperature sensors.

2.2.5. Scanning electron microscopy

Scanning electron microscopy (SEM) is a useful technique to analyze the morphology of micro and nanometric samples. To obtain these images, SEM microscopes use a small, focused and energetic electron beam on the sample. This beam is generated either by thermionic or field effect, and then is concentrated and focused on the sample using electromagnetic lenses. With the beam, it is possible to scan the sample and obtain different types of information depending on the beam-sample interaction detected. For morphology and surface studies, the most common interaction product used are the secondary electrons. As they are emitted from the sample, the electrons from the incident beam travel close to the nuclei of the atoms of the sample. The radiation liberated from this interaction can be absorbed by the electrons in the sample and overcoming the ionization potential of the atoms. These secondary electrons can be collected using a specific designed detector to which a positive voltage is applied. A typical SEM image using secondary electrons is depicted in Figure 2.22. To be able to operate, the whole setup needs to reach at least high vacuum conditions ($< 10^{-4}$ Pa) prior to the generation of the electron beam.

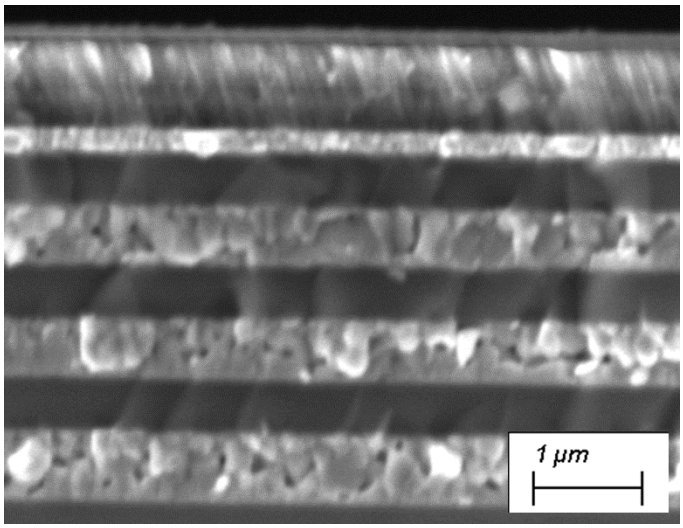

Figure 2.22. SEM micrograph of an AlN-based SMR.

Cross-section micrographs for the different devices manufactured for this thesis were obtained by SEM technique. The measurements were made using a ZEISS EVO 10 equipment (Figure 2.23), working with a W filament to generate the electron beam in the 3 to 7 kV range. These images were taken to investigate the morphology of the composing layers of the SMR devices and to ensure all the interfaces were clear and well defined.

Figure 2.23. Zeiss EVO 10 SEM equipment.

2.2.6. Electrical characterization

Once the resonators are manufactured, the electrical characterization step is crucial to know their suitability as transducers for sensor applications. It is important to know, among other things, their frequency response, their electromechanical coupling coefficients, or their Q factor values. The proposed method to assess these properties is by measuring the scattering parameters of the devices [37]:

$$S = \begin{bmatrix} S_{11} & S_{12} \\ S_{21} & S_{22} \end{bmatrix} \tag{2.2}$$

Where S_{11}, S_{22} are the reflection parameters and S_{12}, S_{21} are the transmission parameters. In our case, all the measurements were made by evaluating the S_{11} reflection parameter as a function of frequency. These measurements are achieved using an Agilent N5230A Vector Network Analyzer (VNA) connected to a GSG RF-probe for making electrical contact with the electrodes of the resonator. In our device configuration, the top electrode is in direct contact with the S tip of the RF-probe, whereas the bottom electrode is in contact with the G tips via capacitive coupling. A picture of the characterization setup is shown in Figure 2.24.

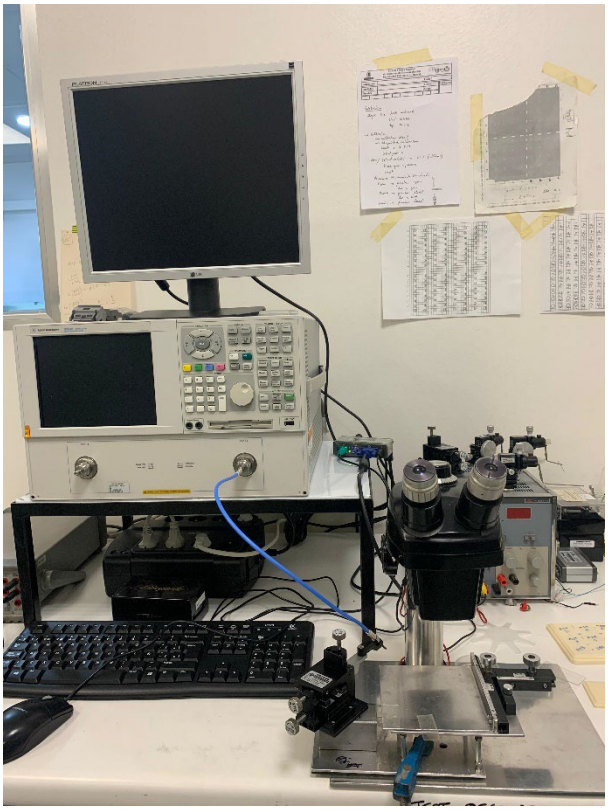

Figure 2.24. SMR characterization setup.

The whole setup is controlled by a LabVIEW application that gathers the S_{11} complex parameter from the VNA measurement and transforms it to impedance values:

$$Z_{11} = Z_0 \frac{1 + S_{11}}{1 - S_{11}} \tag{2.3}$$

Where $Z_0 = 50\ \Omega$ is the system characteristic impedance. A typical $\mathrm{Mod}(S_{11})$ plot can be observed in Figure 2.25(a), with its transformation to $\mathrm{Mod}(Z)$ values in Figure 2.25(b). The second representation is the preferred one for this work because it is visually more intuitive: the frequencies of resonance and anti-resonance can be easily recognized so a qualitative estimation of the behavior of the resonator can be achieved prior to further analysis.

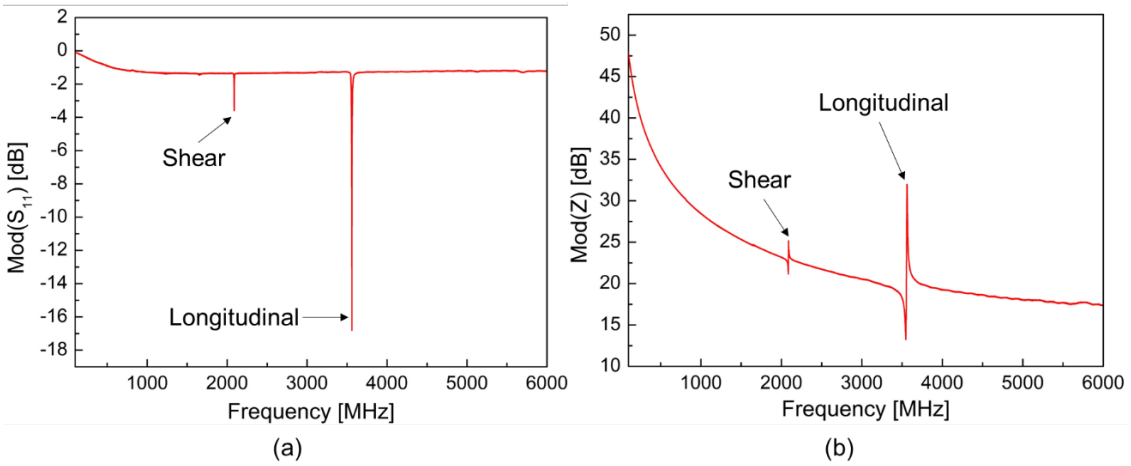

Figure 2.25. (a) Modulus of S_{11} parameter for an AlN-based SMR and (b) its modulus of Z representation. Shear and longitudinal modes are indicated in each figure.

Once the impedance and admittance ($Y = Z^{-1}$) data is obtained from the S_{11} measurement, the position of the resonant and anti-resonant frequencies is determined using the Re(Y) and Re(Z) curves, respectively. These curves are fitted using a standard least squares Levenberg-Marquadt algorithm, specifying the initial frequency range where the resonant (or anti-resonant) frequency should be and minimizing the residuals [38]. From this fitted curve, the position of the resonant (or anti-resonant) frequency can be extracted, as it can be observed from Figure 2.26(a) and Figure 2.26(b). The R_s and L_s parameters represent the electrical resistance coming from the electrodes and the inductance generated by electrode distribution, respectively. These parameters come from the modified Butterworth-Van Dyke's model (mBVD) [39] and have a significant influence on the shape of the peak, but not in the position. Thus, they are introduced to improve the fitting.

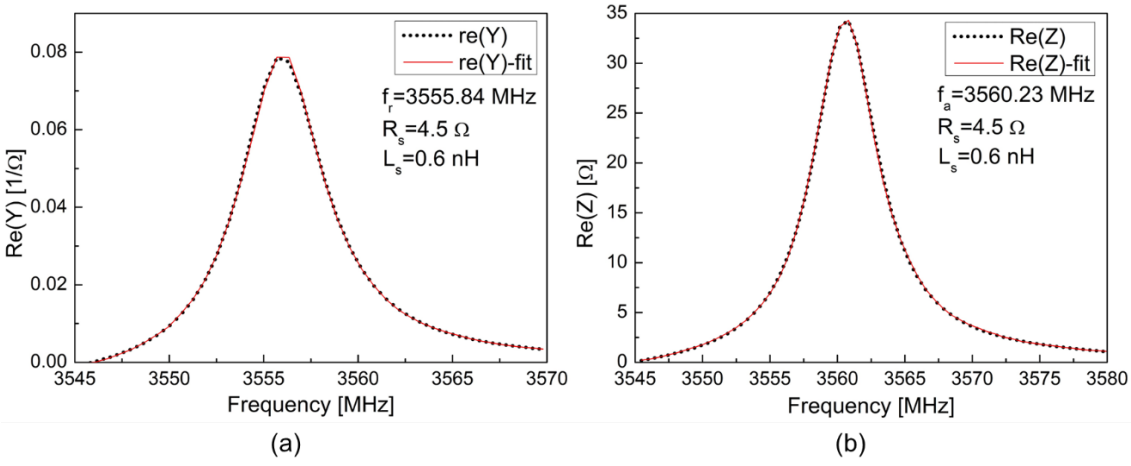

Figure 2.26. (a) Re(Y) at resonant frequency and least squares fitting, and (b) Re(Z) at anti-resonant frequency and least squares fitting.

With the values of f_r and f_a it is possible to extract the rest of the most important parameters to evaluate the behavior of the resonator, being k^2_{eff}, Q_r and Q_a the most important ones for the applications proposed in this work. These parameters are calculated with eqs. 1.17 and 1.20.

2.3. GAS SENSING SETUP: DESIGN AND MANUFACTURE

To evaluate the performance of the manufactured SMR-based sensors during this thesis, a specific characterization setup was designed and built. This setup is in fact part of one of the proposed objectives in section 1.3. For its design, the ambient conditions that needed to be generated to carry out the characterization of the sensing performance of the devices were carefully considered. These considerations could be summed up in the following points:

- A gas injection and exhaust system to generate controlled atmospheres with the possibility of tuning the concentration of the target gas.
- Operation in controlled high and low temperature regimes.
- Humidity generation.
- In-situ characterization of the sensor performance with VNA.

The final setup built during this thesis can be seen in Figure 2.27. It consists of two separate chambers, one for low temperature gas sensing characterization and one for high temperature gas sensing characterization, connected to a gas injection system and humidity generator. The chambers are also connected to a rotatory pump to generate a pre-vacuum prior to gas injection and to exhaust lines. The overall system is controlled with a homemade dashboard, that also allows to generate tunable gas mixtures giving instructions to the mass flow controllers (MFC) placed in each gas line. The chambers also have SMA connectors that allow in-situ characterization, performed with a Keysight P9371A Streamline portable VNA connected via RF-cable.

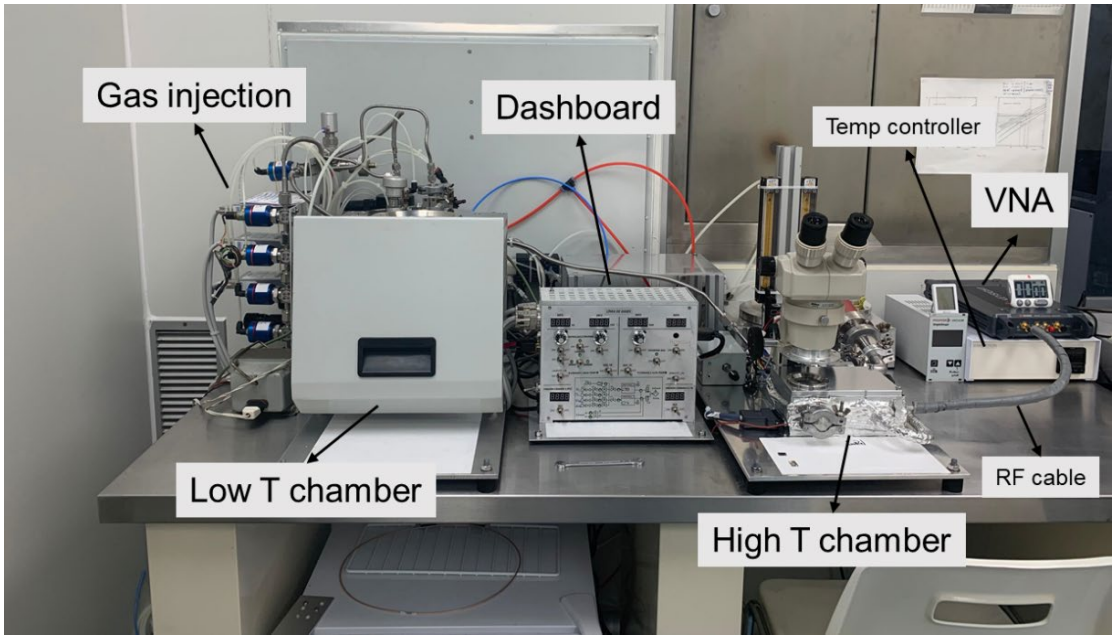

Figure 2.27. Gas sensing characterization setup.

The characterization setup can be broken down into three main elements: the gas injection system, the low temperature chamber and the high temperature chamber. As already mentioned, the main goal of the gas injection system is to create controlled atmospheres inside the chambers and to be able to tune the concentration of the target analyte. With the current setup, it is possible to create tunable CO_2 and NO atmospheres using dry air as a carrier gas, although it is possible to replace these gases for future investigations. In Figure 2.28, a diagram of the design of the whole gas injection system is shown. The necessary valves and MFCs to control all the gas lines are specified, together with the vacuum and exhaust systems for each chamber, provided also with Pirani pressure gauges, P1 and P2. Valves V1 to V9 are pneumatically actuated solenoid valves and MFC1, MFC2 and MFC3 are calibrated MFCs from Brooks Instrument with a 0-1000 sccm range of operation and an inlet pressure range of 0-10 bar.

Five main gas lines are part of the injection system. Three of them share the dry air bottle as point of origin: the vent line controlled by V1, the dry air line controlled by V2 and MFC1, and the humidity generation line (RH in Figure 2.28) controlled by V5. To generate humidity concentrations inside the chambers, a regulated dry air flow acting as carrier gas passes through a bottle filled with deionized (DI) water which is then directed to the characterization chamber. This method also offers the possibility of VOC atmosphere generation if DI water is replaced with a dissolution containing the target VOC.

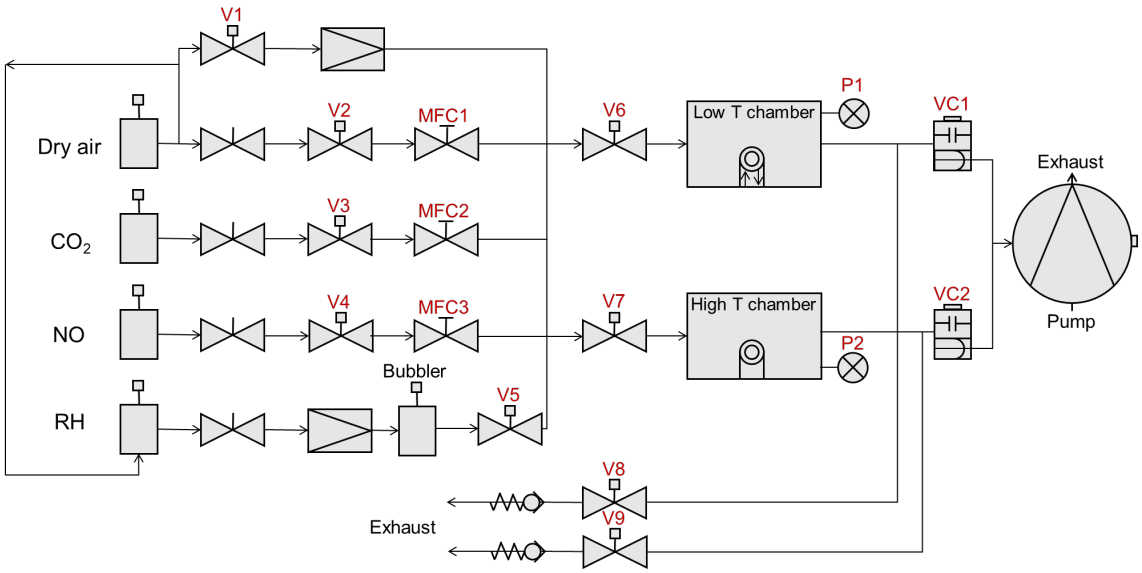

Figure 2.28. Gas injection system design.

The access of the gases to each chamber is regulated by V6 and V7. Prior to gas injection, the active chamber is pumped down to rough vacuum conditions by opening either VC1 or VC2 (pneumatically actuated vacuum valves), which are connected to a rotatory pump. This process is necessary and fast for cleaning the chamber from unwanted species and to create a vacuum seal to prevent leakages to the exterior. The exhaust lines are regulated by V8 and V9, which are connected to check valves to ensure unidirectional gas flow.

The inside of the low temperature chamber can be observed in Figure 2.29. The low temperatures are achieved using a Peltier module controlled by a current module and NTC sensor. The chamber is also refrigerated with coolant liquid using a fluidic system pumped by a water pump. The coolant liquid is stored in a freezer to ensure below 0°C operation. This fluidic system helps to dissipated power from the hot side of the Peltier module, so the temperature in the chamber can reach −50 °C. The chamber is also equipped with a humidity and temperature sensor from Bosch (BME680). To perform sensor characterization in this chamber, SMR-based sensors need to be first wire-bonded to a PCB with SMA connections as RF tip-based measurements are not possible due to lack of space.

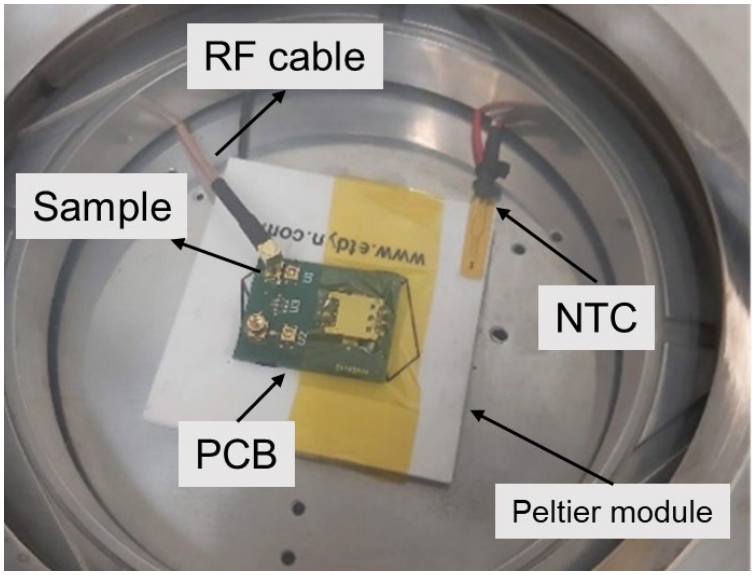

Figure 2.29. Low temperature chamber.

High temperature chamber, the inside of which can be observed in Figure 2.30, was acquired from NEXTRON based on an ad hoc design. It includes a heater module controlled by PID and thermocouple sensor adapted for in air and vacuum operation up to 450°C. The chamber also permits in situ characterization using RF tip contact on sample, which can be handled using a micropositioner. The tip and RF cable are connected to a portable VNA using the SMA connector installed on one of the chamber walls. Temperature and humidity conditions can also be monitored inside the chamber with a Bosch BME680 sensor.

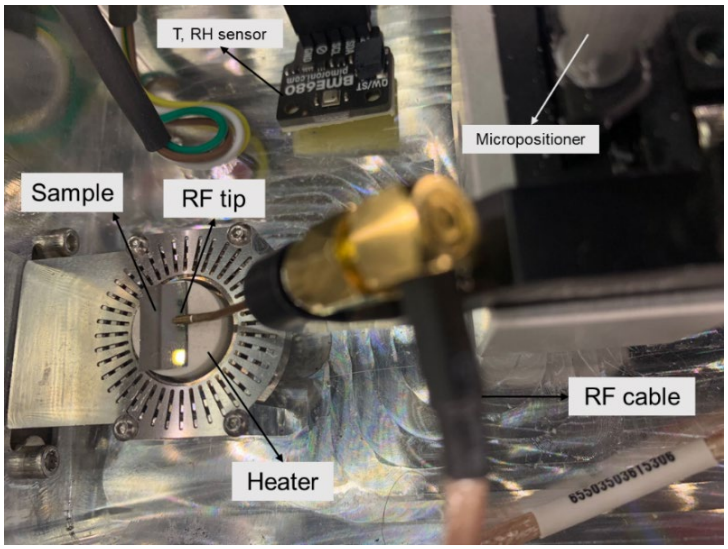

Figure 2.30. High temperature chamber.

Data acquisition from gas sensing characterization experiments was carried out using specifically designed LabVIEW applications. The software was built for tracking the position of resonant and anti-resonant frequencies in real time, together with the temperature and humidity data from the BME680 sensor, during the course of the experiments. In each measurement, before starting the real time tracking, the position of the frequencies had to be determined by fitting Re(*Y*) and Re(Z) as already explained in section 2.2.6. A snapshot of the process is shown in Figure 2.31(a). Once a satisfactory fitting is achieved, the real time monitorization of the frequency can start. A typical sensing characterization measurement is depicted in Figure 2.31 (b).

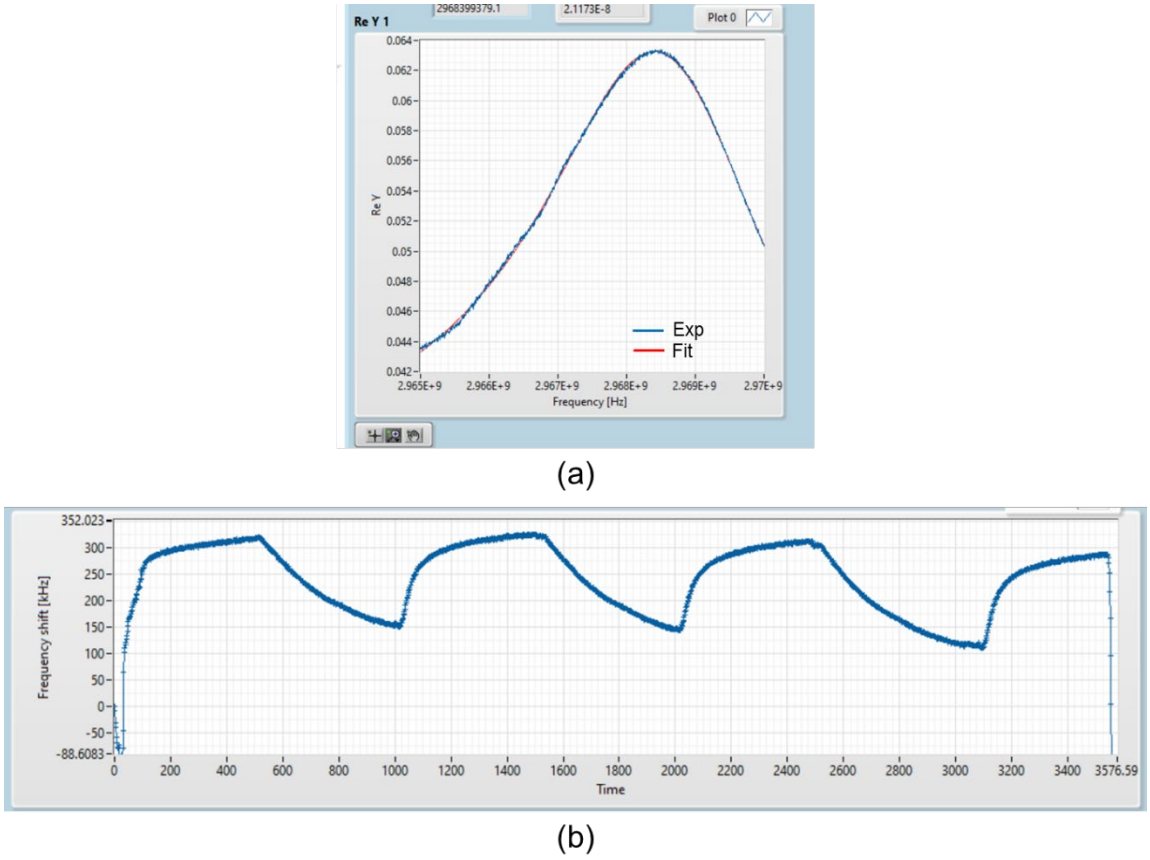

Figure 2.31. (a) Resonant frequency fitting and (b) real time resonant frequency monitorization.

References

[1] H. Adachi, T. Hata, T. Matsushima, T. Motohiro, and K. Tominaga, *Handbook of Sputter Deposition Technology*. Elsevier, 2012.

[2] W. D. Sproul, D. J. Christie, and D. C. Carter, "Control of reactive sputtering processes," *Thin Solid Films*, vol. 491, no. 1–2, pp. 1–17, Nov. 2005, doi: 10.1016/J.TSF.2005.05.022.

[3] L. B. Jonsson, T. Nyberg, I. Katardjiev, and S. Berg, "Frequency response in pulsed DC reactive sputtering processes," *Thin Solid Films*, vol. 365, no. 1, pp. 43–48, Apr. 2000, doi: 10.1016/S0040-6090(99)01116-5.

[4] K. Kano, K. Arakawa, Y. Takeuchi, M. Akiyama, N. Ueno, and N. Kawahara, "Temperature dependence of piezoelectric properties of sputtered AlN on silicon substrate," *Sens. Actuators A Phys.*, vol. 130–131, no. SPEC. ISS., pp. 397–402, 2006, doi: 10.1016/j.sna.2005.12.047.

[5] C. Bittencourt *et al.*, "Effects of Oxygen Partial Pressure and Annealing Temperature on the Formation of Sputtered Tungsten Oxide Films," *J. Electrochem. Soc.*, vol. 149, no. 3, p. H81, 2002, doi: 10.1149/1.1448821.

[6] A. Rydosz, K. Dyndał, W. Andrysiewicz, D. Grochala, and K. Marszałek, "GLAD Magnetron Sputtered Ultra-Thin Copper Oxide Films for Gas-Sensing Application," *Coatings*, vol. 10, no. 4, p. 378, Apr. 2020, doi: 10.3390/COATINGS10040378.

[7] PQL Designs, "PQL Designs. Sputtering systems." Accessed: Nov. 20, 2023. [Online]. Available: https://www.pqldesigns.co.uk/sputter-deposition-systems

[8] D. M. Mattox, *Handbook of Physical Vapor Deposition (PVD) Processing Second edition*, Second. Elsevier, 2010. doi: https://doi.org/10.1016/C2009-0-18800-1.

[9] B. Liu, G. Z. Xie, X. S. Du, X. Li, and P. Sun, "Pentacene based organic thin-film transistor as gas sensor," in *2009 Intern. Conf. on Apperceiving Computing and Intelligence Analysis, ICACIA 2009*, 2009, pp. 1–4. doi: 10.1109/ICACIA.2009.5361165.

[10] P. M. Martin, *Handbook of Deposition Technologies for Films and Coatings*, Third. Elsevier, 2010. [Online]. Available: http://elsevier.com/locate/permissions,

[11] M. F. Bhopal *et al.*, "High-κ dielectric oxide as an interfacial layer with enhanced photo-generation for Gr/Si solar cells," *Carbon N Y*, vol. 125, pp. 56–62, Dec. 2017, doi: 10.1016/j.carbon.2017.09.038.

[12] R. S. Feigelson, "Epitaxial growth of lithium niobate thin films by the solid source MOCVD method," *J. Crystal Growth*, vol. 166, 1-4, pp. 1-16, 1996, doi: 10.1016/0022-0248(95)00570-6.

[13] B. Bouchikhi *et al.*, "Formaldehyde detection with chemical gas sensors based on WO_3 nanowires decorated with metal nanoparticles under dark conditions and UV light irradiation," *Sens. Actuators B Chem.*, vol. 320, 128331, Oct. 2020, doi: 10.1016/j.snb.2020.128331.

[14] A. Firouzi, S. Sobri, F. M. Yasin, and F. Ahmadun, "Synthesis of Carbon Nanotubes by Chemical Vapor Deposition and their Application for CO_2 and CH_4 Detection," *Intern. Conf. on Nanotech. and Biosensors*, vol. 2, pp. 169–172, 2010, Accessed: Oct. 13, 2021. [Online]. Available: https://www.researchgate.net/publication/267967873

[15] S. Bhansali and A. Vasudev, Eds., *MEMS for Biomedical Applications*, First. Woodhead Publishing, 2012.

[16] A. A. Tseng, K. Chen, C. D. Chen, and K. J. Ma, "Electron beam lithography in nanoscale fabrication: Recent development," *IEEE Trans. on Electronics Packaging Manuf.*, vol. 26, no. 2, pp. 141–149, Apr. 2003, doi: 10.1109/TEPM.2003.817714.

[17] J. P. Silverman, "Challenges and progress in x-ray lithography," *J. of Vacuum Sci. & Tech. B: Microelectronics and Nanometer Structures Processing, Measurement, and Phenomena*, vol. 16, no. 6, pp. 3137–3141, Nov. 1998, doi: 10.1116/1.590452.

[18] F. Rahman, D. J. Carbaugh, J. T. Wright, P. Rajan, S. G. Pandya, and S. Kaya, "A review of polymethyl methacrylate (PMMA) as a versatile lithographic resist – With emphasis on UV exposure," *Microelectron. Eng.*, vol. 224, p. 111238, Mar. 2020, doi: 10.1016/J.MEE.2020.111238.

[19] I. G. Foulds, R. W. Johnstone, S. H. Tsang, M. Hamidi, and M. Parameswaran, "Polydimethylglutarimide (PMGI) as a structural material for surface micromachining," *J. of Micromech. and Microeng.*, vol. 18, no. 4, Apr. 2008, doi: 10.1088/0960-1317/18/4/045026.

[20] K. A. Jackson and W. (Wolfgang) Schröter, Eds., *Handbook of semiconductor technology*, First. Wiley-VCH, 2000.

[21] N. W. Ashcroft and N. D. Mermin, *Solid State Physics*, First. Philadelphia: Saunders College, 1976.

[22] P. M. Mayrhofer, C. Eisenmenger-Sittner, H. Euchner, A. Bittner, and U. Schmid, "Influence of c-axis orientation and scandium concentration on infrared active modes of magnetron sputtered ScxAl1-xN thin films," *Appl. Phys. Lett.*, vol. 103, no. 25, p. 251903, Dec. 2013, doi: 10.1063/1.4850735.

[23] M. Newville *et al.*, "LMFIT: Non-Linear Least-Square Minimization and Curve-Fitting for Python," *Zenodo*, 2014.

[24] S. Mertin *et al.*, "Piezoelectric and structural properties of c-axis textured aluminium scandium nitride thin films up to high scandium content," *Surf. Coat. Technol.*, vol. 343, pp. 2–6, Jun. 2018, doi: 10.1016/J.SURFCOAT.2018.01.046.

[25] C. K. Park, S. M. Chang, H. S. Uhm, S. H. Seo, and J. S. Park, "XPS and XRR studies on microstructures and interfaces of DLC films deposited by FCVA method," *Thin Solid Films*, vol. 420–421, pp. 235–240, Dec. 2002, doi: 10.1016/S0040-6090(02)00750-2.

[26] P. Zaumseil, "RCRefSim: Rocking Curve and Reflectivity Simulation." IHP Frankfurt, 2005.

[27] Y. S. Zou *et al.*, "Structural and optical properties of WO_3 films deposited by pulsed laser deposition," *J. Alloys Compd*, vol. 583, pp. 465–470, Jan. 2014, doi: 10.1016/J.JALLCOM.2013.08.166.

[28] S. Aftab, M. Z. Iqbal, S. Alam, and M. Alzaid, "Effect of an optimal oxide layer on the efficiency of graphene-silicon Schottky junction solar cell," *Int. J. Energy Res.*, vol. 45, no. 12, pp. 18173–18181, Oct. 2021, doi: 10.1002/er.6962.

[29] J. Olivares *et al.*, "Growth of carbon nanotube forests on metallic thin films," *Carbon N Y*, vol. 90, pp. 9–15, 2015, doi: 10.1016/j.carbon.2015.03.058.

[30] A. Girlando, M. Masino, A. Brillante, T. Toccoli, and S. Iannotta, "Raman Identification of Polymorphs in Pentacene Films," *Crystals*, vol. 6, no. 4, p. 41, Apr. 2016, doi: 10.3390/CRYST6040041.

[31] P. Eilers and H. Boelens, "Baseline Correction with Asymmetric Least Squares Smoothing," *Unpublished manuscript*, 2005.

[32] J. Perrière, “Rutherford backscattering spectrometry,” *Vacuum*, vol. 33, no. 5–6, pp. 429–432, 1987, doi: https://doi.org/10.1016/0042-207X(87)90327-7.

[33] C. Höglund, “Reactive magnetron sputter deposition and characterization of thin films from the Ti-Al-N and Sc-AI-N systems,” Ph.D. dissertation, Department of Physics, Chemistry, and Biology, Linköping University, 2008.

[34] U. K. Chaturvedi, U. Steiner, O. Zak, G. Krausch, G. Schatz, and J. Klein, “Structure at polymer interfaces determined by high-resolution nuclear reaction analysis,” *Appl. Phys. Lett.*, vol. 56, no. 13, pp. 1228–1230, Jun. 1990, doi: 10.1063/1.103332.

[35] M. Mayer, “SIMNRA User’s Guide, Report IPP 9/113,” Garching, Germany, 1997.

[36] D. Nečas and P. Klapetek, “Gwyddion: An open-source software for SPM data analysis,” *Central European J. of Phy.*, vol. 10, no. 1, pp. 181–188, Feb. 2012, doi: 10.2478/S11534-011-0096-2/METRICS.

[37] D. M. Pozar, *Microwave and Rf Design of Wireless Systems*, First. Wiley, 2000.

[38] J. J. Moré, “The Levenberg-Marquardt algorithm: Implementation and theory,” in *Numerical Analysis. Lecture Notes in Mathematics*, Berling, Heidelberg: Springer, 1978. doi: https://doi.org/10.1007/BFb0067700.

[39] J. D. Larson, P. D. Bradley, S. Wartenberg, and R. C. Ruby, “Modified Butterworth-Van Dyke circuit for FBAR resonators and automated measurement system,” *Proc. of the IEEE Ultrason. Symp.*, vol. 1, pp. 863–868, 2000, doi: 10.1109/ULTSYM.2000.922679.

3

SOLIDLY MOUNTED RESONATOR SENSORS: MATERIALS AND FABRICATION ROUTES

This chapter is centered in the study of the all the materials composing the manufactured devices for this thesis, from the piezoelectric active layer and its corresponding electrodes to the materials used in the layered acoustic reflector. Deposition parameters and essential properties for their role in the device (crystal structure, endurance to thermal processes, etc.) are discussed. Frequency response and resonator characteristics for the SMR configurations studied are also included.

The chapter starts with the design of the resonator using Mason's model simulations, followed by a description of the process to manufacture the SMR-based sensors. The characterization of the materials involved in each fabrication step is discussed afterwards. Then, the fabrication routes followed are included, specifying the differences between the chosen routes for the devices studied in next chapter. The functionalization processes to obtain the final sensing layers is covered in the last section, with a further discussion on the use of WO_3 thin films as NO sensing layers for high temperature operation and their integration on the fabrication route of the SMR-based sensors.

3.1. SMR DESIGN: MASON'S MODEL

Simulation methods are a powerful tool for the design and testing of devices that will be then fabricated and characterized in the laboratory. Regarding the design process of SMR devices, Mason's model is one of the most utilized simulation methods due to its simplicity and accuracy to represent device response [1].

The derivation of the model starts from eq. 1.2. Assuming a thin, large piezoelectric film between two planes z_1 and z_2, the electric field is described as follows [2]:

$$E = \frac{D - eS}{\epsilon} = \frac{1}{\epsilon}D - \frac{e}{\epsilon}\frac{\partial u}{\partial z} \tag{3.1}$$

The voltage can be obtained by integrating the electric field over the piezoelectric film:

$$V = \int_{z_1}^{z_2} E(z)dz = \frac{2dD}{\epsilon} - \frac{e}{\epsilon}[u(z_2) - u(z_1)] \tag{3.2}$$

where $2d = z_2 - z_1$ is the thickness of the film. Particle velocity (eq. 1.8) can be expressed as:

$$v = \frac{\partial u}{\partial t} = j\omega \tag{3.3}$$

Combining these two equations, the following expression for the voltage is obtained:

$$V = \frac{2d}{\epsilon}\frac{I}{j\omega A} + \frac{e}{j\omega\epsilon}[v(z_2) - v(z_1)] \tag{3.4}$$

where $I = j\omega A \cdot D$ was also introduced. From this expression it is possible to obtain the current:

$$I = j\omega C_0 V + \frac{eC_0}{\epsilon}[v(z_2) - v(z_1)] \tag{3.5}$$

where $C_0 = \epsilon A/2d$ is the capacitance. The displacement u(z, t) has the form of the solution of a classical wave equation:

$$u(z, t) = [a\sin(kz) + b\cos(kz)]e^{jwt} \tag{3.6}$$

For z_1 and z_2, the coefficients a and b have the form:

$$\begin{aligned} a &= \frac{1}{\sin 2kd}[u(z_2)\cos(kz_1) - u(z_1)\cos(kz_2)] \\ b &= \frac{1}{\sin(2kd)}[u(z_1)\sin(kz_2) - u(z_2)\cos(kz_1)] \end{aligned} \tag{3.7}$$

The mechanical force at the boundaries is given by:

$$F = -TA = -\left(cS - \frac{e}{\epsilon}D\right)A \tag{3.8}$$

where eq. 1.1 was used to substitute the stress T. The strain S can be expressed in terms of the displacement; therefore, it can be written in terms of coefficients a and b and introduced into eq. 3.8 to evaluate the boundary $z = z_1$:

$$F_1 = \frac{k \cdot c \cdot A}{\sin(2kd)}[u(z_2) - u(z_1)] - k \cdot c \cdot A \tan(kd) \cdot u(z_1) + \frac{e \cdot D}{\epsilon} \cdot A \tag{3.9}$$

The acoustic impedance can be written as $Z = k \cdot c/\omega$, and using this expression together with the ones for intensity and particle velocity, eq. 3.9 becomes:

$$F_1 = Z \cdot \frac{A}{j\sin(2kd)} \cdot [v(z_1) - v(z_2)] + jZ \cdot A \cdot \tan(kd) \cdot v(z_1) + \frac{e}{j\omega\epsilon} \cdot I \tag{3.10}$$

For the other established boundary, the expression is given by:

$$F_2 = Z \cdot \frac{A}{j\sin(2kd)} \cdot [v(z_1) - v(z_2)] + jZ \cdot A \cdot \tan(kd) \cdot v(z_2) + \frac{e}{j\omega\epsilon} \cdot I \tag{3.11}$$

These equations establish a connection between the acoustic and electrical variables. The equations give us a hint of what could be an equivalent circuit. A graphical representation of this circuit is given in Figure 3.1. In this circuit, the left and right ports are the acoustic ports, and the electrical port is the one helping with the piezoelectric coupling between acoustic and electrical variables.

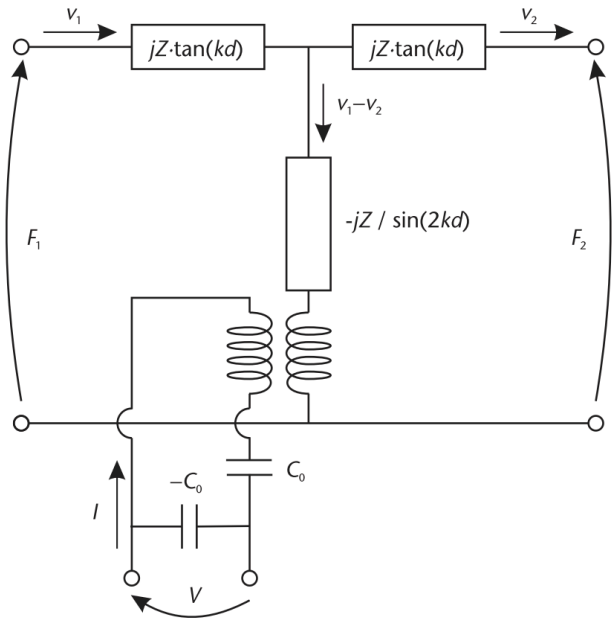

Figure 3.1. Mason model for a piezoelectric film [2].

For non-piezoelectric films, eqs. 3.10 and 3.11 are the same but removing the last term ($e \cdot I/j\omega\epsilon$), which is the only term in which the piezoelectric constant e appears. Thus, the equivalent circuit for a non-piezoelectric term is the same as the one represented in figure 3.1 with only the acoustic ports.

By cascading each transmission line, it is possible to combine multiple layers including piezoelectric and non-piezoelectric layers. Figure 3.2 shows a typical configuration for an SMR structure through their equivalent circuit representation. The top electrode is terminated by an acoustic short given by a stress-free surface and the final impedance at the right corresponds to the impedance of the substrate assuming it is a semi-infinite medium. The piezoelectric layer has the three-port configuration presented in Figure 3.1 and it is coupled with the electrodes. The layers between the bottom electrode and the last layer correspond to the acoustic mirror. This is not the only possible configuration allowed by Mason model, as, for instance, multiple electrical ports can be added by including additional piezoelectric layers, or by not assuming the substrate as a semi-infinite medium and terminating the right port with another acoustic short [2].

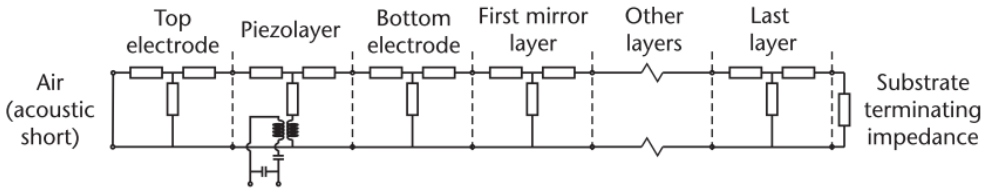

Figure 3.2. Equivalent circuit for an SMR structure with Mason model [2].

Each transmission line can be solved considering the analogy between voltage and mechanical force, and between current and acoustic displacement velocity. With this in mind, it is possible to use electrical network theory to perform the necessary calculations for the model [3], [4]. Thus, the acoustic part showed in Figure 3.1 can be considered a quadrupole with an ABCD matrix:

$$\begin{pmatrix} F_2 \\ v_2 \end{pmatrix} = \mathrm{ABCD} \begin{pmatrix} F_1 \\ v_1 \end{pmatrix}$$

$$\mathrm{ABCD} = \begin{pmatrix} \cos(kd) & -jZ\sin(kd) \\ -j\dfrac{1}{Z}\sin(kd) & \cos(kd) \end{pmatrix} \tag{3.12}$$

With this method, calculating the acoustic impedance of the stack presented in Figure 3.2 becomes simpler. For each interface, F and v can be calculated considering the properties of the involved materials and the final impedance of the

device can be obtained. By combining this expression with the ones already provided by the model, like eqs. 3.4 and 3.5, it is possible to derive the electrical impedance of the structure at the electrical port.

The electrical impedance of the resonator can be derived assuming time harmonic and quasi-electrostatic conditions [5]:

$$Z = \frac{1}{j\omega C_0}\left[1 - \frac{k_t^2 \tan\left(\frac{kd}{2}\right)}{\frac{kd}{2}} \cdot \frac{\left(\frac{Z_1 + Z_2}{Z_P}\right)\cos^2\left(\frac{kd}{2}\right) + j\sin(kd)}{\left(\frac{Z_1 + Z_2}{Z_P}\right)\cos(kd) + j\left(\frac{Z_1 Z_2}{Z_P^2} + 1\right)\sin(kd)}\right] \tag{3.13}$$

where, in this case, Z_1 and Z_2 are the acoustic impedances of the top and bottom electrodes, and Z_P the acoustic impedance of the piezoelectric layer.

Knowing the potential frequency response of the proposed resonator, it is important to design an appropriate acoustic reflector to minimize acoustic losses and help confine the maximum amount of energy within the resonator structure. The reflection coefficient at the interface between two layers with different acoustic impedances has the form [4], [6]:

$$\Gamma = \frac{Z_l - Z_0}{Z_l + Z_0} \tag{3.14}$$

where Z_0 is the impedance of the material from which the incident wave is travelling, and Z_l is the load impedance of the material beyond the interface. The transmission line equation for the overall input impedance from the two materials and their interface will be:

$$Z_{in} = Z_0\left[\frac{Z_l + jZ_0\tan\theta}{Z_0 + jZ_l\tan\theta}\right] \tag{3.15}$$

where Z_{in} is the input impedance and θ the total phase of the wave across the structure.

For an ideal SMR, the reflection coefficient at the interface between the resonator and the reflector should be as close to 1 as possible, meaning that all the generated acoustic waves would stay confined within the resonator structure. To achieve this, the acoustic reflector structure consists of alternating $\lambda/4$-thick low and high acoustic impedance layers to promote high reflection coefficients at each interface, as stated by eq. 3.14. The $\lambda/4$ thickness is related to the aimed frequency for optimal propagation, being $\lambda = v_{mat} \cdot f$ the wavelength of the desired propagation mode in each material. It is possible to calculate the total impedance at

the resonator-reflector interface using recursive relations between each layer, leading to the following expression:

$$Z_n = Z_{mat,n}\left[\frac{Z_{mat,n}}{Z_{n+1}}\right] \tag{3.16}$$

where $Z_{mat,n}$ is the material acoustic impedance in layer n. Adding more layers to the reflector usually leads to a higher overall coefficient. However, it leads to a more stressed structure. Therefore, we must try to reach the highest reflection coefficient possible without compromising the structure of the device or adding excessive fabrication steps.

To characterize the reflective power of an acoustic reflector, its logarithmic transmittance is used:

$$T_{dB} = 10\log(1 - |\Gamma|^2) \tag{3.17}$$

being Γ the reflection coefficient of the entire structure for a specific propagation mode.

For this thesis, several reflector configurations were tried, including fully dielectric configurations (AlN/SiO_2, ZnO/SiO_2, Ta_2O_5/SiO_2 and HfN/SiO_2) and semi-metallic configurations (Mo/SiO_2), as will be discussed in next section. Prior to their fabrication, the design process was carried out using the presented tools in this chapter. Mason's model combined with ABCD matrix calculation methods was previously implemented in a LabVIEW program, and the necessary simulations were performed. As an example of this process, Figure 3.3 shows the simulated response of an SMR designed to present a longitudinal mode at 3.0 GHz. The resonator consists of an 800 nm thick AlN film sandwiched between Ir and Mo layers, acting as bottom and top electrodes. The resonator structure lays on a 7 layer Mo/SiO_2 acoustic reflector, whose transmittance for shear and longitudinal modes are also represented in Figure 3.3. In this case, for the reflector to show optimal reflection coefficient at 3.0 GHz, the simulation tells us that the thickness of the Mo and SiO_2 must be 524 nm and 517 nm, respectively.

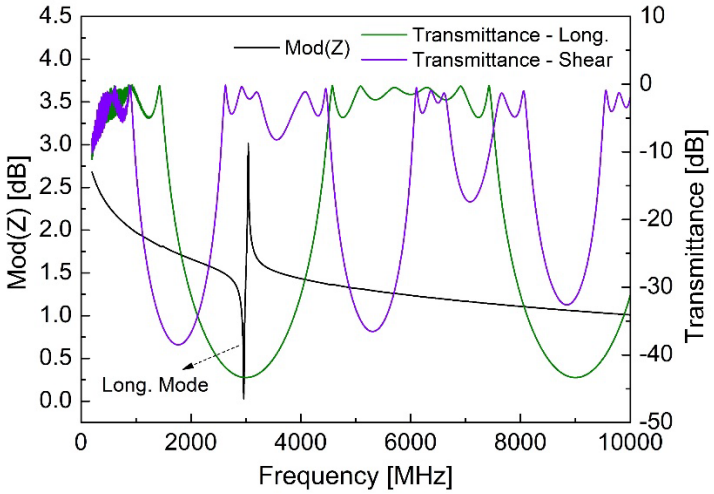

Figure 3.3. Simulated frequency response by Mason of an AlN-based SMR on a Mo/SiO_2 acoustic reflector. The simulated transmittance performance of the reflector for shear and longitudinal modes is also represented.

3.2. ACOUSTIC REFLECTORS

As already mentioned in Chapter 1, when manufacturing an SMR it is of great importance to have an acoustic reflector capable of offering good acoustic reflection in the frequency range of operation. Depending on the application, the choice of the materials composing the reflector is also important, since using the best combination in terms of performance is not always possible.

3.1.1. Fully dielectric acoustic reflectors

Conventional acoustic reflector designs include metallic layers, usually as high impedance materials. The reason behind this choice lies in the fact that metals like Mo [7], Ir [8] or W [9], [10] exhibit very high acoustic impedance owing to their high mass density, achieving a remarkable contrast with the typical values reported for SiO_2 [11], commonly used as low impedance material. Therefore, good acoustic isolation can be achieved while providing a robust and easy-to-manufacture structure to grow the piezoelectric resonator on. However, the presence of metallic layers can be challenging for certain applications, like biosensing or any type of sensing applications in liquid media that needs to separate electric pads from the active area. These layers can create appreciable parasitic effects as they lie under

the metallic pads, so undesired capacitive couplings can be generated [12]. To get rid of these undesired effects, extra microfabrication steps would be required.

Another alternative would be to design an acoustic reflector configuration with no metallic layers. Four different combinations using dielectric materials were assessed during this thesis: AlN/SiO_2, ZnO/SiO_2, Ta_2O_5/SiO_2 and HfN/SiO_2. The main goal of this study is to compare their performance between them in terms of acoustic insulation, especially after processes involving harsh environments, such as high temperature conditions. For this purpose, after studying the structural properties of the proposed materials, the fabricated AlN-based SMRs were subjected to high temperature treatments to study the potential degradation of their performance.

The studied acoustic reflectors consisted of a stack of seven alternating low acoustic impedance (SiO_2) and high acoustic impedance layers. Three of the reflectors were manufactured using reactive pulsed DC sputtering at our facilities. After optimization of sputtering conditions [13], the ones used for this experiment are gathered in Table 3.1. For each reflector configuration, the whole structure was deposited without breaking vacuum. The HfN-based reflector was manufactured using reactive RF sputtering at the Electrical Engineering Division facilities of the University of Cambridge. The chosen sputtering conditions for this reflector are gathered in Table 3.2 [14]. The reflectors were grown on 4-inch high resistivity Si wafers, and extra samples of each material were deposited on thermal oxidized Si substrates to assess their structural properties.

Table 3.1. Sputtering conditions for acoustic reflector layers.

Material	Power [W]	Ar [sccm]	N_2/O_2 [sccm]	Sput. Pressure [Pa]	Thickness [nm]
SiO_2	1200	4.2	25.0	0.25	516
AlN	1200	27.5	20.6	1.47	904
ZnO	600	15.5	25.5	0.33	506
Ta_2O_5	1000	4.1	25	0.59	410

Table 3.2. Sputtering conditions for HfN/SiO_2 acoustic reflector layers.

Material	Power (Plasma) [W]	Power (cathode) [W]	Ar [sccm]	N_2/O_2 [sccm]	Sput. Pressure [Pa]	Thickness [nm]
SiO_2	600	300	55.0	8.0	3.71	443
HfN	1000	800	30.0	56.0	3.80	386

The deposited films were assessed by XRD spectroscopy to explore their crystallinity. The resulting measurements were analyzed, and the most relevant peaks were fitted to pseudo-Voigt functions, as can be observed from Figure 3.4. The results from the fitting process are gathered in Table 3.3. The deposited AlN films (Figure 3.4 (a)) show a clear wurtzite structure, with a preferential c-axis orientation, hence the high intensity of the 002 reflection [15]. The same structure is observed in the ZnO films (Figure 3.4 (b)); however, the presence of the 101 reflection indicates that some of the grains are not c-axis oriented [16]. For Ta_2O_5 (Figure 3.4 (c)), the deposited films show an orthorhombic structure as the appearance of 111 and 201 reflections suggest [17]. HfN films (Figure 3.4 (d)) show a face-centered cubic structure, as the 111 reflections suggest, although the low intensity of the peak might indicate a poor crystalline structure [18]. The FWHM of the 111 peak is also greater than the FWHM values of the main peaks of the other measured materials, suggesting a smaller crystallite size that could grant these films a more amorphous structure.

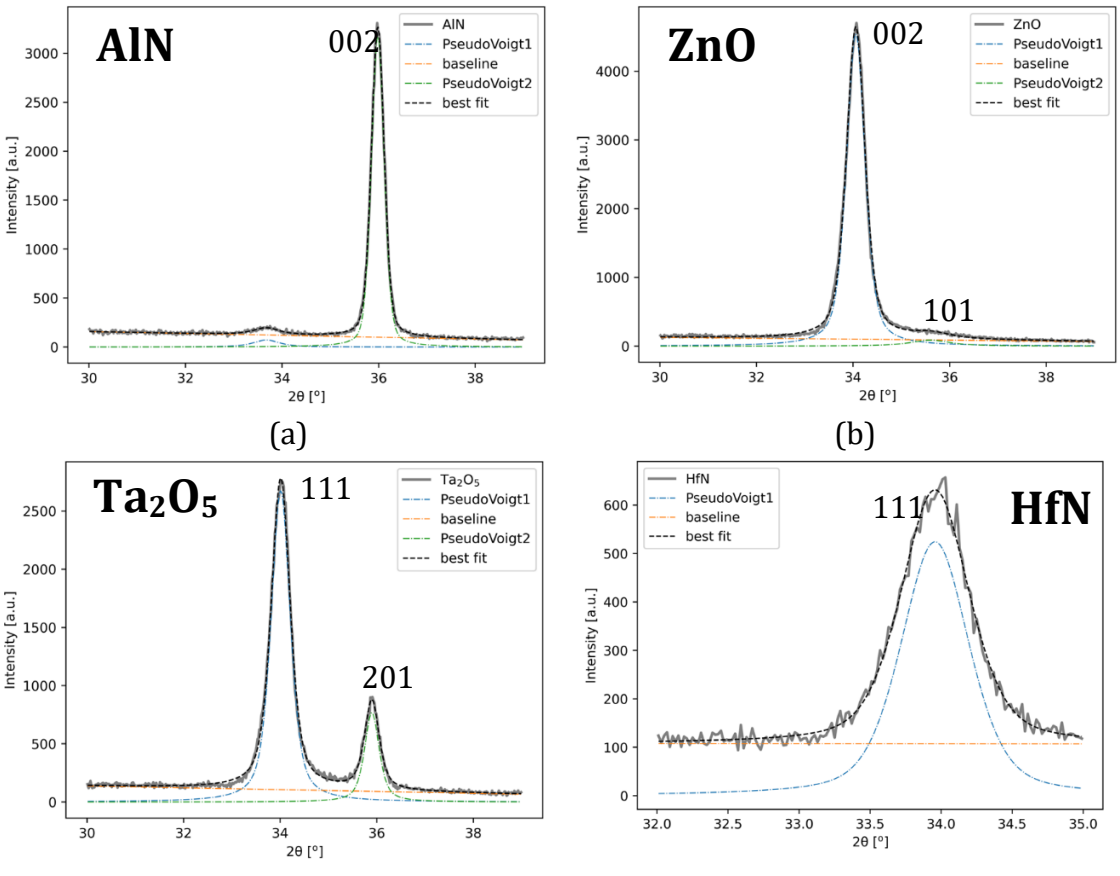

Figure 3.4. XRD $\theta - 2\theta$ patterns of the high impedance materials studied in this section: (a) AlN, (b) ZnO, (c) Ta_2O_5 and (d) HfN. The dashed lines correspond to the resulting functions of the fitting process.

Table 3.3. Positions and FWHMs of the XRD peaks according to the fittings.

Peak name	Position [°]	FWHM [°]
AlN (002)	35.98	0.31
ZnO (002)	34.06	0.46
ZnO (101)	35.60	1.00
Ta_2O_5 (111)	34.01	0.47
Ta_2O_5 (201)	35.90	0.36
HfN (111)	33.96	0.57

XRR spectroscopy measurements were also performed to the high acoustic impedance materials. By fitting the resultant curves, it is possible to estimate density, thickness, and roughness values. The most important region for the density estimation is angle at which the intensity starts to sharply decline. In Figure 3.5, the XRR curves for the studied materials are shown together with their fitted density values. The deposited films display lower densities than their nominal values except for ZnO, which presents the same density as its bulk value (5680 kg/m^3). For the AlN films, the fitted value corresponds to the 89% of its bulk value (3300 kg/m^3), whereas for Ta_2O_5 films, the fitted value corresponds to the 93% of the bulk density value 8200 kg/m^3. HfN films show the most remarkable change as the fitted density corresponds to the 80% of the bulk density value 13800 kg/m^3.

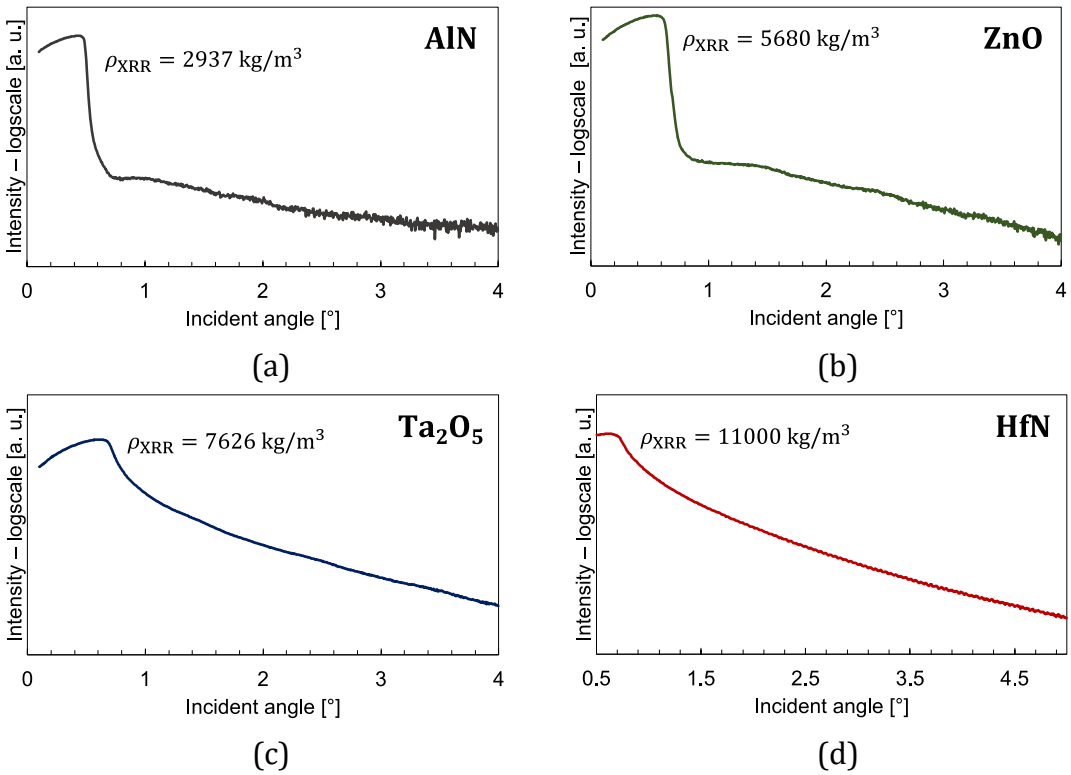

Figure 3.5. High acoustic impedance materials XRR curves: (a) AlN, (b) ZnO, (c) Ta_2O_5 and (d) HfN.

The acoustic impedance of any material for longitudinal and shear acoustic waves can be calculated with the following equation:

$$Z_{l,s} = v_{l,s}\rho \tag{3.18}$$

Where $v_{l,s}$ is the acoustic velocity in the material for longitudinal and shear waves, respectively, and ρ is the density. As already mentioned, the higher the acoustic impedance, the greater the mismatch with the low acoustic impedance material, SiO_2 in this case. This would ideally indicate that the acoustic reflector manufactured with the materials presenting the higher mismatch would provide the best acoustic isolation for an SMR. In Table 3.4, the calculated values for the shear and longitudinal acoustic impedances for the studied materials is shown. HfN presents the higher impedance values for both shear and longitudinal modes, whereas the other materials share quite similar results among them.

Table 3.4. Acoustic impedance calculations from XRR measurements [11], [14], [19]–[21].

Material	v_l [m/s]	v_s [m/s]	ρ_{XRR} [kg/m³]	Z_l [Mrayl]	Z_s [Mrayl]
AlN	10850	6170	2937	31.9	18.1
ZnO	6075	3680	5680	34.5	20.9
Ta_2O_5	4920	2900	7626	37.5	22.1
HfN	4950	4670	11000	54.5	51.4

Two types of AlN-based SMRs were manufactured for each reflector configuration: one with tilted AlN grains to display a shear mode and one with c-axis oriented AlN grains to display a high-quality longitudinal mode. The AlN films are sandwiched between an Ir bottom electrode and a patterned Mo top electrode, with a thin sputtered Ti film between the resonator and the reflector to improve adhesion. A SEM image of the cross-section of one of the devices can be observed in Figure 3.6. In particular, it is an AlN-based SMR on a ZnO/SiO_2 reflector. As it can be observed, the AlN film in this case presents tilted grains, which means that the frequency response of the device will display a shear mode.

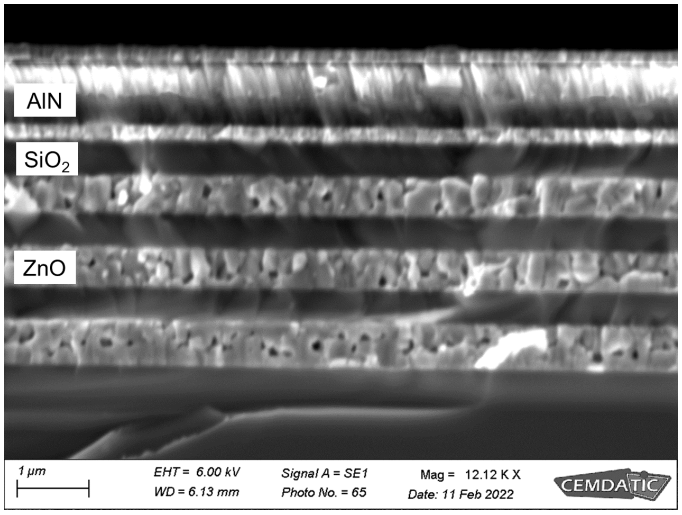

Figure 3.6. Cross-section of a shear mode AlN-based SMR on a ZnO/SiO_2 acoustic reflector.

After measuring their frequency response, the SMRs were exposed to a 700°C for 2 hours in vacuum. Then, their frequency response was again measured to observe the effects to high temperature exposure. The resonant and anti-resonant frequencies for the measured shear modes are in the $1.4 - 1.7$ GHz range and in the $2.7 - 3.0$ GHz range for the measured longitudinal mode devices.

The performance of the shear mode devices is summarized in Figure 3.7. For all the measured parameters, the presented value corresponds to the median of the distribution of measurements, with the error bars corresponding to the standard deviation of the distribution. In this way, it is possible to have a broader view of the performance of all resonators manufactured for each type of reflector. The k_{eff}^2 values remain almost unaltered (Figure 3.7 (a)), indicating that no degradation in piezoelectric properties of the AlN films occurs when the devices are exposed to 700°C environments. Regarding acoustic losses, both Q_r (Figure 3.7 (b)) and Q_a (Figure 3.7 (c)) share similar behavior. The measured values improve for AlN/SiO_2 and ZnO/SiO_2 reflectors and deteriorate for Ta_2O_5/SiO_2 and HfN/SiO_2 reflectors. Remarkable acoustic isolation levels are achieved for ZnO-based reflectors, with measured Q_r and Q_a values above 500, which indicates that this configuration could be the most appropriate for shear mode operation.

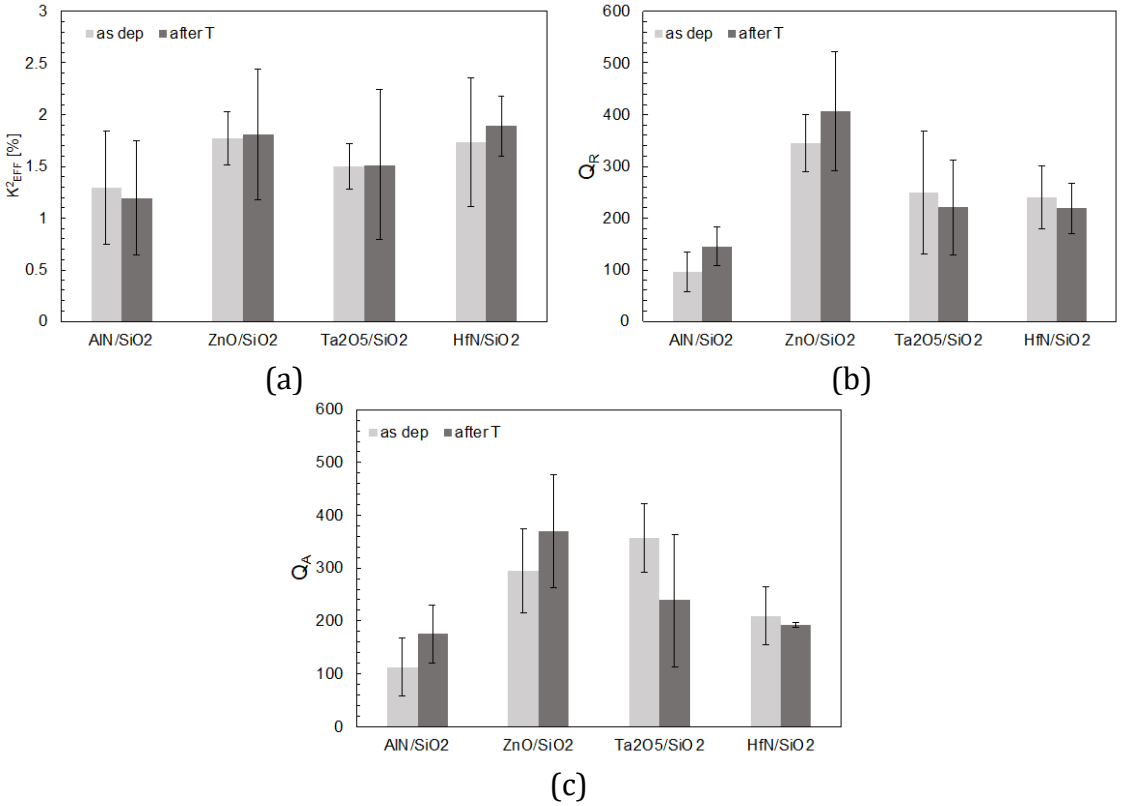

Figure 3.7. Shear mode measured performance for the shear mode SMRs: (a) k_{eff}^2, (b) Q_r and (c) Q_a before and after high temperature exposure.

The same study was carried out for longitudinal mode devices and the results are summarized in Figure 3.8. Similar to shear mode devices, Figure 3.8(a) shows the evolution of k_{eff}^2 values after high temperature exposure, and no appreciable changes are observed. Figure 3.8(b) shows Q_r values, suggesting that acoustic isolation deteriorates in three of the four reflector configurations, whereas Q_a values (Figure 3.8(c)) increase for AlN and ZnO-based reflectors and decreases for Ta_2O_5 and HfN-based reflectors. In this case, no reflector displays a significant better performance than the others, meaning that no configuration offers substantial advantages. However, HfN-based reflectors did in fact experience major degradation effects after high temperature exposition, as many of the manufactured resonators did no longer display a measurable resonance. In addition, the characterized devices showed considerably deteriorated resonances, as it can be observed from Figure 3.9(a) for longitudinal f_r and from Figure 3.9(b) for longitudinal f_a.

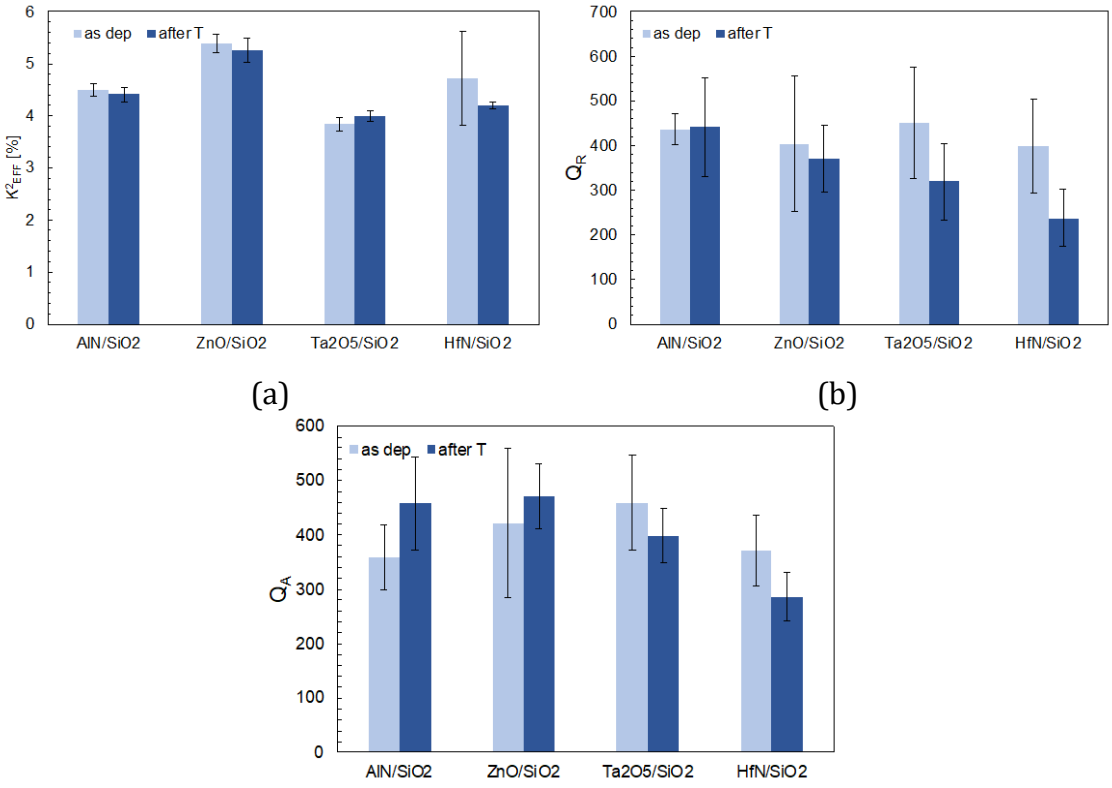

Figure 3.8. Shear mode measured performance for the longitudinal mode SMRs: (a) k^2_{eff}, (b) Q_r and (c) Q_a before and after high temperature exposure.

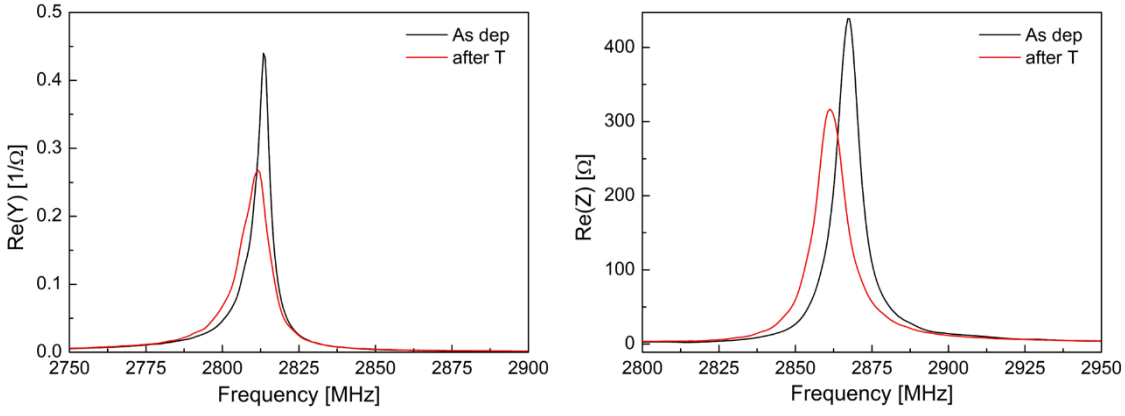

Figure 3.9. Frequency response before and after high temperature exposition for (a) resonant and (b) anti-resonant frequencies for resonators on HfN/SiO_2 reflectors.

To evaluate the behavior of the devices under temperature changes, TCF measurements were conducted for shear and longitudinal modes on all the four reflector configurations. Figure 3.10 shows the normalized resonant frequency shift for temperature changes between 15°C and 100°C, together with the linear

regression fit used to calculate the TCF for each acoustic reflector. All the obtained coefficients with their fitting error are gathered in Table 3.5. All the calculated TCFs are negative, meaning that increasing temperatures cause a shift to lower frequencies in all cases. The SMRs manufactured on AlN-based reflectors are the most unaffected by temperature changes, indicating that compensation techniques would require less effort for this configuration. Resonators on HfN-based reflectors are the ones displaying higher sensitivity to temperature changes for all the studied frequencies.

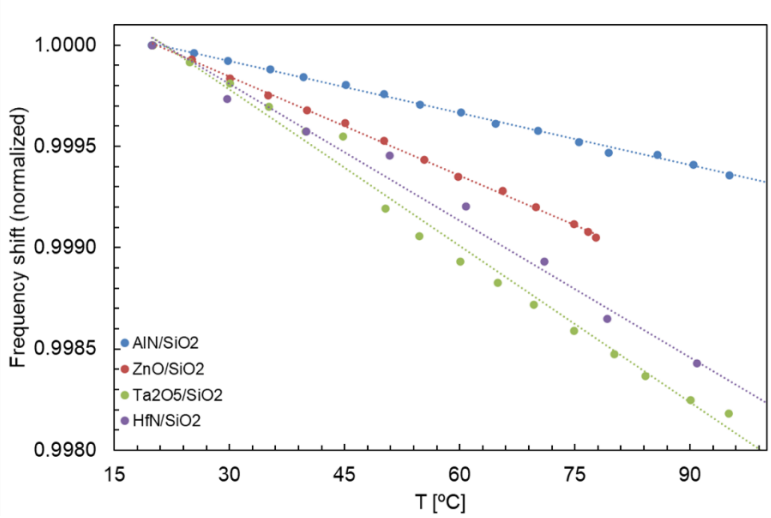

Figure 3.10. TCF measurements and linear fits for resonant frequencies of the longitudinal modes.

Table 3.5. Summary of TCF calculations in ppm · $°C^{-1}$.

Reflector	Shear TCF_r	Shear TCF_a	Long. TCF_r	Long. TCF_a
AlN/SiO_2	-14.33 ± 0.17	-14.84 ± 0.15	-8.55 ± 0.12	-8.82 ± 0.14
ZnO/SiO_2	-25.30 ± 0.80	-24.30 ± 0.30	-16.28 ± 0.15	-23.40 ± 0.80
Ta_2O_5/SiO_2	-33.30 ± 0.60	-25.20 ± 0.50	-25.70 ± 0.60	-23.50 ± 0.40
HfN/SiO_2	-36.00 ± 0.80	-28.30 ± 0.50	-31.60 ± 1.20	-34.90 ± 0.90

The comparative study revealed that the choice of one of these materials for high acoustic impedance layer in acoustic reflectors is subjected to the mode of operation and intended application of the SMR. For shear mode operation, ZnO/SiO_2 reflectors seem to be the ones providing better acoustic isolation, whereas for longitudinal mode operation Ta_2O_5/SiO_2 and AlN/SiO_2 can also be a good alternative. With no high temperature exposure, HfN/SiO_2 also offer comparable good acoustic isolation levels. To have a more detailed knowledge of the properties of these reflector configurations, more experimental actions would be required, such as measuring v_l and v_s values and performing in situ characterization of the

frequency response of SMRs based on each reflector at high temperature environments.

3.1.2. Mo/SiO_2 acoustic reflectors

Although dielectric reflectors are quite useful for certain applications, the most common reflector configuration is based on metals acting as high acoustic impedance layers. As already mentioned, Mo, Ir, W and Pt [22] are common choices for this role, as they present a high mismatch in acoustic impedance with SiO_2 layers. This provides the reflectors with usually higher acoustic isolation properties than the ones reported for reflectors with dielectric high acoustic impedance layers.

With a reported density of 10300 kg·m^{-3} and $v_l = 6190\ \mathrm{m \cdot s^{-1}}$, Mo has a longitudinal acoustic impedance of 63.8 MRayl [20]. For this thesis, Mo/SiO_2 acoustic reflectors were used for high temperature sensing applications, as their in-situ performance under high temperature operation was already assessed by the group [23]. In Figure 3.11, the frequency response of an SMR with Mo/SiO_2 acoustic reflector is presented. Almost no variation was observed for a seven-hour monitorization at 400 °C.

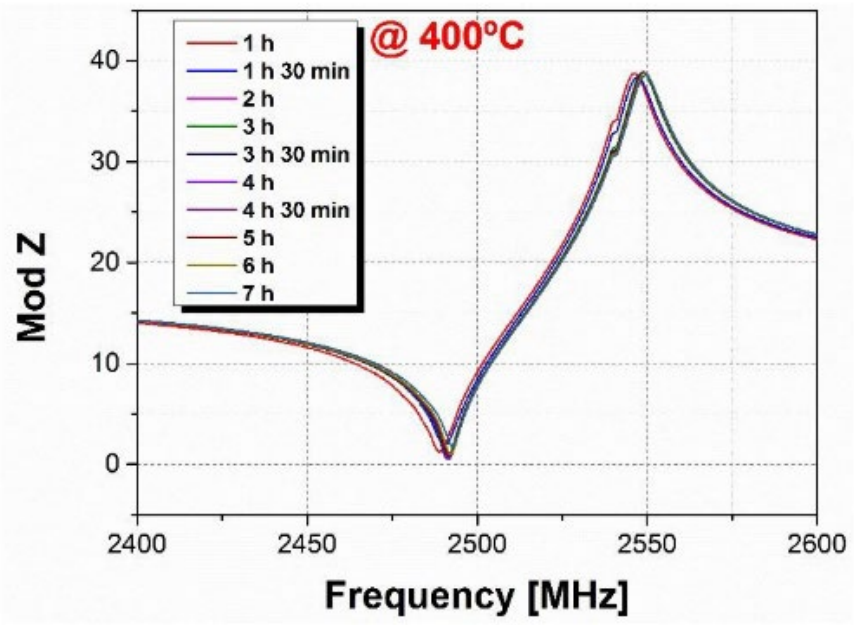

Figure 3.11. Frequency response of AlN-based SMR with Mo/SiO_2 reflector at 400 °C for seven hours [23].

The design of the fabricated reflectors is shown in Figure 3.12 and the selected sputtering conditions for each layer are gathered in Table 3.6. SiO_2 and Mo layers are deposited by pulsed DC magnetron sputtering from Si and Mo targets. For this type of reflectors, a thin Ti layer is also deposited between each SiO_2 and Mo layer to improve adhesion and prevent from delamination effects. These Ti layers were also deposited by pulsed DC magnetron sputtering from a Ti target. The whole resonator structure can be deposited using the same sputtering tool without breaking vacuum like the fully dielectric reflectors from previous section.

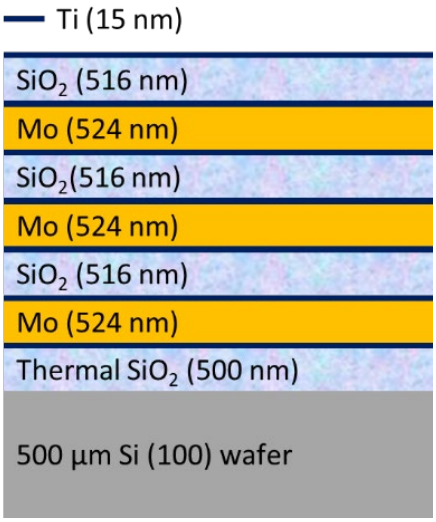

Figure 3.12. Design of Mo/SiO_2 acoustic reflector.

Table 3.6. Sputtering conditions for the acoustic reflector layers.

Material	Power [W]	Ar [sccm]	O_2 [sccm]	Sput. Pressure [Pa]	Thickness [nm]
SiO_2	1200	4.2	25.0	0.25	516
Mo	400	35.8	-	0.27	524
Ti	150	30.1	-	0.67	15

AlN-based SMRs were manufactured on Mo/SiO_2 reflectors. The resonators consisted of sputtered AlN piezoelectric films sandwiched between Ir and Mo layers as bottom and top electrodes, respectively. In Figure 3.13, the frequency response of a typical AlN-based SMR using Mo/SiO_2 acoustic reflector manufactured for this thesis is presented. Q values need to be sufficiently high for sensor applications because they usually decrease after functionalization processes, and some sensor properties are heavily dependent on them, such as the limit of detection.

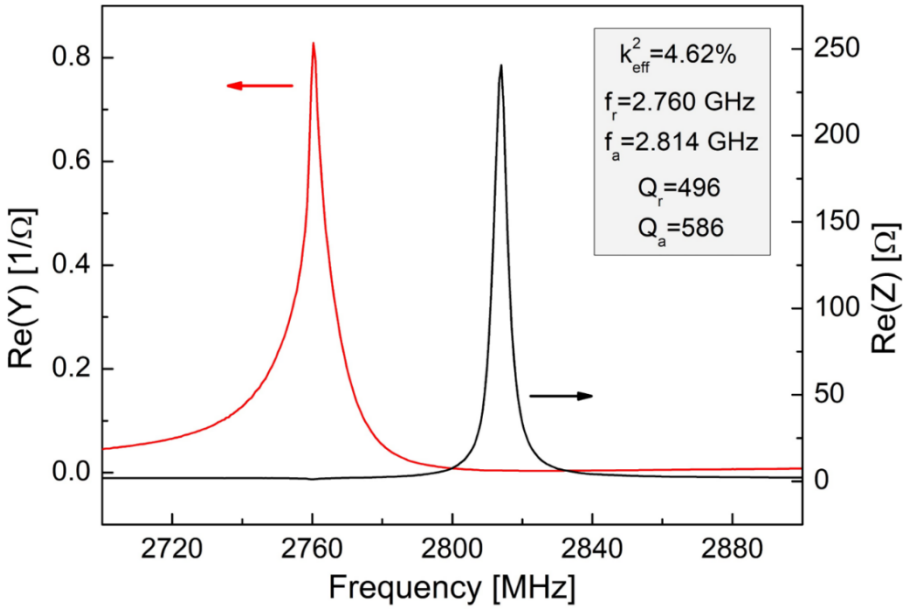

Figure 3.13. Typical resonant (red) and anti-resonant (black) frequencies for an AlN-based SMR on Mo/SiO_2 acoustic reflector.

3.3. ELECTRODES

An important part of the design of an SMR device is the choice of the pair of electrodes needed for the electrical excitation of the piezoelectric film. Al [24], [25], [26] and Mo [26]–[29] are the most common metals used as electrodes, although depending on the intended application and the rest of the materials used for the resonator, other metals such as Pt [30], Ir [23] and Au [10], [29] have been reported.

The manufactured SMRs for sensor applications during this thesis follow the same electrode configuration: Ir as bottom electrode and Mo as top electrode. For AlN-based SMRs, the choice of Ir bottom electrode was based on the proven good crystalline quality and good piezoelectric performance for sputtered AlN films on Ir substrates [31]. Thus, 120 nm thick Ir films were deposited on the acoustic reflectors via e-beam evaporation technique.

Patterned Mo films were used as top electrodes for all the SMRs in this thesis. Pulsed DC magnetron sputtering was the deposition method, and the topology was defined using UV-photolithography techniques and wet etching. The standard thickness for the deposited Mo electrodes was 150 nm. However, for high temperature applications, the thickness of the Mo electrodes was reduced to 120 nm and a very thin (30 nm) sputtered Au layer was deposited on top to prevent degradation related to oxidation processes. Final sputtering conditions for Mo and

Au layers are gathered in Table 3.7. In this case, the Mo/Au final electrode was defined by lift-off process. Figure 3.14 shows typical AlN-based SMR response with Mo top electrode before and after adding the protective Au layer. As would be expected, the extra Au layer causes a shift to lower frequencies. However, as the final Mo/Au electrode gets thicker, its series resistance decreases, which improves the Q factor at resonance.

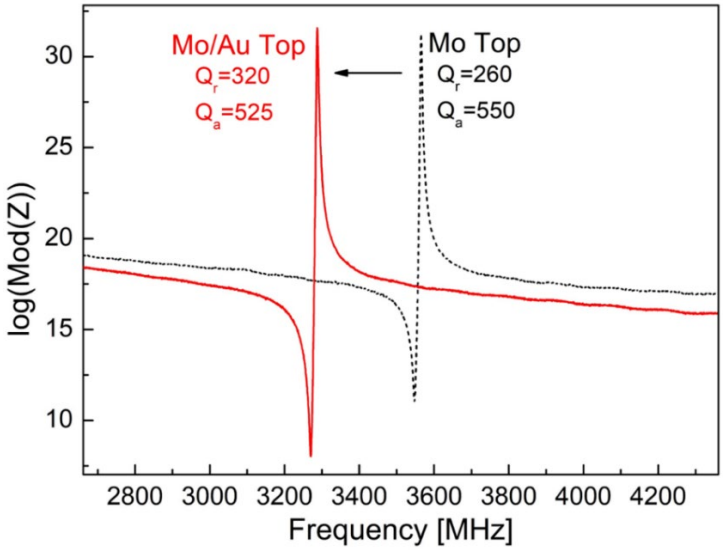

Figure 3.14. AlN-based SMR frequency response before and after adding a 30 nm thin Au layer to the top electrode.

Table 3.7. Sputtering conditions for top electrodes.

Material	Power [W]	Ar [sccm]	Sput. Pressure [Pa]	Thickness [nm]
Mo	400	18.1	0.20	150/120
Au	270	50.0	0.43	30

3.4. PIEZOELECTRIC MATERIALS

The most important part of any FBAR device is the piezoelectric film. Proper crystalline orientation and good electromechanical coupling are required to provide high quality resonances that can be exploited for the desired application. Specifically for sensor applications, frequency of operation and Q factors are the most important parameters to be considered, so high quality piezoelectric thin films need to be achieved.

In this thesis, two different piezoelectric materials were tested: AlN and $Al_{0.7}Sc_{0.3}N$. Piezoelectric AlN deposition technology is already mature and well

established within our research group, however, AlN-based resonators have reached certain performance limits that prevent them from meeting the specific requirements for some applications, especially related to 5G technologies. With this issue in mind, our group started to study AlScN-based resonators. In this section an extensive description of the properties of $Al_{0.7}Sc_{0.3}N$ thin films and SMRs, and their behavior with temperature is presented, discussing the potential use of these devices as transducers for sensor applications.

3.1.3. AlN

Piezoelectric AlN was deposited using MAREA, our in-house sputtering tool described in the previous chapter. Two deposition processes were employed, one for longitudinal mode devices and one for shear mode devices. Both processes start by placing the substrate in the transference chamber of the equipment and pumping it down to HV conditions using a turbomolecular pump. When vacuum conditions are achieved, the substrate is transferred to the deposition chamber, which is already under UHV conditions thanks to a cryogenic pump.

To improve crystalline quality, the deposition process of AlN is temperature assisted. For longitudinal mode devices, the substrate is heated up to 450°C and left in the deposition chamber to reach the desired vacuum conditions, typically below 10^{-5} Pa. To prepare the substrate for the sputtering process, the surface is first cleaned with Ar plasma generated by AC voltage using an RF power supply, with a process pressure of 1.33 Pa for three minutes. When the cleaning process is done, the sputtering process is then conducted, with the process conditions summarized in Table 3.8. It is worth noting that for the specified Ar and N_2 gas flow values, a gas mixture of 57.75:42.25 is set inside the deposition chamber. During the deposition process, an RF bias of -65 V is also introduced to force the c-axis orientation of the film.

Table 3.8. Piezoelectric AlN sputtering conditions.

Material	Power [W]	$T_{subs.}$ [°C]	Ar [sccm]	N_2 [sccm]	Sput. Pressure [Pa]
AlN	1200	450	27.8	38.0	0.16

For shear mode devices, AlN thin films presenting tilted grains were grown, following the studied recipe in [32]. First, an AlN seed layer of ~100 nm is deposited at room temperature following the sputtering conditions in Table 3.9. Then, the

piezoelectric AlN film is deposited under the conditions in Table 3.8. For this process, the substrates are placed at the edge of the substrate holder, which together with the seed layer promotes the growth of the piezoelectric film with its c-axis tilted with respect to surface normal [33].

Table 3.9. AlN seed layer sputtering conditions.

Material	Power [W]	$T_{subs.}$ [°C]	Ar [sccm]	N_2 [sccm]	Sput. Pressure [Pa]
AlN (seed)	600	RT	16.0	22.0	0.77

The AlN-based SMRs for sensor applications that will be discussed in next chapter were fabricated depositing piezoelectric AlN thin films following the process for highly c-axis oriented films. Tilted c-axis AlN films were deposited to fabricate the SMRs used to test fully dielectric acoustic reflectors under shear mode operation.

3.1.4. $Al_{0.7}Sc_{0.3}N$[1]

In the pursuit of finding materials with higher electromechanical couplings, new alternatives have emerged in the last decade to the well-established and mature piezoelectric materials, such as AlN and ZnO. New materials such as $LiNbO_3$ [34] and AlScN [35] have been subject of study over the last years as they can offer increased piezoelectric activity. In particular, $LiNbO_3$, despite offering large electromechanical coupling coefficients, seems not to be compatible with standard resonator technologies due to very complicated fabrication processes that require extremely high temperatures [36]–[38]. However, since the possibility of the incorporation of Sc atoms to the AlN structure was first reported by Akiyama [39], AlScN became a serious alternative to current piezoelectric materials as they can offer improved piezoelectric response. This material can be obtained by several thin film deposition methods, such as molecular beam epitaxy [40] and co-sputtering from separate Al and Sc targets [41]. For this study, the films were deposited via reactive magnetron sputtering of engineered targets to obtain AlScN with Al-Sc ratio of 70:30.

[1] This section is a partial reproduction of J. M. Carmona-Cejas, T. Mirea, J. Nieto, J. Olivares, V. Felmetsger and M. Clement, "Homogeneity and Thermal Stability of Sputtered Al0.7Sc0.3N Thin Films," *Materials*, vol. 16, no. 6, 2169, Mar. 2023, doi: 10.3390/ma16062169.

The films were deposited in an Endeavor-MX PVD cluster tool from OEM Group LLC. This equipment was provided with an S-gun magnetron with two independently controlled ring-shaped coaxial sputtering targets of 7 and 11 inches in diameter, engineered to have alternate Al and Sc segments. The design of the chamber and targets can be observed in Figure 3.15 (a) and (b). The size of the segments was set to achieve an Al-Sc ratio of 70:30. The target arrangement has been proven to provide stable and arc-free reactive sputtering of nitrides and oxides, in addition to the ability of reaching good compositional homogeneity in large regions. More detailed information about this can be found in [42]. Prior to deposition, the ring-shaped targets were preconditioned, first in metallic mode under an Ar atmosphere, and then in poisoned mode with an Ar-N_2 mixture. This last step prevented the films from being contaminated with Al_3-Sc precipitations. To ensure good film orientation and reduce roughness, a 50 nm AlN seed layer was first sputtered on all the utilized substrates. Then, without breaking vacuum, the AlScN films were deposited without intentional heating [43].

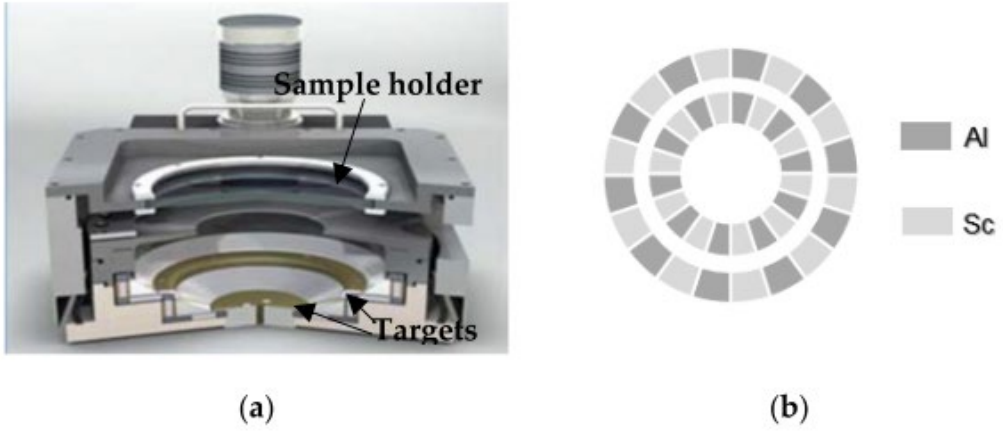

Figure 3.15. (a) Cross-sectional view of the sputtering chamber and (b) coaxial Al-Sc segmented targets.

Two types of substrates were employed for the study of AlScN films. To assess structural properties and composition, 720 nm thick AlScN films were deposited on 8-inch Si wafers coated first with the already mentioned 50 nm AlN seed layer (Figure 3.16(a)). 5 samples were taken from equidistant spots following wafer radius to evaluate uniformity in properties throughout the films. These samples were used to perform RBS+NRBS and XRD measurements, before and after applying a 600 °C thermal treatment in a vacuum for 1 h, as will be detailed below.

Extra samples with the same characteristics were also annealed at 700°C and used to obtain extra XRD measurements.

4-inch Si wafers (Figure 3.16(b)) were used to manufacture SMRs excited with the AlScN piezoelectric films. A 7 layer acoustic reflector was first fabricated on top of the Si substrate by alternating 620 nm thick SiO2 films to act as low acoustic impedance layers and 629 nm thick Mo films to act as high acoustic impedance layers. The piezoelectric sandwich manufactured on top of the reflectors consisted of a 110 nm thick Mo bottom electrode, the 50 nm AlN seed layer followed by the 1.1 µm AlScN piezoelectric film, and a 150 nm thick Mo top electrode, as shown in Figure 3.16(c). The Mo top electrode was finally patterned to excite the piezoelectric film via capacitive coupling. Figure 3.16(b) shows the wafer disposition within the sputtering chamber and the spots where the 5 samples were taken from to evaluate film uniformity in terms of piezoelectric properties, before and after applying 600°C annealing in a vacuum for 1 h. It is worth noting that these spots are practically the same as the ones chosen for the 8-inch wafers displayed in Figure 3.16(a), as this can leave the possibility of establishing correlations between the results obtained in all the characterization techniques applied in this study.

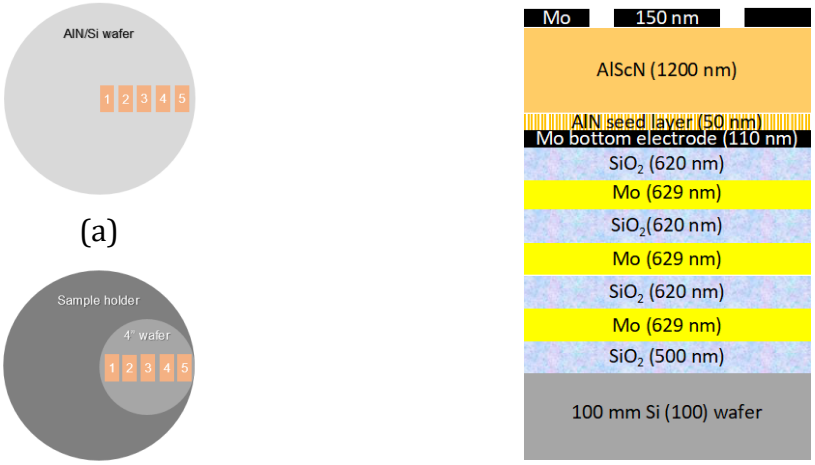

Figure 3.16. (a) Diagram of 8-inch AlN seed layer/Si wafer used as substrate. Numbers from 1 to 5 represent the spots where samples were taken from. (b) Diagram of the placement inside the sputtering chamber of the 4-inch wafer used to fabricate the SMRs and (c) their cross-section.

3.1.4.1. SMR Electrical response

Figure 3.17 shows an example of an impedance spectrum from two resonators: one located at the right edge of the 4" wafer, corresponding to the edge of sample holder, and another one located at the left edge of the 4" wafer, corresponding to the center of the sample holder. The c-axis favoring the growth of $Al_{0.7}Sc_{0.3}N$ films is evident after observing the longitudinal mode located at around 2 GHz. However, a shear mode is also observed at around 1.3 GHz, suggesting some dispersion in the microcrystal orientation along the c-axis, although this is not very significant since 10·1, 10·2 or 10·3 peaks are not observed in the XRD patterns, as discussed further in section 3.4.2.4. It is worth noting that the shear mode is excited in both samples, although generally, it appears to be of slightly higher intensity at the center of the wafer. This might be related to an increased deviation of the c-axis-oriented microcrystals, possibly related to the presence of some structural defects in this area.

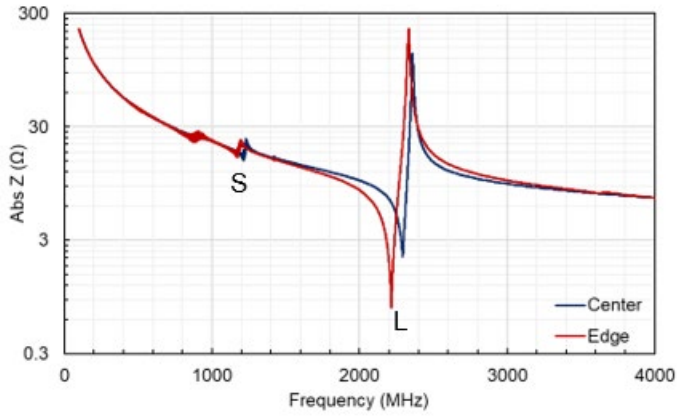

Figure 3.17. Frequency response of $Al_{0.7}Sc_{0.3}N$-based SMRs located at position corresponding to the sample holder center and located at sample holder edge. Shear and longitudinal modes are labeled with an S and L, respectively.

The electromechanical coupling factor (k_{eff}^2) of a series of SMRs was derived from the S_{11} measurements. This parameter can be used to estimate whether the $Al_{0.7}Sc_{0.3}N$ films display high quality in terms of their piezoelectric properties. Figure 3.18 shows the k_{eff}^2 radial distribution for different wafer spots before and after the thermal treatment. The k_{eff}^2 values appearing on the chart represent the mean value of the distribution of the resonators located in each position. The error bars attached to each point represent one standard deviation from each k_{eff}^2 distribution. As one

might observe, the k_{eff}^2 values increase as the distance from the center increases, revealing an improvement in the piezoelectric activity of the films. Despite this difference in electromechanical coupling, most of the resonators show a better k_{eff}^2 value than the usual ones obtained from AlN-based resonators, which usually range between 6% and 7% [44]–[46]. In this case, k_{eff}^2 values all range from 6% to 12%, with 12.8% being the highest measured value. A comparison between state-of-the-art values is shown in Table 3.10. After thermal treatment, resonators located near the central positions tend to improve their piezoelectric properties and their k_{eff}^2 coefficients increase to the 8–10% range. Regarding more external spots, the annealing seems to worsen the piezoelectric properties of this area, and thus their k_{eff}^2 became slightly worse, dropping to values above 10%.

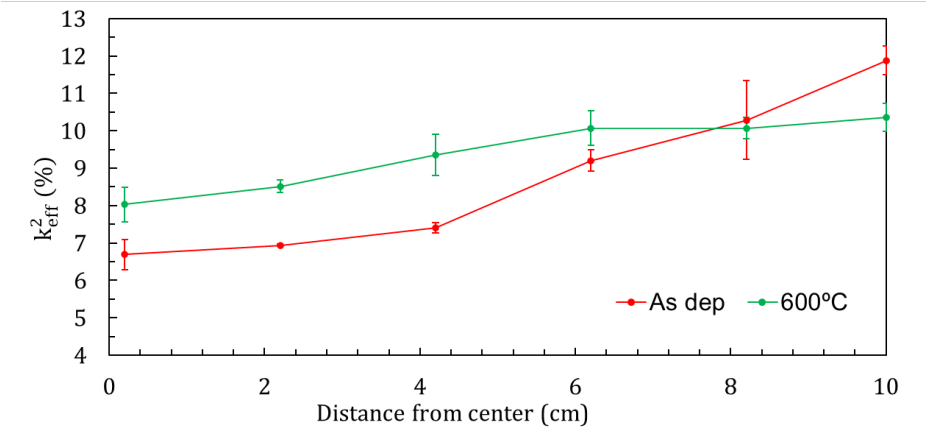

Figure 3.18. Radial distribution of mean k_{eff}^2 values for $Al_{0.7}Sc_{0.3}N$-based SMRs. The distance is measured from the sputtering chamber sample holder center. The error bars represent one standard deviation.

Table 3.10. k_{eff}^2 values of best and worst resonator presented in this work in comparison with state-of-the-art FBAR devices.

Piezoelectric Material	k_{eff}^2	Reference
AlN	6.5	[45]
$Al_{0.91}Sc_{0.9}N$	9.53	[35]
AlN/$Al_{0.87}Sc_{0.13}N$	10	[47]
$Al_{0.85}Sc_{0.15}N$	12	[35]
$Al_{0.8}Sc_{0.2}N$	14.5	[48]
$Al_{0.73}Sc_{0.27}N$	12.18	[49]
$Al_{0.7}Sc_{0.3}N$	6.3	This work (worst resonator)
$Al_{0.7}Sc_{0.3}N$	12.8	This work (best resonator)

In addition to these measurements, Table 3.11 shows the measured Q-factor distribution of the resonators located at the spots with lower (center) and higher (edges) electromechanical coupling factors. It is noticeable how they are quite similar to each other regardless of the wafer position for both resonant and anti-resonant frequencies. These values remain similar to each other after the annealing treatment, which might indicate that no extra acoustic losses are induced.

Table 3.11. Measured Q_r and Q_a distributions.

Distance from Center (cm)	$Q_r \pm \sigma$	$Q_a \pm \sigma$
10 (As dep)	210 ± 68	181 ± 38
10 (after 600 °C)	176 ± 78	200 ± 31
0.2 (As dep)	205 ± 107	194 ± 18
0.2 (after 600 °C)	166 ± 77	185 ± 40

3.1.4.2. SEM and AFM Characterization

Morphological characterization was carried out for the fabricated devices using SEM technique. The alternating Mo and SiO_2 layers showed distinct and clear interfaces. They also showed good thickness uniformity, the same as the two Mo electrodes that sandwiched the piezoelectric films. The $Al_{0.7}Sc_{0.3}N$ piezoelectric films are distinguishable from the AlN seed layers and display quite good uniformity in terms of thickness throughout the entire wafers. A typical micrograph of the cross section from a cleaved SMR sample can be seen in Figure 3.19.

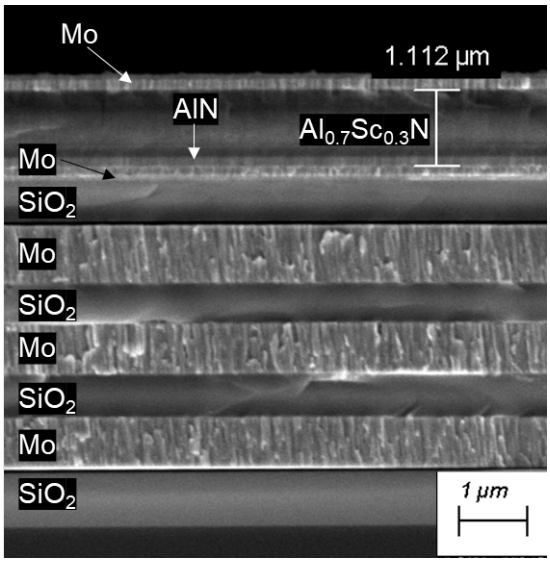

Figure 3.19. Cross-sectional SEM micrograph of the SMR stack.

The surface of the piezoelectric films was evaluated via AFM. Figure 3.20(a) shows a 1 × 1 μm topographic profile from the center of the wafer. A quite uniform and smooth surface can be observed, showing a root mean square roughness parameter of $R_{RMS} = 1.34$ nm. Figure 3.20(b) shows the same measurement from a spot near the edge of the wafer. In this case, the presence of abnormal grains is spotted, with sizes up to ~20 nm in height. However, the overall surface roughness improves, and calculating the R_{RMS} parameter from the regions with no abnormal grains, the results are lower ($R_{RMS} = 550$ pm).

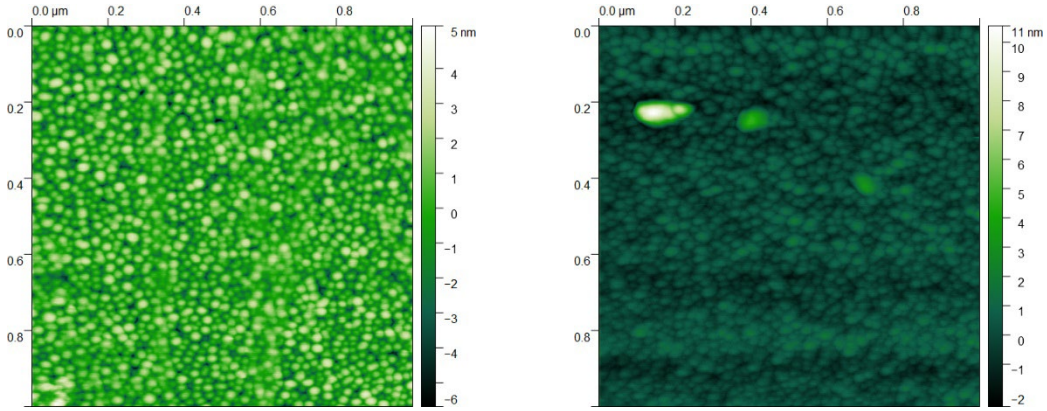

(a) (b)

Figure 3.20. (a) AFM topographic image of the center and (b) the edge of the $Al_{0.7}Sc_{0.3}N$ films deposited on 8-inch Si wafers.

3.1.4.3. Compositional study with RBS and NRA

RBS and NRA measurements were performed to the film deposited on Si substrates to investigate more about their composition. A first set of experiments [50] revealed that the thickness of the $Al_{0.7}Sc_{0.3}N$ film was uniform across the 8-inch wafer and that the Al-Sc ratio was relatively constant, going from 28.4% at the center to 30.6% at the edge of the wafer, as summarized in Table 3.12. However, this slight deviation seems not to be responsible for the observed variation in k^2_{eff} values observed for different film regions.

Table 3.12. Atomic composition at different wafer spots.

Distance from Center (cm)	Sc (%)	Al (%)	N (%)	$\frac{Sc}{Al+Sc}$ (%)
0–2 cm	14.3	36	49.7	28.4
2–4 cm	14.5	35.8	49.7	28.8
4–6 cm	14.2	35.2	50.3	28.7
6–8 cm	14.8	33.5	51.6	30.6
8–10 cm	15.2	34.5	50.2	30.6

To study the presence of light elements, a second set of experiments was performed at higher energies at which their scattering cross-section deviate from Rutherford cross-sections (non-Rutherford backscattering). The energies at which the process cross-section increases are called resonances [51]. First, we measured the NRBS spectra at 3.038 MeV, at which the scattering cross section of oxygen peaks is linked to the $^{16}O(\alpha, \alpha)^{16}O$ nuclear reaction. Figure 3.21(a) shows the NRBS spectra measured at 3.038 MeV on four different film spots, following a radial distribution. The almost identical patterns observed in the region between 1700 keV and 2250 keV (corresponding to the Sc signal) confirms the good homogeneity in terms of thickness of the $Al_{0.7}Sc_{0.3}N$ film [52]. The inset of Figure 3.21(a) outlines the signal peaks corresponding to oxygen located at the surface of the films. The measurement shows that the oxygen content clearly increases when moving from the edges to the center of the films, which might suggest that the central region of the wafer is more susceptible to adsorb oxygen atoms than the external region. This effect might be caused by a larger ion bombardment of this area of the sample holder during deposition, thus producing a more deteriorated surface with a higher concentration of structural defects, such as dangling bonds, which could end up in an increase in surface reactivity and the capturing of more oxygen atoms than other regions [53], [54].

To obtain more insight into the in-depth oxygen distribution along the $Al_{0.7}Sc_{0.3}N$ film, two other measurements were performed at higher energies (3.05 MeV and 3.1 MeV) to verify whether projectiles backscattered at 3.038 MeV with oxygen atoms could come from greater depths in the sample. As can be seen in the resulting spectra shown in Figure 3.21(b), no signal corresponding to backscattering with O atoms is observed for these energies, in contrast to what is observed at 3.038 MeV, suggesting that oxygen is only present at the surface of the film, as higher beam energies do not produce any peak related to the oxygen presence in the bulk of the material.

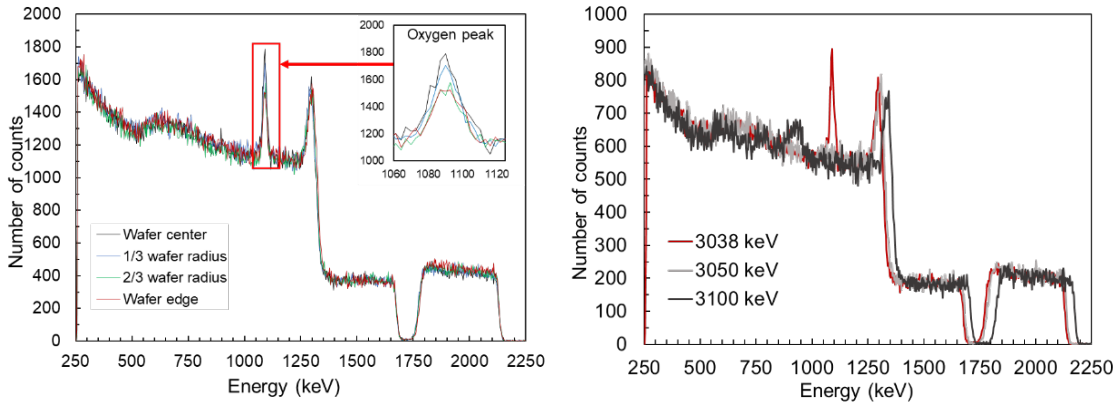

(a) (b)

Figure 3.21. (a) NRBS spectra taken at different wafer positions, fixing the beam energy at 3.038 MeV. The inset highlights the oxygen resonance detected when measuring at this energy [34]. (b) RBS-NRA spectra from wafer center taken at three different beam energies.

In addition to these measurements, other spectra were measured at 4.258 MeV, at which the scattering cross section of carbon (C) is maximized, owing to the $^{12}C(\alpha, \alpha)^{12}C$ nuclear reaction. These measurements did not reveal the presence of this impurity at the surface of the film.

3.1.4.4. Structural study: XRD Measurements

Crystalline structure of the $Al_{0.7}Sc_{0.3}N$ films on 8-inch Si wafers was assessed by XRD measurements. As can be observed in Figure 3.22, typical theta-2theta patterns only displayed the 00·2 (and 00·4) reflections corresponding to both $Al_{0.7}Sc_{0.3}N$ films and the AlN seed layer, with no evidence of misoriented grains, as 10·1, 10·2 and 10·3 peaks are not observed. Figure 3.22 also shows that the region gathering the most information about the structure of the films is located in the range between 34° and 37° in 2θ. Figure 8 shows this region in more detail, together with the resulting pseudo-Voigt functions used to perform the deconvolution of the main features for two samples located at the center (Figure 3.23(a)) and the edge (Figure 3.23(b)) of the wafer.

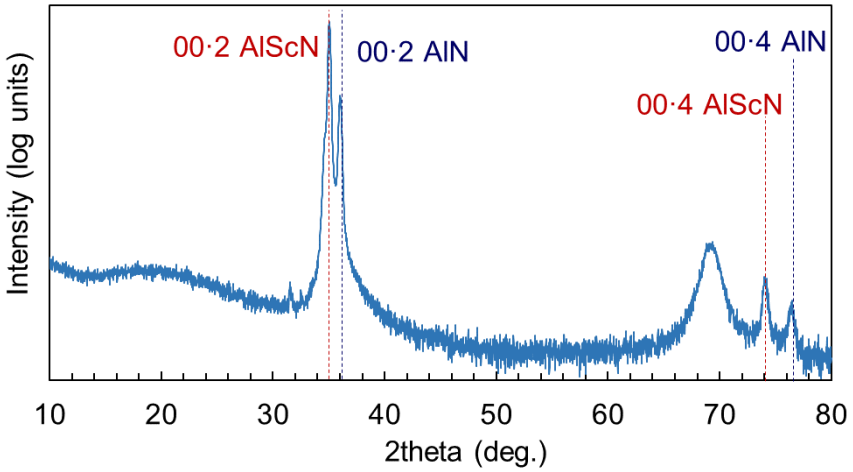

Figure 3.22. Typical XRD pattern of $Al_{0.7}Sc_{0.3}N$/AlN/Si structure. Y axis is in log units to highlight the absence of 10·1, 10·2 and 10·3 peaks.

The main features between 34° and 37° can be fitted by using three pseudo-Voight functions in the sample located at the center of the wafer, whereas only two functions are required to deconvolute the peaks at the edge of the wafer. The peak at around 36° present in the two samples is attributed to the 00·2 AlN peak of the seed layer. The main peak of the two spectra is associated with the reflection with the 00·2 planes of the $Al_{0.7}Sc_{0.3}N$ film; the fact that the peak experiences a significant shift between samples could be related to differences in planar stress, since RBS measurements allows us to rule out peak shifts due to compositional changes. An extra peak at ~34.5° is required to fit the features at the central area of the wafer, which could be attributed to the non-piezoelectric 111 ScN rocksalt phase [55]. The presence of such phase in the central area of the wafer is apparently related to the poorer piezoelectric response revealed by the SMRs frequency response as well as to the increased surface reactivity revealed by the RBS-NRBS compositional characterization.

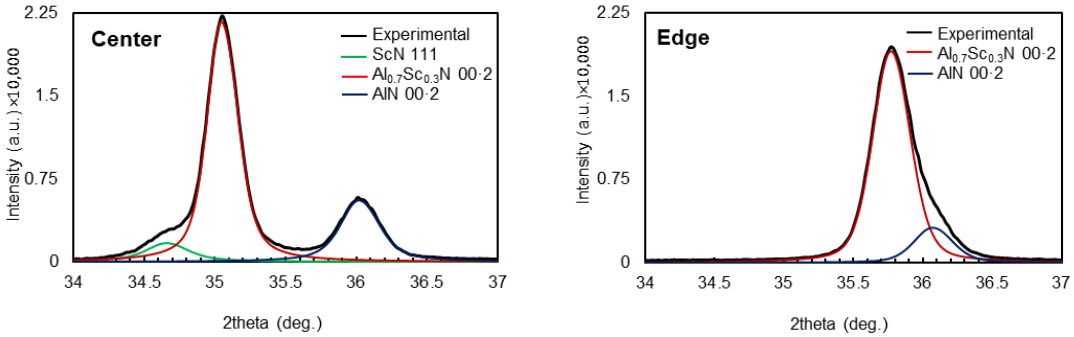

(a) (b)

Figure 3.23. (a) Deconvoluted XRD pattern for a sample located at the center and (b) at the edge of the wafer.

In order to gain more insight about the structural homogeneity and thermal stability of the $Al_{0.7}Sc_{0.3}N$ films, XRD measurements were performed on five samples taken from equidistant positions along the wafer radius, before and after annealing at 600°C and 700°C. The theta-2 theta patterns of Figure 3.24 led to the following conclusions:

1. The AlN seed layer is indeed homogeneous along the wafer and exhibits high thermal stability.
2. The ScN rocksalt phase is apparently present in all the central areas (up to position 3), although the peak deconvolution does not allow us to draw significant conclusions about its thermal stability.
3. The shift of the 00·2 $Al_{0.7}Sc_{0.3}N$ towards higher angles is confirmed, suggesting a stress gradient along the radius of the wafer in the as-deposited samples.

When bringing the thermal treatments into discussion, the XRD patterns clearly reveal considerable changes affecting the 00·2 $Al_{0.7}Sc_{0.3}N$ reflection. A severe reduction in the peak intensities accompanied by a widening of the FWHM is observed. Peak deconvolution after the heating treatments is not straightforward: the significant flattening of the main features after the treatments in all positions except in external areas might suggest an in-depth stress gradient in the $Al_{0.7}Sc_{0.3}N$ film and/or a decrease in the crystallite size. The shift to lower 2-theta angles is also observed in similar recent investigations of 00·2 $Al_{0.7}Sc_{0.3}N$ peaks after thermal treatments [56].

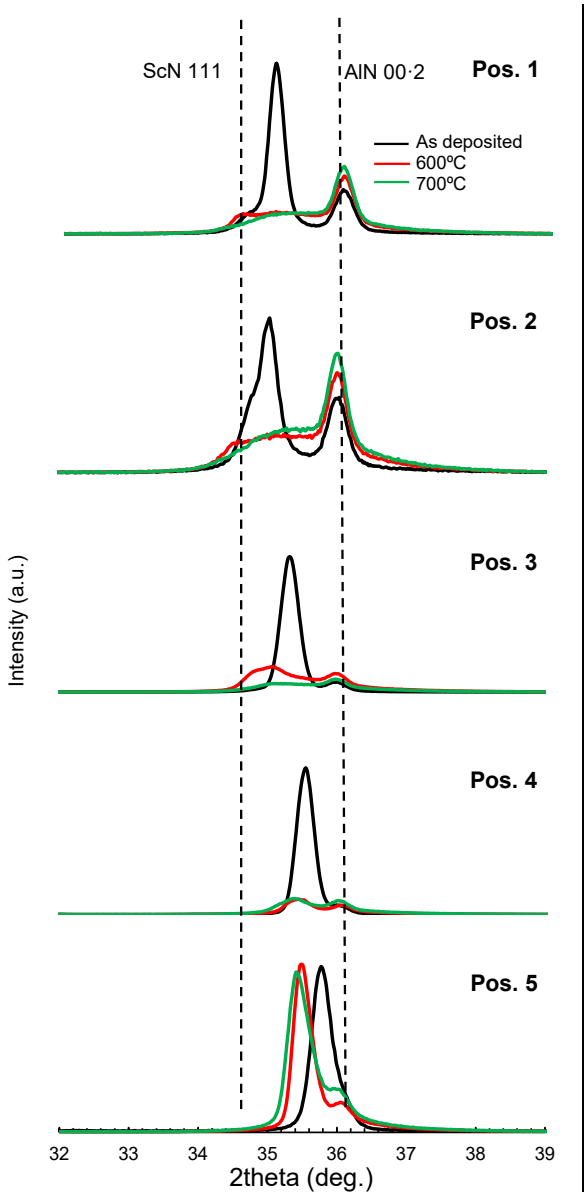

Figure 3.24. XRD patterns from the $Al_{0.7}Sc_{0.3}N$ on Si films as deposited and after 600°C and 700°C thermal treatments, going from the center (Pos. 1) to the edge (Pos. 5) of the 8-inch wafer.

The RCs of the $Al_{0.7}Sc_{0.3}N$ and AlN peaks were also measured and fitted using gaussian functions to obtain their FWHM for the as deposited films and after 600°C annealing. The results are gathered in Table 3.13, together with their corresponding standard errors. The RC around the AlN 00·2 peak shows minor variations across the radius of the wafer, keeping an almost constant value after the annealing. Concerning the rest of the RCs at the wafer center, no clear pattern is observed. This could reinforce the idea that relevant structural changes occur once the thermal treatment is applied and that for this film region, the deposited material lacks stability and homogeneity. A similar behavior is observed for RCs in the mid-radius

region. However, the fitted values for the external region reveal that the $Al_{0.7}Sc_{0.3}N$ RCs remain similar, implying that the crystallites of this region could have a more stable structure.

Table 3.13. FWHM values for the RC measurements.

Al0.7Sc0.3N-00·2 Peak		
Distance from center (cm)	**FWHM As dep.**	**FWHM @600 °C**
0–2	2.09 ± 0.01	3.04 ± 0.02
4–6	1.78 ± 0.01	2.68 ± 0.01
8–10	1.32 ± 0.01	1.35 ± 0.01
AlN-00·2 peak		
Distance from center (cm)	**FWHM As dep.**	**FWHM @600 °C**
0–2	2.59 ± 0.01	2.61 ± 0.01
4–6	2.62 ± 0.01	2.74 ± 0.02
8–10	2.58 ± 0.02	2.65 ± 0.01

In summary, the results of the composition and structural characterization might help explain, in part, the piezoelectric behavior observed in Figure 3.18. As RBS-NRA results suggested first, the excessive bombardment during the deposition phase might have produced $Al_{0.7}Sc_{0.3}N$ films with a large number of structural defects in central regions. This, together with the presence of an extra XRD peak related to a ScN non-piezoelectric phase, may explain the poor k_{eff}^2 values obtained when characterizing the fabricated SMRs. This hypothesis might be well supported by the XRD patterns in Figure 3.23 in which one can observe the instability of these regions after applying thermal treatments. On the other hand, external regions seem to have fewer structural defects and a more stable crystalline structure, which could be the main reason for the good k_{eff}^2 values obtained. However, it is worth noting that structural changes are also observable in these regions as well since these values slightly drop after thermal treatment.

For sensor applications, $Al_{0.7}Sc_{0.3}N$-based SMRs show good k_{eff}^2 and offer the possibility of operation at high frequencies. However, the measured Q factors are lower than those achieved es in AlN-based SMRs, suggesting that LOD and resolution could be smaller, also making the tracking of resonant and anti-resonant frequencies more difficult. Moreover, their lack of stability after high temperature exposition could make them not suitable for certain functionalization processes and for operation under harsh environmental conditions.

3.5. SMR FABRICATION ROUTE

The final SMR structure is obtained after following a number of fabrication steps thought to manufacture each part of the device. Each new step needs also to be designed taking into consideration the whole structure to not cause any unwanted harm or degradation to the rest of the parts conforming the device.

All the SMRs for this thesis were manufactured using the deposition parameters explained throughout this section. To obtain the final stack, the following recipe was used:

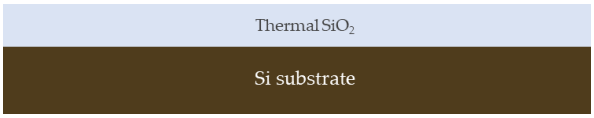

- On a 4-inch high ρ Si wafer, the first SiO_2 layer is grown via thermal oxidation.

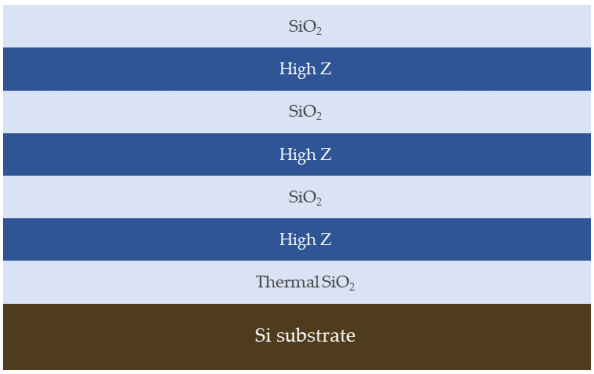

- Sputtering deposition of alternating layers of SiO_2 (low acoustic impedance) and high acoustic impedance material (Mo, AlN, ZnO, Ta_2O_5 or HfN) to make a 7 layer acoustic reflector. For the Mo/SiO_2 reflectors, thin Ti films are also sputtered between layers to improve adherence.

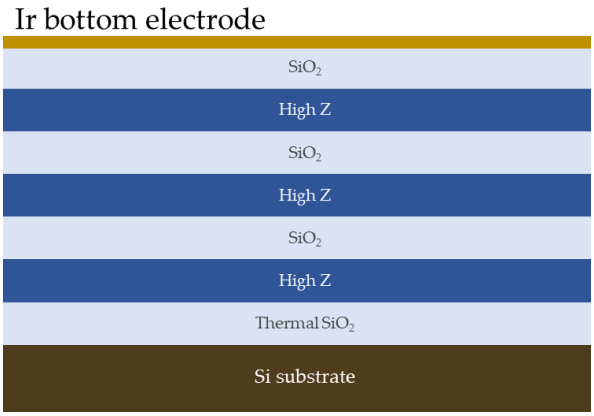

- After mechanical polishing, sputtering of a thin Ti layer and deposition of Ir bottom electrode via e-beam evaporation. In some cases, to avoid the appearance of a split mode [29], an extra Mo sacrificial layer is deposited to pattern the bottom electrode and etch the desired Ir and Ti areas.

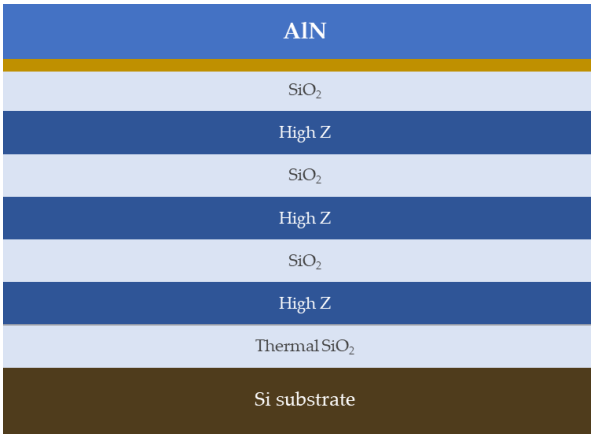

- Deposition of a high quality AlN film via T assisted reactive pulsed dc magnetron sputtering to act as piezoelectric layer.

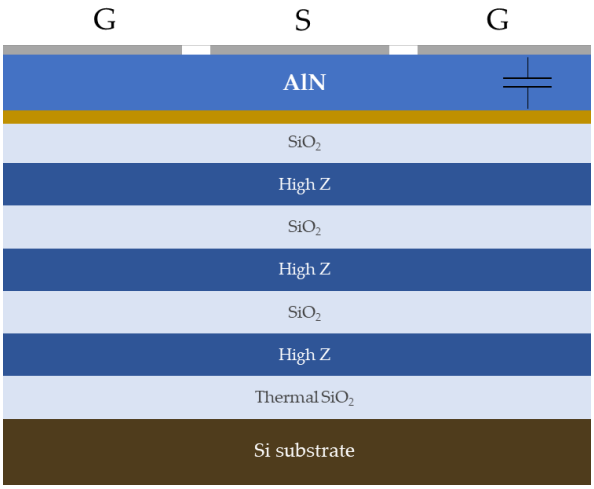

- Sputtering of the top electrode (Mo or Mo/Au) and patterning via photolithographic process. Mo electrodes are etched by chemical wet etching and Mo/Au are defined by lift-off process. With this configuration, bottom electrode is contacted through capacitive coupling, eliminating the need of etching the piezoelectric layer.

3.6. FUNCTIONALIZATION

AlN-based SMRs play the role of transducers when they are intended for gas/particle sensor applications. To manufacture an operational sensor, a functionalization process is required to develop a sensing layer capable of detecting the desired analyte . Thus, extra fabrication steps are often needed once the SMR route is finished. These functionalization steps need to meet certain requirements in order to obtain a fully functional SMR sensor:

- They need to be sensitive to the proposed analyte, and they need to show high selectivity to avoid false positives and cross-sensitivity issues.
- They need to be able to work under specific environmental conditions, since harsh environments are one of the main targets of the thesis.

- Their fabrication and integration processes need to be compatible with the rest of the SMR structure. Thus, not all the potential sensing layers can be studied as their associated functionalization process could harm the resonator and the final device response could be too deteriorated to have a functional sensor.

To optimize sensitivity, sensing layers need to cover the maximum possible area of the resonator. However, sensing layers are rarely composed of conductive materials, so it is important to leave some uncoated areas to make electrical contact. The most common electrode topology used for this thesis is represented in Figure 3.25. In this design, most of the top electrode area is coated with the functionalization layer to form the SMR sensor structure, leaving a short pad to make electrical contact and allow excitation of the piezoelectric layer. This functionalization layer causes the resonance to drop to lower frequency values and increase acoustic losses, so high Q factor values are required. Moreover, if bottom electrode pad is not properly etched, a split mode can appear [29], which could be an undesired effect for certain device designs and applications.

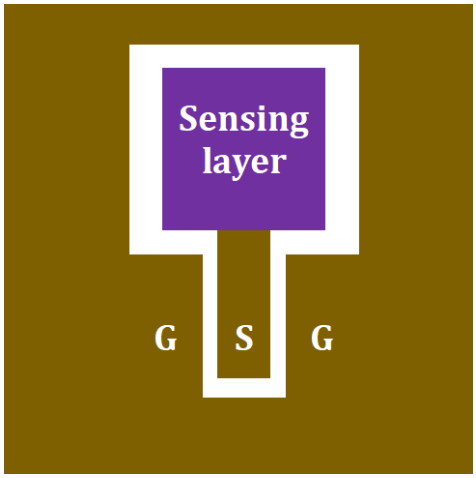

Figure 3.25. Top side representation of the topology of the top electrode plus sensing layer of an AlN-based SMR sensor.

Functionalization processes based on thin film deposition techniques emerge as a convenient choice for achieving a final layout like the one depicted in Figure 3.25. By means of chemical etching or lift-off processes, the final sensing area can be precisely defined without harming the integrity of the resonator structure. The recipes proposed for this thesis all include these techniques and will be described in this section.

3.1.5. Pentacene thin films

Sensing layers intended to work at room temperature usually have no limitations as they are not required to withstand temperature-related harsh conditions for proper operation. Therefore, organic composites are often used as active layers for gas sensors at room temperature, as they offer high sensitivity and easy, low-cost synthesis processes [57].

Although not very common, some organic materials can be deposited on substrates via PVD techniques. This is the case of pentacene, which is an organic material that can be presented in thin film form. Its structure consists of five benzene rings linearly chained, as depicted in Figure 3.26. Depending on the deposition parameters, pentacene films can show different arrangements, such as the thin film, low temperature and high temperature phases [58]. Commonly used for organic thin film transistors [59], pentacene has also been explored as sensing layer for gas sensors at room temperature, particularly for detecting NO_x in low concentrations, showing high selectivity towards these gas species [60], [61].

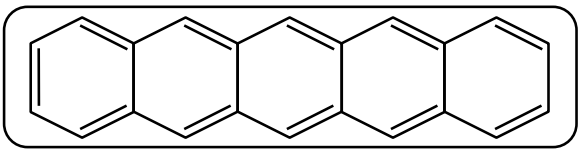

Figure 3.26. Pentacene chemical structure [62].

Parting from AlN-based SMRs on AlN/SiO_2 acoustic reflectors as substrates, pentacene thin films were deposited via thermal evaporation to act as sensing layers for NO gas at room temperature. Pentacene powder (TCIAP0030) used as source material was acquired from VWR. The SMRs were previously coated with developed photoresist to perform a lift-off process and remove the deposited pentacene from the undesired parts of the devices. An optical microscope picture is shown in Figure 3.27. As can be observed from the picture, part of the Ir bottom electrode is also removed prior to AlN deposition to avoid the appearance of split modes.

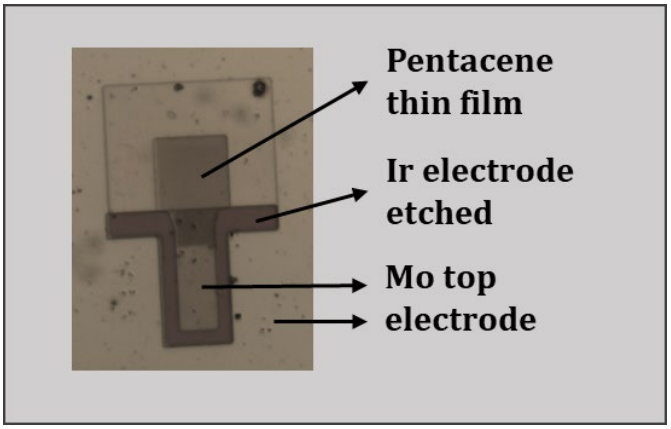

Figure 3.27. SMR device with pentacene active layer.

The evaporated pentacene films were characterized by profilometry technique, revealing an average thickness of 50 nm. Their crystalline structure was assessed by Raman spectroscopy, and the measured spectra before and after deposition on SMRs surface is shown in Figure 3.28. The measured spectrum after pentacene evaporation shows some of the characteristic Raman active modes of this material. The peaks in the 1150-1200 cm^{-1} region correspond to the C-H bending vibrational modes, whereas the peaks beyond 1300 cm^{-1} are related to C-C vibrational modes [63], [64]. The position of the band around 1370 cm^{-1} and its relative intensity suggests the pentacene films are arranged in high temperature phase [65].

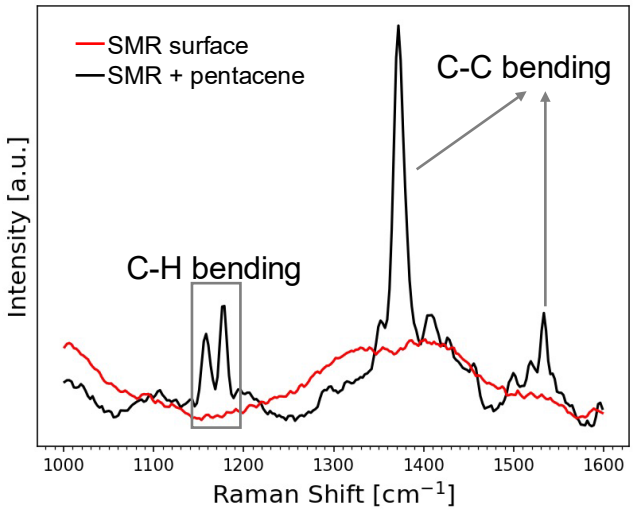

Figure 3.28. Raman spectra of the SMR surface before and after pentacene evaporation.

The response of the resultant device is shown in Figure 3.29. The measured resonance is centered around 2.6 GHz. The functionalization process seems to cause

a degradation in the resonant frequency as the Q factor calculation reveals. However, anti-resonant frequency shows good Q value, meaning that the device after functionalization is suitable for sensor applications.

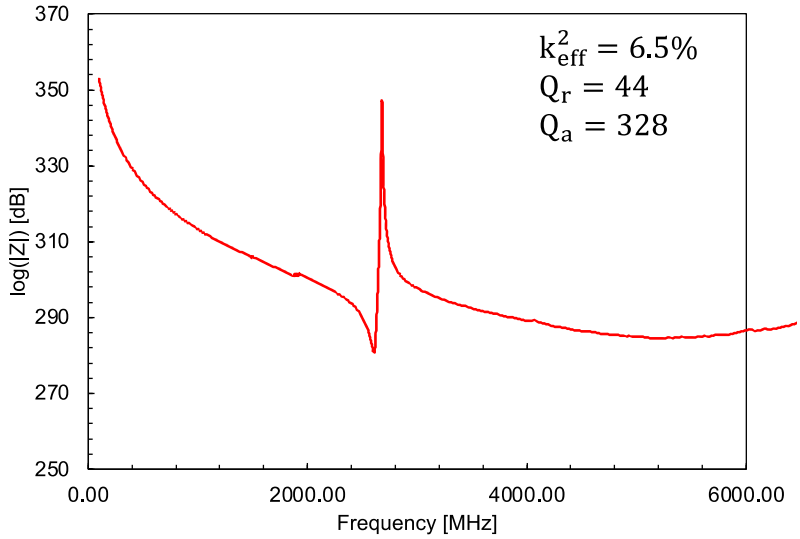

Figure 3.29. Frequency response of the AlN-based SMR+pentacene sensing layer.

3.1.6. CNT forests

Following an already developed and studied process in our group [6], [66]–[68], CNT forests were grown on top of AlN-based SMRs to act as sensing layers at room temperature. This configuration could also be used as substrate to add extra functionalization steps to enhance sensitivity and/or selectivity [69]–[71]. However, for this thesis, the CNT+SMR structures were used to test the proper functioning of the homemade gas sensing setup described in previous chapter.

The CNT forests are grown from catalytic nanoparticles (NPs) that are formed on top of the resonators and enable selective growth. Once the SMR structure is fabricated, a 12 nm Al layer and a 6 nm Fe layer are deposited via thermal evaporation and defined on the active area using lift-off process, leaving the same layout as the one depicted in Figure 3.25. The Al layer is evaporated to act as protective layer and prevent diffusion between the top electrode and the Fe layer, which is deposited as a precursor for the NP nucleation process. The CNT growth process is achieved via CVD. First, the substrate is introduced in the chamber and pumped down to rough vacuum conditions. To ensure the interior of the CVD chamber is clean, several purge-vacuum N_2 cycles are performed. Then, the

substrate is heated to 450°C in NH_3 atmosphere with a chamber pressure of 17.3 Pa. Once the temperature is reached, these conditions are maintained during 10 min to ensure Fe NP formation. The CNTs are then grown at 650°C in NH_3:C_2H_2 atmosphere in a 1:1 ratio at 32 Pa for 8 min. After the process, the sample is let cool down in vacuum [6]. A typical device with CNT forest integration is shown in Figure 3.30(a) and its cross-section in Figure 3.30(b). The frequency response is show in Figure 3.31, indicating that resonant frequency can be used as the tracking frequency for sensor applications.

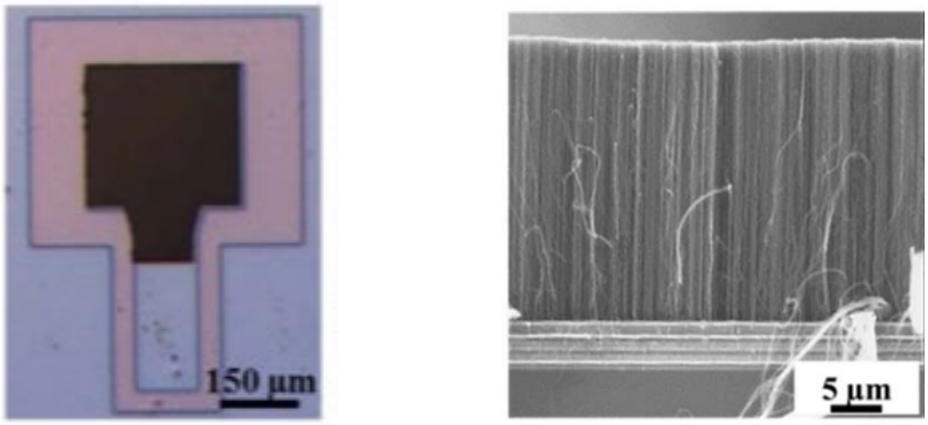

Figure 3.30. (a) top view of an AlN-bases SMR coated with a CNT forest and (b) SEM micrograph of the cross-section of the device [66].

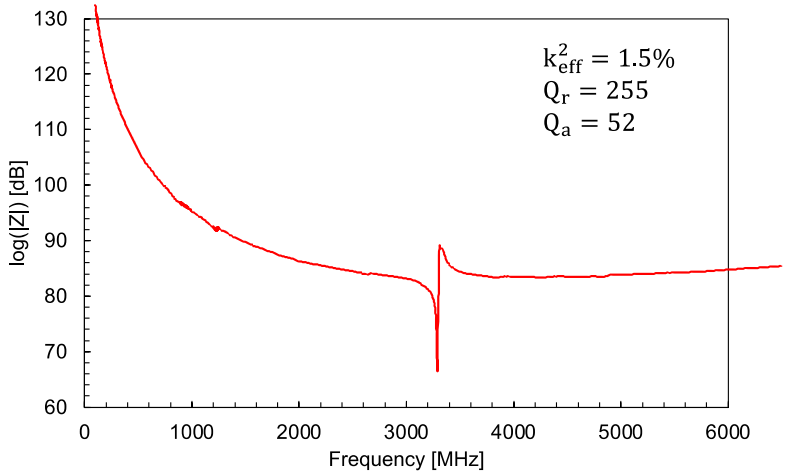

Figure 3.31. Frequency response of the SMR+CNT forest structure.

3.1.7. WO_3 films

Metal oxides have been proven to be useful sensing layers for gas detection due to activation of redox reactions at high temperatures [72], [73]. Although their formation can be achieved through chemical processes such like sol-gel method [74], sputtered metal oxides are also a good alternative and their performance in gas sensing application has also been demonstrated, especially as chemiresistive sensors [75], [76]. Regarding SMR based sensors, functionalization via sputtering of thin films is a very convenient way of achieving a functional sensor without complicating the whole recipe and without compromising the rest of the structure.

For this thesis, WO_3 films were sputtered on AlN-based SMRs. The devices followed a conventional configuration, represented in Figure 3.32(a). The WO_3 films were sputtered on the SMRs and defined via lift-off process, as can be observed from Figure 3.32(b).

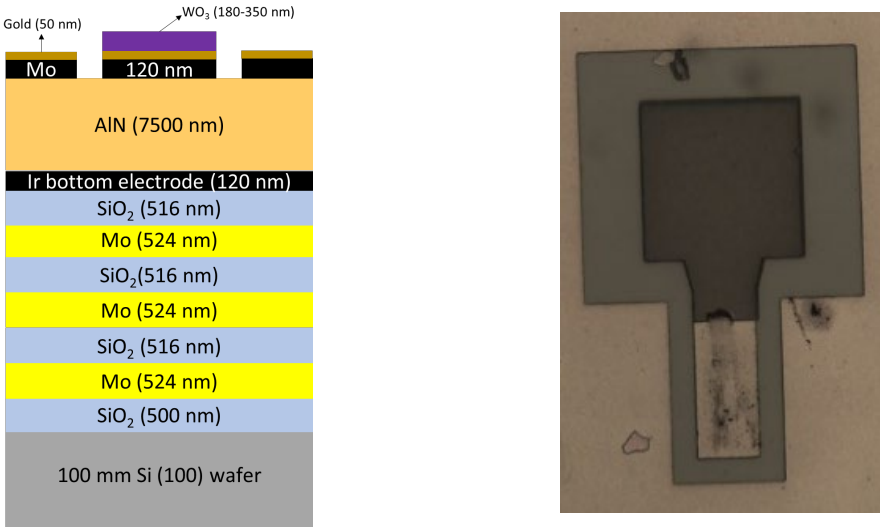

(a) (b)

Figure 3.32. (a) Design of the SMR functionalized with sputtered WO_3 films and (b) optical microscope image of the top view.

The sputtering process was carried out from a W target at room temperature. Two different Ar/O_2 (50:50 and 70:30) atmospheres were tested, keeping process pressure and power at 0.15 Pa and 100 W. Some of the samples were also deposited positioning the substrate with a 45° tilt with respect to the W target to increase the roughness of the sensing layer and try to enhance the effective sensing area. The

sputtering conditions gathered in Table 3.14. The process was conducted directly on the AlN-based SMRs acting, defining the sensing area on the Mo/Au top electrodes by lift-off process. The sputtering power is sufficiently low to not burn the developed photoresist. Once the WO_3 layers are integrated on the surface of the SMRs, an annealing treatment in air was performed at 350 °C for 12 hours.

Table 3.14. WO_3 sputtering conditions.

WO_3 layer (label)	Pressure [Pa]	Power [W]	O_2 conc. [%]	Thickness [nm]
Tilted-1	0.15	100	50	190
H-1	0.15	100	50	220
Tilted-2	0.15	100	50	330
H-2	0.15	100	30	270
Tilted-3	0.15	100	30	320

Good crystalline quality is essential for a metal oxide layer to function as sensing layer. Raman spectra showed that sputtered WO_3 films on SMRs tend to grow with a very poor crystalline structure, as it can be seen from figure 3.33. The lack of the most characteristic Raman modes of WO_3 suggest that the thin films are practically amorphous after the sputtering deposition. However, the spectra took after the 350 °C annealing show a remarkable improvement in the crystalline structure of the films. The most prominent peaks are the ones located at 710 cm^{-1} and 801 cm^{-1}. These peaks are related to asymmetric and symmetric W-O-W stretching modes, respectively, and are often associated with the monoclinic phase of WO_3 [77], [78]. Additional observed peaks after annealing are the 260 cm^{-1} and 320 cm^{-1}, commonly associated to O-W-O bending modes [79]. Finally, the peaks located at 123 cm^{-1} and 650 cm^{-1} correspond to a lattice mode and a stretching mode similar to the 710 cm^{-1} one but in presence of water molecules, respectively [80]. As it also can be observed from Figure 3.33, no significant difference is appreciated between the two different sputtering processes for WO_3 thin films, so they seem to behave in a similar manner before and after annealing, going from nearly amorphous to the highly dominant monoclinic phase observed from Raman spectra.

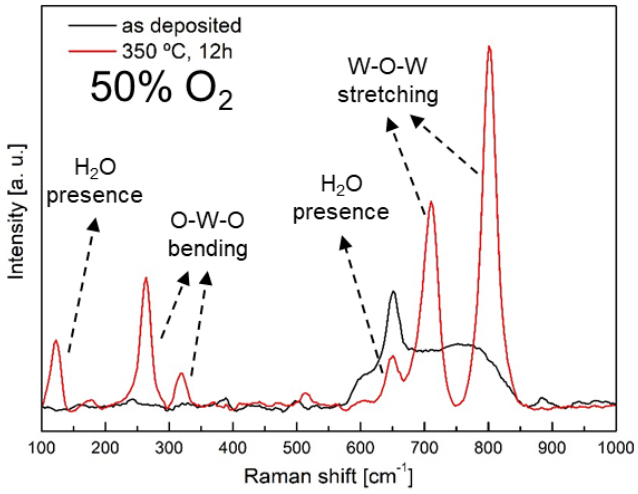

(a)

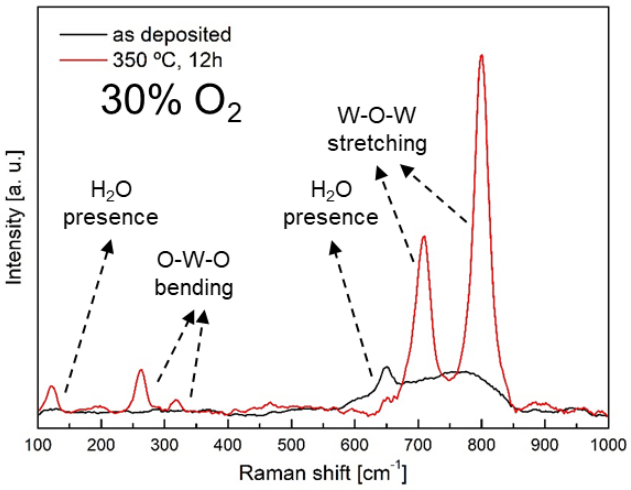

(b)

Figure 3.33. Raman spectra of the as deposited (black) and after annealing (red) WO_3 thin films for the (a) 50:50 Ar:O_2 gas mixture and (b) 70:30 Ar:O_2 gas mixture during the sputtering process.

Topography and grain size analysis from AFM characterization reveal a quite homogeneous behavior for the different WO_3 deposition conditions studied in this work. In terms of surface roughness, the measurements reflect a slight increase after the annealing treatment, going from an average 20.48 nm to 22.93 nm, which is consistent with the literature [81]. The values of the RMS surface roughness measurements for all the WO_3 sensing layers after the annealing process are shown in Figure 3.34(a). In all the studied samples, the WO_3 films grown on SMRs show a remarkable variability in terms of grain size, going from 40 nm to 170 nm in diameter. This variability, together with the mean roughness measurements, can indicate that the films are highly microstructured and show a high surface ratio, a rather helpful property for sensing applications. The 3D micrographs shown in

Figure 3.34 show the dispersion in grain sizes and high roughness profiles. It can also be noted that the Figure 3.34(b) image reveals tilted grains as a consequence of the sputtering conditions, in opposition to the surface shown in Figure 3.34(c), in which the WO_3 film is sputtered with a regular substrate-target disposition. However, the observed tilted grains do not exhibit a straightforward correlation with improved sensor performance, as will be discussed further in next chapter.

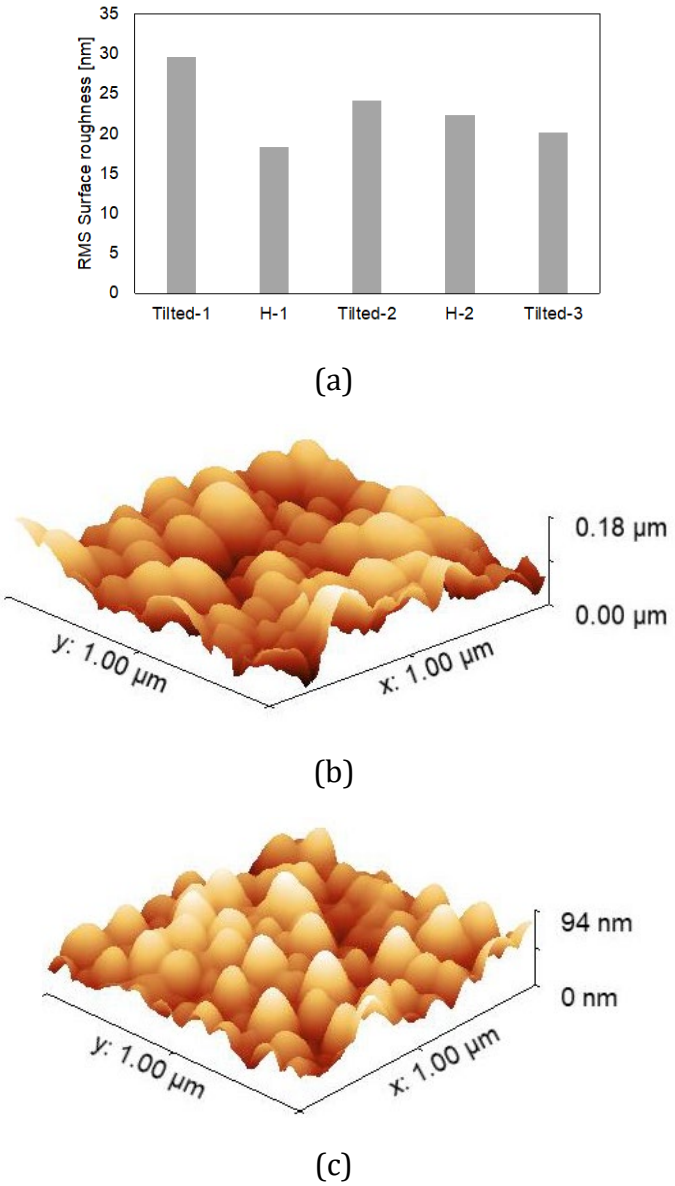

Figure 3.34. (a) RMS surface roughness of the WO_3 films after annealing. AFM 3D topography images of WO_3 films deposited by (b) 45º tilted sputtering and (c) regular sputtering conditions.

The frequency response of a typical device can be observed in Figure 3.35. The final layout after defining the WO_3 sensing layer causes the generation of two

resonances. This behavior will be further described in next chapter. The study of the resonant and anti-resonant frequencies reveals that although presenting low electromechanical coupling values, Q factors are good enough for the devices to operate as high sensitivity gas sensors.

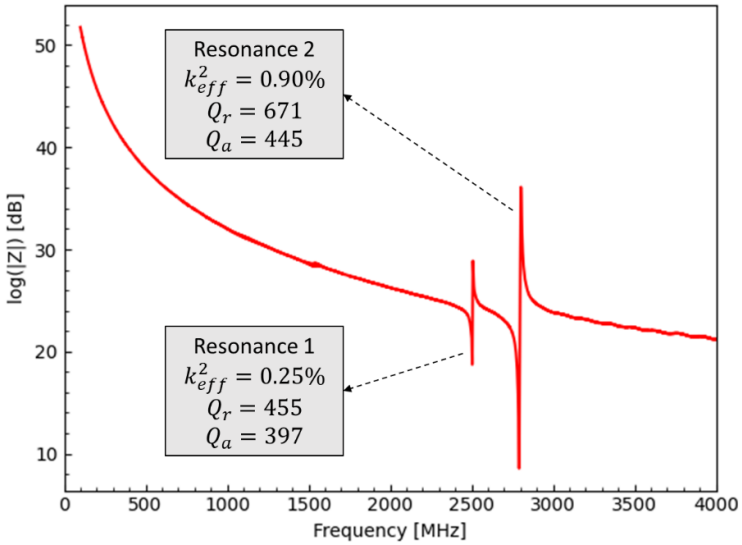

Figure 3.35. Frequency response of WO_3-SMR sensor.

References

[1] W. P. Mason, *Electromechanical Transducers and Wave Filters*. New York: Van Nostrand, 1942.

[2] K. Hashimoto, *RF Bulk Acoustic Wave Filters for Communications*. Artech House, 2009.

[3] M. de Miguel Ramos, "High sensitivity biosensors based on shear mode AIN resonators for in liquid operation," Ph.D. dissertation, Electronic Engineering Department, Universidad Politécnica de Madrid, 2015. doi: 10.20868/UPM.thesis.39314.

[4] D. M. Pozar, *Microwave and Rf Design of Wireless Systems*, First. Wiley, 2000.

[5] K. M. Lakin, "Modeling of thin film resonators and filters," *IEEE MTT-S Intern. Microw. Symp. Digest*, vol. 1, pp. 149–152, Jun. 1992, doi: 10.1109/MWSYM.1992.187931.

[6] T. Mirea, "Thin film electroacoustic resonators for physical and chemical sensing," Ph.D. dissertation, Electronic Engineering Department, Universidad Politécnica de Madrid, 2017. doi: 10.20868/UPM.thesis.45713.

[7] S. Huang *et al.*, "A Solidly Mounted Resonator Fabricated by $LiNbO_3$ Single-Crystalline Film on Flexible Polyimide Substrate," *IEEE Trans. Ultrason. Ferroelectr. Freq. Control*, vol. 68, no. 7, pp. 2585–2589, Jul. 2021, doi: 10.1109/TUFFC.2021.3066589.

[8] J. Olivares, E. Wegmann, M. Clement, J. Capilla, E. Iborra, and J. Sangrador, "Assessment of solidly mounted resonators with wide-band asymmetric acoustic reflectors," *Proc. IEEE Ultrason. Symp.*, pp. 1677–1680, 2010, doi: 10.1109/ULTSYM.2010.5935777.

[9] R. Aigner *et al.*, "Bulk-acoustic-wave filters: Performance optimization and volume manufacturing," in *IEEE MTT-S Intern. Microw. Symp. Digest*, 2003, pp. 2001–2004. doi: 10.1109/mwsym.2003.1210552.

[10] C. Han *et al.*, "Solidly mounted resonator sensor for biomolecule detections," *RSC Adv.*, vol. 9, no. 37, pp. 21323–21328, 2019, doi: 10.1039/c9ra01695c.

[11] M. Demiguel-Ramos, T. Mirea, J. Olivares, M. Clement, J. Sangrador, and E. Iborra, "Assessment of the shear acoustic velocities in the different materials composing a high frequency solidly mounted resonator," *Ultrasonics*, vol. 62, pp. 195–199, Sep. 2015, doi: 10.1016/J.ULTRAS.2015.05.017.

[12] M. Demiguel-Ramos *et al.*, “Influence of the electrical extensions in AlN-BAW resonators for in-liquid biosensors,” *2014 European Freq. and Time Forum, EFTF 2014*, pp. 301–304, 2015, doi: 10.1109/EFTF.2014.7331492.

[13] J. M. Carmona-Cejas, T. Mirea, M. Clement, and J. Olivares, “Comparative study of fully-dielectric acoustic reflectors in solidly mounted resonators,” in *IEEE Intern. Ultrason. Symp., IUS*, 2021, doi: https://doi.org/10.1109/IUS52206.2021.9593421.

[14] M. Demiguel-Ramos *et al.*, “Hafnium Nitride as High Acoustic Impedance Material for Fully Insulating Acoustic Reflectors,” in *IEEE Intern. Ultrason. Symp., IUS*, 2018, pp. 14–17. doi: 10.1109/ULTSYM.2018.8579935.

[15] Y. Lu *et al.*, “Surface Morphology and Microstructure of Pulsed DC Magnetron Sputtered Piezoelectric AlN and AlScN Thin Films,” *Physica Status Solidi (A) Applic. and Mater. Sci.*, vol. 215, no. 9, p. 1700559, May 2018, doi: 10.1002/pssa.201700559.

[16] P. Bindu and S. Thomas, “Estimation of lattice strain in ZnO nanoparticles: X-ray peak profile analysis,” *J. of Theoretical and Appl. Phys.*, vol. 8, no. 4, pp. 123–134, Dec. 2014, doi: 10.1007/S40094-014-0141-9/FIGURES/9.

[17] S. Yun, L. Wang, W. Guo, and T. Ma, “Non-Pt counter electrode catalysts using tantalum oxide for low-cost dye-sensitized solar cells,” *Electrochem. Commun.*, vol. 24, no. 1, pp. 69–73, Oct. 2012, doi: 10.1016/j.elecom.2012.08.008.

[18] A. Courrech Arias, L. García González, J. Hernández Torres, T. Hernández Quiroz, and G. Galicia Aguilar, “Analysis of hardness, resistivity and corrosion of HfN thin films fabricated by D.C. sputtering,” in *Adv. Mater. Res.*, , 2014, pp. 93–97. doi: 10.4028/www.scientific.net/AMR.976.93.

[19] J. Wang, Z. Chen, C. Li, F. Wang, and Y. Zhong, “First-principles study on mechanical properties of IVB-group transition-metal nitrides TiN, ZrN, and HfN,” in *Adv. Mater. Res.*, 2012, pp. 1451–1456. doi: 10.4028/www.scientific.net/AMR.415-417.1451.

[20] J. Capilla, J. Olivares, M. Clement, J. Sangrador, E. Iborra, and A. Devos, “High-acoustic-impedance tantalum oxide layers for insulating acoustic reflectors,” *IEEE Trans. Ultrason. Ferroelectr. Freq Control*, vol. 59, no. 3, pp. 366–372, 2012, doi: 10.1109/TUFFC.2012.2205.

[21] E. Török and J. Perry, “Young’s Modulus of TiN, TiC, ZrN and HfN,” *Thin Solid Films*, vol. 153, pp. 37–43, 1987.

[22] G. N. Saddik, D. S. Boesch, S. Stemmer, and R. A. York, “Strontium titanate DC electric field switchable and tunable bulk acoustic wave solidly mounted resonator,” *2008 IEEE MTT-S Intern. Microw. Symp. Digest,* pp. 1263–1266, Sep. 2008, doi: 10.1109/MWSYM.2008.4633289.

[23] T. Mirea, J. Olivares, M. Clement and J. Sangrador, “AlN-based solidly mounted resonators at 400°C: In-situ performance monitoring,” *IEEE Intern. Ultras. Symp., IUS*, 1700–1702, Oct. 2019 https://doi.org/10.1109/ULTSYM.2019.8925697.

[24] J. P. Specht, S. Esfahani, Y. Xing, A. Kock, M. Cole, and J. W. Gardner, “Thermally Modulated CMOS-Compatible Particle Sensor for Air Quality Monitoring,” *IEEE Trans. Instrum. Meas.*, vol. 71, 2022, doi: 10.1109/TIM.2022.3141151.

[25] X. Bai *et al.*, “The thin film bulk acoustic wave resonator based on single-crystalline 43-Ɔ Y-cut lithium niobate thin films,” *AIP Adv.*, vol. 10, no. 7, 2020, doi: 10.1063/1.5143550.

[26] C. L. Wei, Y. C. Chen, C. C. Cheng, and K. S. Kao, “Solidly mounted resonators consisting of a molybdenum and titanium Bragg reflector,” *Appl. Phys. A Mater. Sci. Process*, vol. 90, no. 3, pp. 501–506, Mar. 2008, doi: 10.1007/s00339-007-4312-2.

[27] T. Mirea, M. Clement, J. Olivares, and E. Iborra, “Assessment of the Absolute Mass Attachment to an AlN-Based Solidly Mounted Resonator Using a Single Shear Mode,” *IEEE Electron Device Lett.*, vol. 41, no. 4, pp. 609–612, Apr. 2020, doi: 10.1109/LED.2020.2976490.

[28] G. Rughoobur *et al.*, “Room temperature sputtering of inclined c- axis ZnO for shear mode solidly mounted resonators,” *Appl. Phys. Lett.*, vol. 108, no. 3, Jan. 2016, doi: 10.1063/1.4940683.

[29] E. Wajs, G. Rughoobur, K. Burling, A. George, A. J. Flewitt, and V. J. Gnanapragasam, “A novel split mode TFBAR device for quantitative measurements of prostate specific antigen in a small sample of whole blood,” *Nanoscale*, vol. 12, no. 17, pp. 9647–9652, May 2020, doi: 10.1039/D0NR00416B.

[30] L. Ma *et al.*, “Bulk acoustic wave resonance characteristic modified by reducing the defects in ZnO-based solidly mounted resonators,” *Mater. Sci. Semicond. Process*, vol. 137, p. 106216, Jan. 2022, doi: 10.1016/J.MSSP.2021.106216.

[31] E. Iborra, M. Clement, J. Capilla, J. Olivares, and V. Felmetsger, “Low-thickness high-quality aluminum nitride films for super high frequency solidly mounted resonators,” *Thin Solid Films*, vol. 520, no. 7, pp. 3060–3063, Jan. 2012, doi: 10.1016/j.tsf.2011.11.007.

[32] M. DeMiguel-Ramos, T. Mirea, M. Clement, J. Olivares, J. Sangrador, and E. Iborra, “Optimized tilted c-axis AlN films for improved operation of shear mode resonators,” *Thin Solid Films*, vol. 590, pp. 219–223, Sep. 2015, doi: 10.1016/J.TSF.2015.08.010.

[33] J. Bjurström, G. Wingqvist, and I. Katardjiev, “Synthesis of textured thin piezoelectric AlN films with a nonzero C-axis mean tilt for the fabrication of shear mode resonators,” *IEEE Trans. Ultrason. Ferroelectr. Freq. Control*, vol. 53, no. 11, pp. 2095–2100, Nov. 2006, doi: 10.1109/TUFFC.2006.149.

[34] M. Bousquet *et al.*, “Lithium niobate film bulk acoustic wave resonator for sub-6 GHz filters,” in *IEEE Intern. Ultrason. Symp., IUS*, IEEE Computer Society, Sep. 2020. doi: 10.1109/IUS46767.2020.9251654.

[35] M. Moreira, J. Bjurström, I. Katardjev, and V. Yantchev, “Aluminum scandium nitride thin-film bulk acoustic resonators for wide band applications,” *Vacuum*, vol. 86, no. 1, pp. 23–26, 2011, doi: 10.1016/j.vacuum.2011.03.026.

[36] R. S. Feigelson, “Epitaxial growth of lithium niobate thin films by the solid source MOCVD method,” *J. Crystal Growth*, vol. 166, 1-4, Sep. 1996, doi: 10.1016/0022-0248(95)00570-6.

[37] A. M. Marsh, S. D. Harkness, F. Qian, and R. K. Singh, “Pulsed laser deposition of high quality $LiNbO_3$ films on sapphire substrates,” *Appl. Phys. Lett.*, vol. 62, no. 9, pp. 952–954, 1993, doi: 10.1063/1.108530.

[38] R. L. Paldi *et al.*, “Nanocomposite-Seeded Epitaxial Growth of Single-Domain Lithium Niobate Thin Films for Surface Acoustic Wave Devices,” *Adv. Photonics Res.*, vol. 2, no. 6, 2000149, Jun. 2021, doi: 10.1002/ADPR.202000149.

[39] M. Akiyama, K. Kano, and A. Teshigahara, “Influence of growth temperature and scandium concentration on piezoelectric response of scandium aluminum nitride alloy thin films,” *Appl. Phys. Lett.*, vol. 95, no. 162107, 2009, doi: 10.1063/1.3251072.

[40] B. Saha *et al.*, "Development of epitaxial $Al_xSc_{1-x}N$ for artificially structured metal/semiconductor superlattice metamaterials," *Phys. Status Solidi B Basic Res.*, vol. 252, no. 2, pp. 251–259, 2015, doi: 10.1002/pssb.201451314.

[41] S. Fichtner, T. Reimer, S. Chemnitz, F. Lofink, and B. Wagner, "Stress controlled pulsed direct current co-sputtered $Al_{1-x}Sc_xN$ as piezoelectric phase for micromechanical sensor applications," *APL Mater.*, vol. 3, no. 11, 2015, doi: 10.1063/1.4934756.

[42] V. Felmetsger, P. N. Laptev, and S. M. Tanner, "Design, operation mode, and stress control capability of S-Gun magnetron for ac reactive sputtering," *Surf. Coat. Technol.*, vol. 204, no. 6–7, pp. 840–844, Dec. 2009, doi: 10.1016/j.surfcoat.2009.08.007.

[43] V. Felmetsger, M. Mikhov, M. Ramezani, and R. Tabrizian, "Sputter Process Optimization for $Al_{0.7}Sc_{0.3}N$ Piezoelectric Films," *IEEE Intern. Ultrason. Symp., IUS*, vol. 2019-Octob, pp. 2600–2603, Oct. 2019, doi: 10.1109/ULTSYM.2019.8925576.

[44] R. C. Ruby, P. Bradley, Y. Oshmyansky, A. Chien, and J. D. Larson, "Thin film bulk wave acoustic resonators (FBAR) for wireless applications," *Proc. of the IEEE Ultrason. Symp.*, vol. 1, pp. 813–821, 2001, doi: 10.1109/ULTSYM.2001.991846.

[45] R. S. Naik *et al.*, "Correspondence Measurements of the Bulk, C-Axis Electromechanical Coupling Constant as a Function of AlN Film Quality," *IEEE Trans. on Ultrason. Ferroelect. and Freq. Control*, vol. 47, no. 1, pp. 292-296, Jan. 2000.

[46] O. Ambacher, "Growth and applications of Group III-nitrides," *J. of Phys. D: Appl. Phys.*, vol. 31, no. 20, pp. 26-53, 1998, doi: 10.1088/0022-3727/31/20/001.

[47] Q. W. Yang, R. C. Lin, and S. J. Sun, "Influence of AlN/ScAlN piezoelectric multilayer on the electromechanical coupling of FBAR," *Micro and Nanostructures*, vol. 174, Feb. 2023, doi: 10.1016/j.micrna.2022.207472.

[48] Y. Zou *et al.*, "Aluminum scandium nitride thin-film bulk acoustic resonators for 5G wideband applications," *Microsystems & Nanoengineering*, vol. 8, no. 1, pp. 1–7, Nov. 2022, doi: 10.1038/s41378-022-00457-0.

[49] M. Schneider, M. DeMiguel-Ramos, A. J. Flewitt, E. Iborra, and U. Schmid, "Scandium Aluminium Nitride-Based Film Bulk Acoustic Resonators," *Proc.*

West Mark Ed. Assoc. Conf., vol. 1, no. 10, p. 305, 2017, doi: 10.3390/proceedings1040305.

[50] M. Clement, V. Felmetsger, J. Olivares, T. Mirea, and J. Sangrador, "Combined assessment of $Al_{1-x}Sc_xN$ thin films by RBS, XRD, FTIR and BAW frequency response measurements," in *IEEE Intern. Ultrason. Symp., IUS*, Oct. 2019, pp. 720–723. doi: 10.1109/ULTSYM.2019.8926266.

[51] U. K. Chaturvedi, U. Steiner, O. Zak, G. Krausch, G. Schatz, and J. Klein, "Structure at polymer interfaces determined by high-resolution nuclear reaction analysis," *Appl. Phys. Lett.*, vol. 56, no. 13, pp. 1228–1230, Jun. 1990, doi: 10.1063/1.103332.

[52] C. Jeynes and J. L. Colaux, "Thin film depth profiling by ion beam analysis," *Analyst.*, vol. 141, no. 21, pp. 5944–5985, Oct. 2016, doi: 10.1039/C6AN01167E.

[53] T. C. Huang, G. Lim, F. Parmigiani, and E. Kay, "Effect of ion bombardment during deposition on the x-ray microstructure of thin silver films," *J. of Vacuum Sci. & Tech. A: Vacuum, Surfaces, and Films*, vol. 3, no. 6, pp. 2161–2166, Nov. 1985, doi: 10.1116/1.573271.

[54] M. Clement, E. Iborra, J. Sangrador, A. Sanz-Hervás, L. Vergara, and M. Aguilar, "Influence of sputtering mechanisms on the preferred orientation of aluminum nitride thin films," *J. Appl. Phys.*, vol. 94, no. 3, pp. 1495–1500, Aug. 2003, doi: 10.1063/1.1587267.

[55] C. Höglund, J. Bareo, J. Birch, B. Alling, Z. Czigány, and L. Hultman, "Cubic $Sc_{1-x}Al_xN$ solid solution thin films deposited by reactive magnetron sputter epitaxy onto ScN(111)," *J. Appl. Phys.*, vol. 105, no. 11, p. 113517, Jun. 2009, doi: 10.1063/1.3132862.

[56] R. Islam, N. Wolff, M. Yassine, G. Schönweger, B. Christian, and D.- Kiel, "On the exceptional temperature stability of ferroelectric Al," *Appl. Phys. Lett.*, vol. 118, pp. 1–11, 2021.

[57] S. S. Ba Hashwan *et al.*, "A review of piezoelectric MEMS sensors and actuators for gas detection application," *Nanoscale Res. Lett. 2023 18:1*, vol. 18, no. 1, pp. 1–41, Feb. 2023, doi: 10.1186/S11671-023-03779-8.

[58] T. Siegrist *et al.*, "A polymorph lost and found: The high-temperature crystal structure of pentacene," *Adv. Mater.*, vol. 19, no. 16, pp. 2079–2082, Aug. 2007, doi: 10.1002/ADMA.200602072.

[59] M. Kitamura and Y. Arakawa, “Pentacene-based organic field-effect transistors,” *J. of Phys. Condensed Matter*, vol. 20, no. 18, May 2008, doi: 10.1088/0953-8984/20/18/184011.

[60] Y. Zeng, W. Huang, W. Shi, and J. Yu, “Enhanced sensing performance of nitrogen dioxide sensor based on organic field-effect transistor with mechanically rubbed pentacene active layer,” *Appl. Phys. A Mater. Sci. Process*, vol. 118, no. 4, pp. 1279–1285, Mar. 2015, doi: 10.1007/s00339-014-8831-3.

[61] X. Zhuang, S. Han, B. Huai, W. Shi, and Y. Junsheng, “Sub-ppm and high response organic thin-film transistor NO_2 sensor based on nanofibrillar structured TIPS-pentacene,” *Sens. Actuators B Chem.*, vol. 279, pp. 238–244, Jan. 2019, doi: 10.1016/j.snb.2018.10.002.

[62] K. Seto and Y. Furukawa, “Study on solid structure of pentacene thin films using Raman imaging,” *J. of Raman Spectrosc.*, vol. 43, no. 12, pp. 2015–2019, 2012, doi: 10.1002/jrs.4090.

[63] C. Te Liu, W. H. Lee, and J. F. Su, “Pentacene-based thin film transistor with inkjet-printed nanocomposite high-K dielectrics,” *Active and Passive Electronic Comp.*, vol. 2012, 2012, doi: 10.1155/2012/921738.

[64] A. Brillante, R. G. D. Valle, L. Farina, A. Girlando, M. Masino, and E. Venuti, “Raman phonon spectra of pentacene polymorphs,” *Chem. Phys. Lett.*, vol. 357, no. 1–2, pp. 32–36, May 2002, doi: 10.1016/S0009-2614(02)00441-4.

[65] A. Girlando, M. Masino, A. Brillante, T. Toccoli, and S. Iannotta, “Raman Identification of Polymorphs in Pentacene Films,” *Crystals*, vol. 6, no. 4, p. 41, Apr. 2016, doi: 10.3390/CRYST6040041.

[66] T. Mirea, J. Olivares, M. Clement, J. Sangrador, and E. Iborra, “Direct integration of CNT forests on solidly mounted resonators and their influence on device performance,” *2017 Joint Conf. of the European Freq. and Time Forum and IEEE Intern. Freq. Control Symp., EFTF/IFC 2017 - Proceedings*, pp. 353–356, 2017, doi: 10.1109/FCS.2017.8088890.

[67] J. Olivares *et al.*, “Growth of carbon nanotube forests on metallic thin films,” *Carbon N Y*, vol. 90, pp. 9–15, 2015, doi: 10.1016/j.carbon.2015.03.058.

[68] S. Esconjauregui *et al.*, “Carbon nanotube forests as top electrode in electroacoustic resonators,” *Appl. Phys. Lett.*, vol. 107, no. 13, 2015, doi: 10.1063/1.4932197.

[69] M. Han, S. Jung, Y. Lee, D. Jung, and S. Kong, “PEI-functionalized carbon nanotube thin film sensor for CO_2 gas detection at room temperature,” *Micromachines (Basel)*, vol. 12, no. 9, p. 1053, Aug. 2021, doi: 10.3390/mi12091053.

[70] P. Gholami, A. Rashidi, M. Khaleghi Abbasabadi, M. Pourkhalil, M. Jahangiri, and N. Izadi, “Synthesis and characterization of ZnO-functionalized multiwall carbon nanotubes nanocomposite as NO_x gas sensor,” *Res. on Chem. Intermediates*, vol. 46, no. 8, pp. 3911–3927, Aug. 2020, doi: 10.1007/S11164-020-04181-0/SCHEMES/2.

[71] J. M. Escolano *et al.*, “Integration and Bio-Functionalization of Vertically Aligned Carbon Nanotube Forests on High Frequency AlN Gravimetric Sensors,” *Proc. West Mark Ed. Assoc. Conf.*, vol. 1, no. 10, p. 537, 2017, doi: 10.3390/proceedings1040537.

[72] L. Yang, A. Marikutsa, M. Rumyantseva, E. Konstantinova, N. Khmelevsky, and A. Gaskov, “Quasi similar routes of NO_2 and NO sensing by nanocrystalline WO_3: Evidence by in situ DRIFT spectroscopy,” *Sensors (Switzerland)*, vol. 19, no. 15, Aug. 2019, doi: 10.3390/s19153405.

[73] L. Saadi, C. Lambert-Mauriat, V. Oison, H. Ouali, and R. Hayn, “Mechanism of NO_x sensing on WO_3 surface: First principle calculations,” *Appl. Surf. Sci.*, vol. 293, pp. 76–79, Feb. 2014, doi: 10.1016/J.APSUSC.2013.12.095.

[74] Z. Li *et al.*, “Sb-doped WO_3 based QCM humidity sensor with self-recovery ability for real-time monitoring of respiration and wound,” *Sens. Actuators B Chem.*, vol. 361, p. 131691, Jun. 2022, doi: 10.1016/J.SNB.2022.131691.

[75] R. J. Rath, S. Farajikhah, F. Oveissi, F. Dehghani, and S. Naficy, “Chemiresistive Sensor Arrays for Gas/Volatile Organic Compounds Monitoring: A Review,” *Adv. Eng. Mater.*, vol. 25, no. 3, p. 2200830, Feb. 2023, doi: 10.1002/ADEM.202200830.

[76] H. G. Moon *et al.*, “On-Chip Chemiresistive Sensor Array for On-Road NO_x Monitoring with Quantification,” *Adv. Sci.*, vol. 7, no. 22, p. 2002014, Nov. 2020, doi: 10.1002/ADVS.202002014.

[77] B. Montanari, A. J. Barbosa, S. J. L. Ribeiro, Y. Messaddeq, G. Poirier, and M. S. Li, “Structural study of thin films prepared from tungstate glass matrix by Raman and X-ray absorption spectroscopy,” *Appl. Surf. Sci.*, vol. 254, no. 17, pp. 5552–5556, Jun. 2008, doi: 10.1016/j.apsusc.2008.02.107.

[78] M. Breedon *et al.*, "Synthesis of nanostructured tungsten oxide thin films: A simple, controllable, inexpensive, aqueous sol-gel method," *Cryst. Growth Des.*, vol. 10, no. 1, pp. 430–439, Jan. 2010, doi: 10.1021/cg9010295.

[79] Y. S. Zou *et al.*, "Structural and optical properties of WO_3 films deposited by pulsed laser deposition," *J. Alloys Compd*, vol. 583, pp. 465–470, Jan. 2014, doi: 10.1016/J.JALLCOM.2013.08.166.

[80] M. F. Daniel, J. C. Lassegues, B. Gerand, and M. Fjglarz, "Infrared and Raman Study of WO_3 Tungsten Trioxides and WO_3, xHzO Tungsten Trioxide Hydrates," *J. of Solid State Chem.*, vol. 67, 2, pp. 235-247, Apr. 1987.

[81] M. Stankova *et al.*, "Influence of the annealing and operating temperatures on the gas-sensing properties of rf sputtered WO_3 thin-film sensors," *Sens. Actuators B Chem.*, vol. 105, no. 2, pp. 271–277, Mar. 2005, doi: 10.1016/J.SNB.2004.06.009.

4

SMR SENSORS IN HARSH ENVIRONMENTS: RESULTS AND DISCUSSION

This chapter focuses on the response of the designed and manufactured devices throughout the thesis. Proving the versatility of SMR-based sensors, we examined their performance under different conditions depending on the temperature regime and the specific utilized sensor.

The chapter is divided in three sections depending on the working temperature: room, low and high temperature. Each section is structured as follows:

- Room temperature section includes ethanol vapor detection measurements using SMR sensors functionalized with CNT forests. This section also includes the study of NO detection by pentacene functionalized devices.
- Low temperature section focuses on the study of dual-mode resonators and their potential to decouple humidity and temperature effects from their frequency response. This effect is achieved and tested in a wide range of temperatures, going from −20 °C to room temperature.
- High temperature section covers the characterization of the sensitivity to different NO concentrations of SMR sensors functionalized with sputtered WO_3 films in the 200-350°C range. Their principle of work is thoroughly discussed, since their response seems not to be related to gravimetric detection, which is the most typical behavior for SMR based gas sensors. In this case, the frequency shift under analyte exposure can be explained by the variation in elastic properties of the functionalization layer.

4.1. ROOM TEMPERATURE

Following previous research by the group [1], [2], we conducted detection experiments for SMRs sensors at room temperature. These experiments allowed us to link previous works with the proposed objectives. The first experiment consisted in the detection and characterization of the sensitivity of SMRs functionalized with CNT forests to ethanol vapor. This experiment was also useful to check the readiness of the experimental characterization setup proposed as one of the objectives of the thesis. The second one consisted in the study of SMRs functionalized with thermally evaporated pentacene thin films as potential NO sensors. Pentacene has already been explored as NO_x sensing layer [3], [4], so its integration to SMR devices and ability to detect NO gas molecules are studied in this experiment.

4.1.1. Ethanol vapor detection with CNT functionalized SMR sensors

As stated in previous chapters, CNT forests growth is an already mature procedure well established within our group's know-how [5]–[7]. They have been used as active layers for sensor applications [8]. Extra functionalization steps to improve their properties have also been studied [9], [10]. So, their integration on the SMR top electrode and the characterization of the whole structure is a good starting point to test the experimental setup and software specifically designed for this thesis. Figure 4.1 shows the frequency response of a typical device, with its resonance centered around 3.25 GHz. The Q factor values after CNT integration are $Q_r = 150$ and $Q_a = 100$, which are low for a typical c-axis oriented AlN-based SMR device. This is due to the addition of the CNT forest to the structure, which deteriorates the performance of the longitudinal mode. However, the observed Q factor values are high enough to track the resonant and anti-resonant frequencies during sensing activities. It is also worth noting that these devices are intended to operate in a gaseous medium at room temperature, so no extra deterioration for the resonance is expected.

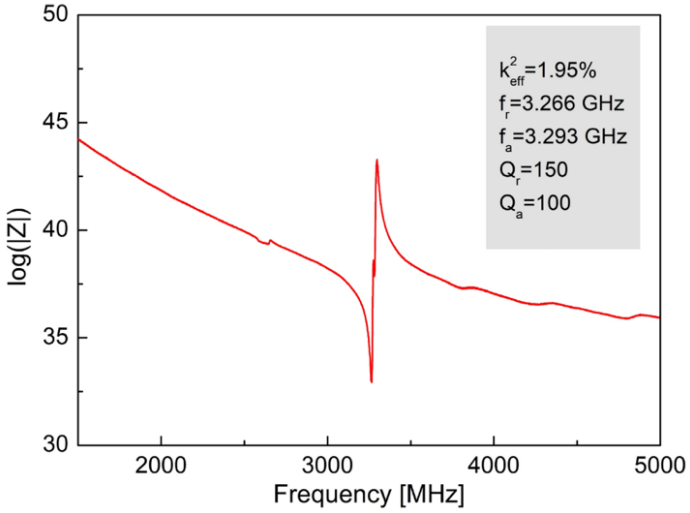

Figure 4.1. Frequency response of a SMR functionalized with CNTs SMR.

The sample devices were placed in the high temperature chamber. For this experiment, the temperature controller was kept powered off. Then, the chamber was sealed and purged with the help of a rotatory pump. Dry air was introduced to the chamber at a constant flow of 300 sccm. The ethanol vapor gas cycles were generated by a bubbler fed with dry air and filled with liquid ethanol. By mixing it with the first dry air gas line, ethanol vapor concentration in the chamber can be tuned. To test the change in sensitivity provided by the functionalization layer, we first ran ethanol vapor detection experiments to the non-functionalized SMR device. Figure 4.2(a) shows the frequency shift at resonance for three 100% ethanol vapor exposure cycles. The behavior is repeatable after each adsorption-desorption cycle, and the average shift is $\Delta f_r = -166$ kHz. The integration of CNT forests on the SMR surface enhances the sensitivity of the device for the same exposure cycles, as can be observed from Figure 4.2(b). In this case, the shift at resonance is $\Delta f_r = -791$ kHz, indicating that functionalization improves sensitivity by almost 5 times. A second cycle at a lower concentration causes a shift of $\Delta f_r = -516$ kHz, suggesting sensitivity follows a linear dependence. From the measurements taken for the two devices, the detection mechanism seems to be purely gravimetric.

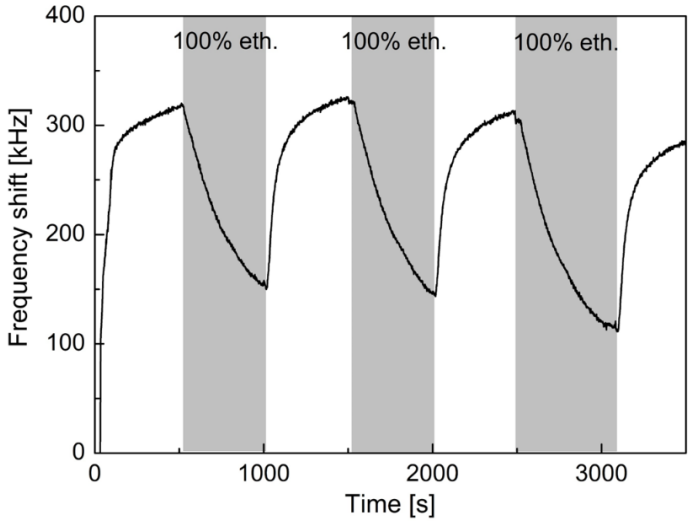

(a)

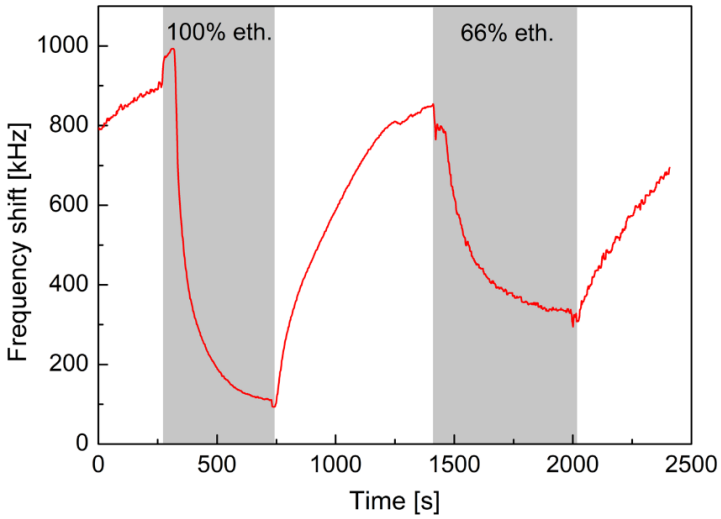

(b)

Figure 4.2. (a) Frequency shift for bare SMR and (b) CNT functionalized SMR upon ethanol vapor exposure cycles.

In summary, c-axis oriented AlN-based SMRs functionalized with CNT forests are able to successfully improve sensitivity towards ethanol vapor at room temperature. This result confirms the suitability of the CNT forest-SMR structure as gravimetric gas sensor. Extra functionalization steps, such as CNT decoration with nanoparticles, can be addressed to improve sensitivity towards this or other species, and to move operation temperatures out of room temperature range.

4.1.2. Pentacene functionalized SMR sensors for nitric oxide detection

As already stated, pentacene is an organic material composed of five chained benzene rings that can be arranged in crystalline structures. It has been studied as material to be part of organic transistors [11], [12] and, more recently, as sensing layer in NO_x gas sensors, offering good sensitivity and high selectivity towards these gas species [3], [4]. Pentacene can be deposited by thermal evaporation, which makes it a convenient candidate for SMR functionalization. For this experiment, we defined by lift-off a thermal evaporated pentacene thin films on the top electrode of c-axis oriented AlN-based SMRs. First, we evaluated the frequency response of the devices. The measured resonances were centered around 2.6 GHz, with Q factor values in the range between 50 and 350, which makes them suitable for sensor applications at room temperature. After placing them in the sensor characterization chamber and running a purging cycle with dry air, we tested the sensor behavior to humidity changes. Figure 4.3 shows results of the measurement, which indicates that the sensitivity towards humidity is $S_{RH} = 3.9$ kHz/%RH.

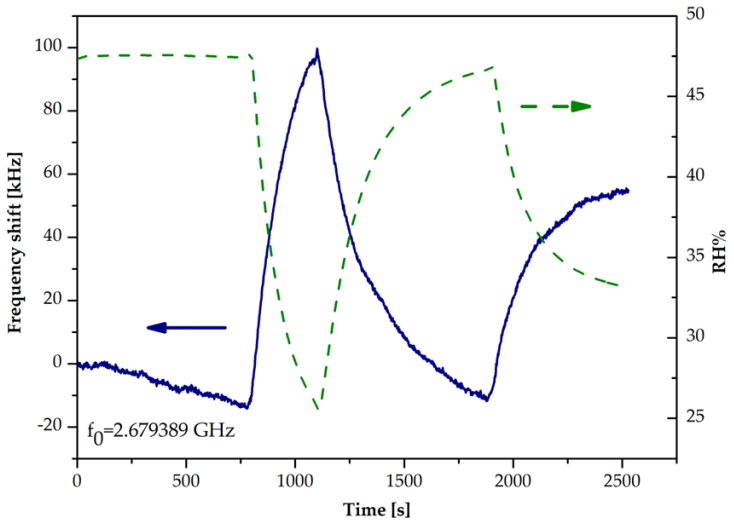

Figure 4.3. Relative humidity dependence of resonant frequency.

The devices were exposed to NO concentrations of 33.3 ppm, using dry air as carrier gas, for 150 s and then cleaned with dry air for 300 s. Figure 4.4(a) shows the response of the sensor for three NO exposure cycles. For each cycle, when the analyte is injected to the chamber, a frequency shift is observed. The average calculated frequency shift is $\Delta f_r \approx 35$ kHz. The observed baseline drift is in part induced by the change in humidity conditions. However, an additional drift was

observed, likely related to the use of dry air as carrier gas [13]. The temperature and humidity conditions observed during the experiment are gathered in Figure 4.4(b). In average, we observe $\Delta T \approx 0.3°C$ and $\Delta(\%RH) \approx 1.4\%$ in each gas exposure cycle. These increments translate to a $\Delta f_r \approx 5.7$ kHz frequency shift. Therefore, a more accurate sensitivity calculation towards NO can be obtained by subtracting this shift to the one observed in fig. 4.4(a). This results in a sensitivity of $S_{NO} = 29.3$ kHz towards 33.3 ppm of NO, which is close to 1 kHz/ppm (0.88 kHz/ppm).

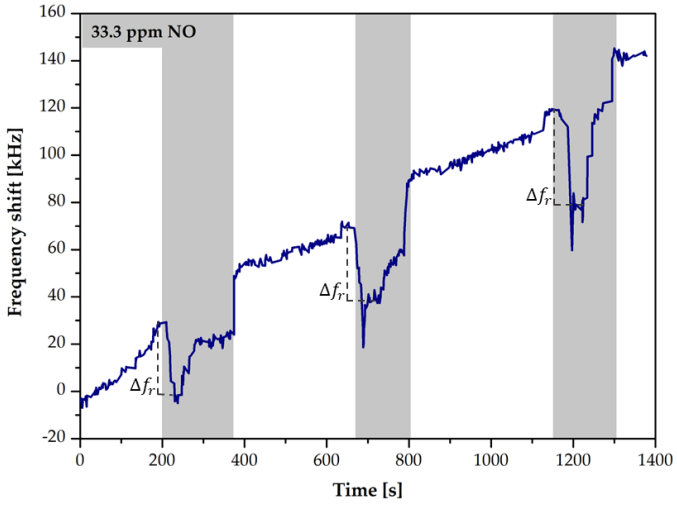

(a)

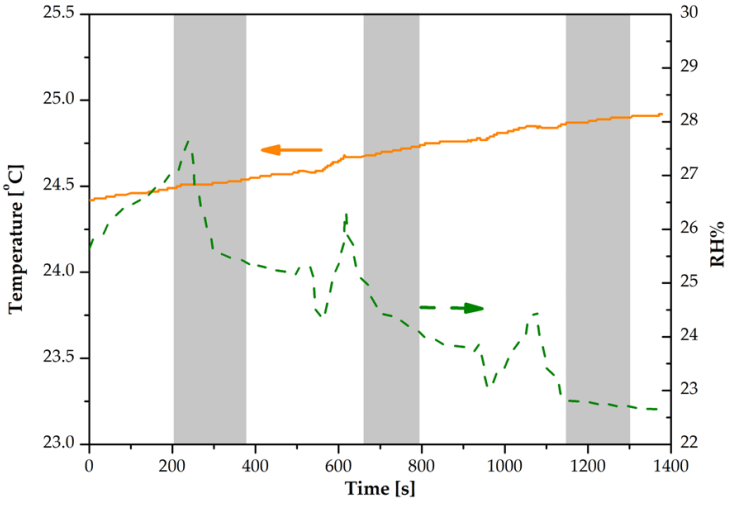

(b)

Figure 4.4. (a) Pentacene functionalized SMR frequency shift upon NO exposure and (b) ambient conditions during the experiment.

These measurements prove that SMR surfaces can be functionalized with evaporated pentacene thin films and be used as gas sensors. The manufactured

devices, as a proof of concept, were tested and their frequency changes were monitored. Despite cross-sensitivity effects especially towards humidity changes, we observed shifts in frequency indicating detection of 33.3 ppm of NO in ambient at room temperature. However, additional detection tests at different analyte concentrations are required to study the linearity of the variation in frequency shift.

4.2. LOW TEMPERATURE

This section covers the experiments carried out in low temperature environments. One of the main issues that come up in this type of atmospheres is humidity presence, therefore SMR devices need to be tested under these conditions first to assure their viability as low temperature sensors. Moreover, the possibility of tracking and discriminating humidity and temperature effects using a dual mode configuration is also explored.

4.1.3. Dual-mode SMR sensor for humidity and temperature discrimination[2]

Electroacoustic resonators are one of the most relevant and well-established devices within the telecommunication industry, as they have become key components in current communication networks [14]. In addition to RF applications, these devices have been found promising as high-resolution sensors for a wide variety of magnitudes and targets [15], such as temperature [16], pressure [17], different gas species [18]–[20] or even biosensing [21]–[23]. However, this versatility can lead to the observation of undesired effects, such as cross-sensitivity or the response changes due to external ambient factors as temperature and/or humidity. Their use as gravimetric sensors relies on the shift experienced by the resonant frequencies when the targeted species are linked to the properly functionalized surface of the resonator.

In this section, detecting and decoupling humidity changes from the evolution of frequency response of a resonator specifically designed to display two resonances at frequencies f_1 and f_2 subjected to temperature and humidity changes is proposed. This behavior could be described with the following equations:

[2] This section is a partial reproduction of J. M. Carmona-Cejas, T. Mirea, R. Hervás-García, J. Olivares and M. Clement, "Dual-mode SMR-based sensor for discriminating temperature humidity effects," *Sensors*, 2024 (under review).

$$\begin{aligned} \Delta f_1 &= TCF_1 \cdot \Delta T + HCF_1 \cdot \Delta(RH) \\ \Delta f_2 &= TCF_2 \cdot \Delta T + HCF_2 \cdot \Delta(RH) \end{aligned} \quad (4.1)$$

where $\Delta f_{1,2}$ are the observed frequency changes, ΔT and $\Delta(RH)$ are the variations in temperature and relative humidity (%) experienced by the devices, and $TCF_{1,2}$, $HCF_{1,2}$ are the temperature and humidity coefficients of frequency, respectively. Therefore, a single resonator in dual mode configuration should allow quantifying humidity and temperature variations through a single measurement and decoupling one from the other.

AlN-based SMRs were manufactured in collaboration with Sorex Sensors Ltd. [24]. The piezoelectric AlN film was sandwiched between two electrodes and grown on top of an acoustic reflector similar to the one used in [25]. This configuration contributed to provide good acoustic insulation. Additionally, a 50 nm-thick Au layer was deposited on top of the devices, to prevent the electrode from oxidating at high humidity concentrations and to prepare the sensor surface for further functionalization.

The fabricated SMRs displayed two longitudinal modes at 1.78 GHz and 2.33 GHz. This phenomenon was achieved by engineering the acoustic reflector, which leaded to two different resonances with different behavior upon temperature variations [26]. Figure 4.5 shows the typical frequency response of a dual mode resonator together with a schematic representation of the device.

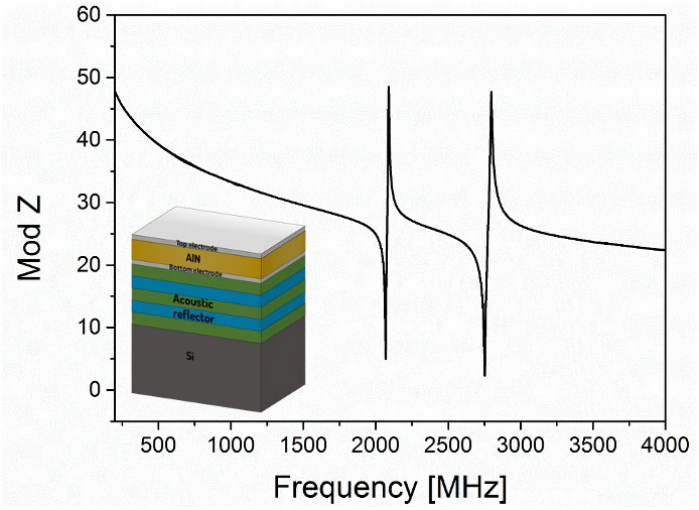

Figure 4.5. Typical frequency response of a dual mode resonator and an illustrative diagram of its layout.

After fabrication the SMRs were bonded to a PCB (to ease the connection to the VNA from inside the testing chamber), and placed on top of the Peltier module,

as can be observed in Figure 4.6. After evacuating the chamber with the rotary pump, the flows of dry and humid air were adjusted with an array of MFCs to set the desired atmosphere in the testing chamber. The characterization was carried out by measuring the S parameters with a portable VNA and sending the data to a computer to process the using our own LabVIEW designed software. The environmental conditions inside the chamber were measured using an NTC and a humidity sensor. A set of measurements at different temperatures and atmospheres was carried out to prove the ability of the resonators to decouple the humidity and temperature contributions to the shift in their resonant frequency.

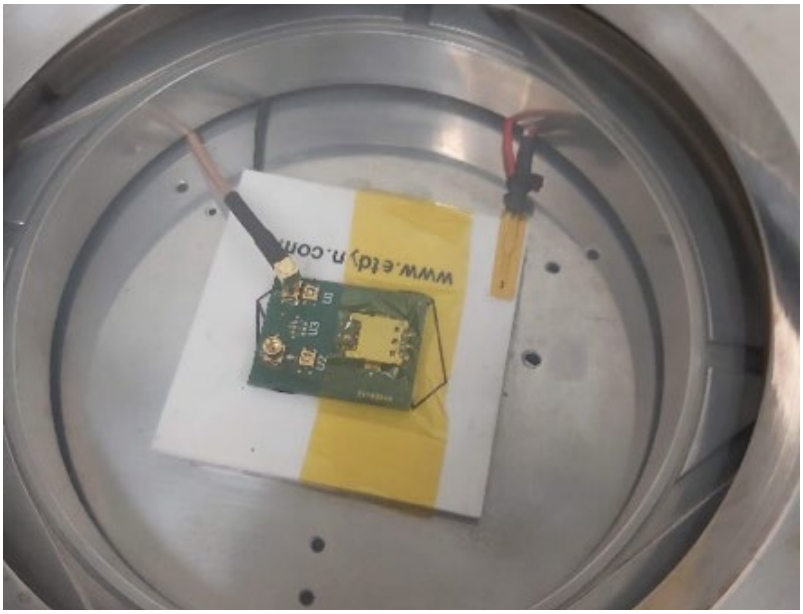

Figure 4.6. View of the inside of the characterization chamber. The SMR is bonded to the PCB and connected to a VNA via an RF cable.

The typical frequency response of the SMRs used for this work is shown in Figure 4.7. Two resonances displaying (slightly) different properties appear separated by around 540 MHz. These peaks experience frequency shifts without interfering with each other over the wide range of temperature and relative humidity envisaged in this work. The first mode has a resonant frequency of $f_r = 1789$ MHz, an electromechanical coupling factor (k_{eff}^2) of about 1.15%, and a resonant quality factor of $Q_r = 371$, giving a figure of merit (FOM) of 426. For the second mode, $f_r = 2332$ MHz, whereas $k_{eff}^2 = 1.1\%$ and $Q_r = 206$, resulting in FOM = 227, indicating that both modes could be well suited for sensing

applications. However, a maximized FOM is not the aim of this device, as we have been focused on the temperature-humidity decoupling phenomenon.

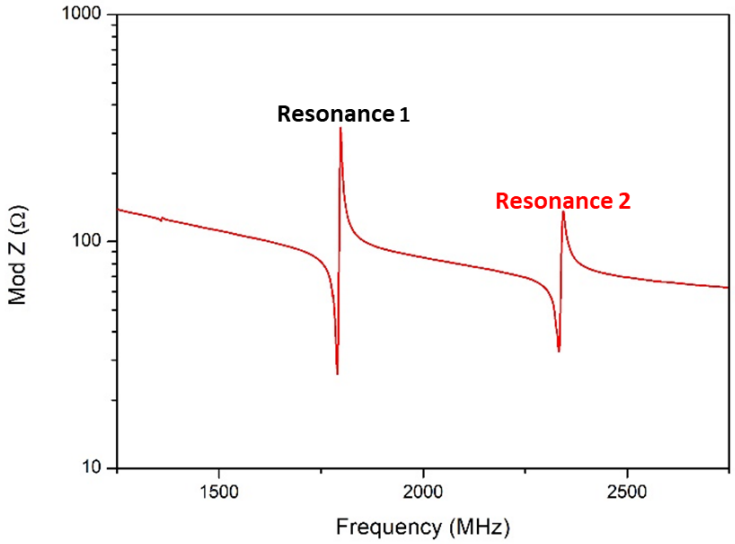

Figure 4.7. Typical frequency response of the SMRs.

The sensitivity of the two modes to temperature and relative humidity changes in the environment can be assessed through the corresponding variation coefficients in terms of frequency:

$$\mathrm{TCF} = \frac{\Delta f}{\Delta \mathrm{T}} \tag{4.2}$$

$$\mathrm{HCF} = \frac{\Delta f}{\Delta \mathrm{RH}} \tag{4.3}$$

where Δf is the shift in resonant frequency, ΔT is the temperature variation, ΔRH is the relative humidity variation and TCF and HCF are the temperature and relative humidity frequency coefficients. These equations can also be normalized to the value of resonant frequency measured at initial time. Prior to operation in any given environment, these coefficients should be experimentally determined in order to have an SMR sensor with a proper calibration. Since our devices display two resonances, we have four coefficients to evaluate: two for each resonant frequency.

TCF measurements were carried out by tracking the resonant frequency of the two modes while performing temperature sweeps at atmospheric pressure under constant humidity conditions. The obtained coefficients were $\mathrm{TCF}_1 = 2.64$ kHz/°C for the first mode and $\mathrm{TCF}_2 = 34.21$ kHz/°C for the second mode. This supposes a variation in almost 32 kHz/°C between the two coefficients, being the

second mode much more sensitive to temperature changes than the first one, which displays a low variation coefficient.

Once the TCF determined, the resonators were subjected to relative humidity changes in the 20% to 60% range. During these experiments the temperature was also tracked since slight temperature changes could take place. The typical frequency shift of the two modes is shown in Figure 4.8. Both modes experience different shifts, although this can be explained by the small temperature changes undergone during data acquisition, as it can be seen from the temperature variation measured and displayed on the right axis. Since the two modes behave differently under temperature changes, both frequencies experience different variations after each iteration. This also explains why after each sensing iteration both modes seem to move upwards in frequency.

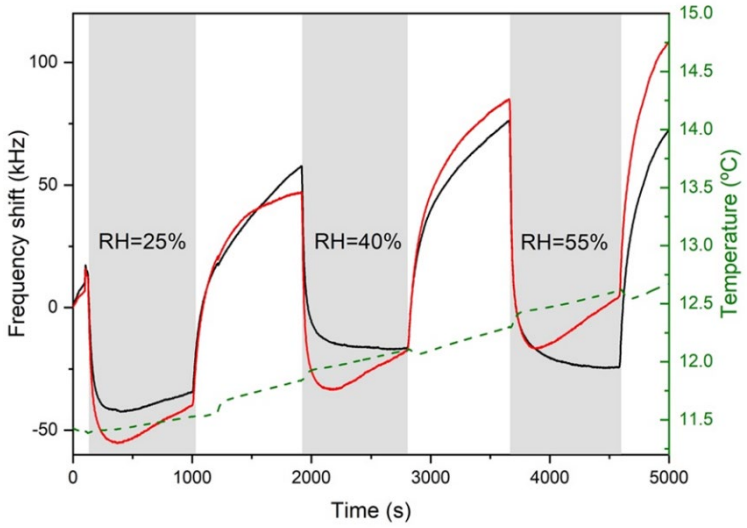

Figure 4.8. Frequency shift under different relative humidity atmospheres for resonance 1 (black) and resonance 2 (red). Temperature monitorization is displayed on the right axis.

Figure 4.9(a) shows the frequency response of the two modes for the same relative humidity variation taken at room temperature and at low temperature environments. The temperature changes during each measurement are also different, being the low temperature experiment the one with higher temperature variation from start to finish, as it can be extracted from the higher difference between the two resonances. After applying a temperature-related correction, the two modes seem to behave more similarly under the two different temperature environments, as suggested by Figure 4.9(b). This correction is no more than subtracting the frequency shift related to the temperature change during data acquisition and leaving just the humidity-related changes:

$$\Delta f_{RH} = \Delta f_{\text{Total}} - \text{TCF}\cdot\Delta T \qquad (4.4)$$

This approach works in the same manner for resonance 1 and resonance 2 using their calculated TCFs. With the resulting frequency shifts we can deduce the humidity coefficients for the two resonances. This calibration process is gathered in Figure 4.10, where variations from 0 to ~65% are represented for the two resonances together with their linear regression fits. Calculated HCF values are $\text{HCF}_1 = -1.94 \pm 0.09\ \text{kHz/(\%RH)}$ with a correlation coefficient $R^2 = 0.99$ for resonance 1 and $\text{HCF}_2 = -1.62 \pm 0.08\ \text{kHz/(\%RH)}$ and $R^2 = 0.98$ for resonance 2. The variation between them, which in this case is of around 0.32 kHz/(%RH), can be neglected after considering the variation between temperature coefficients and thus implying a very similar sensitivity to humidity changes from both modes.

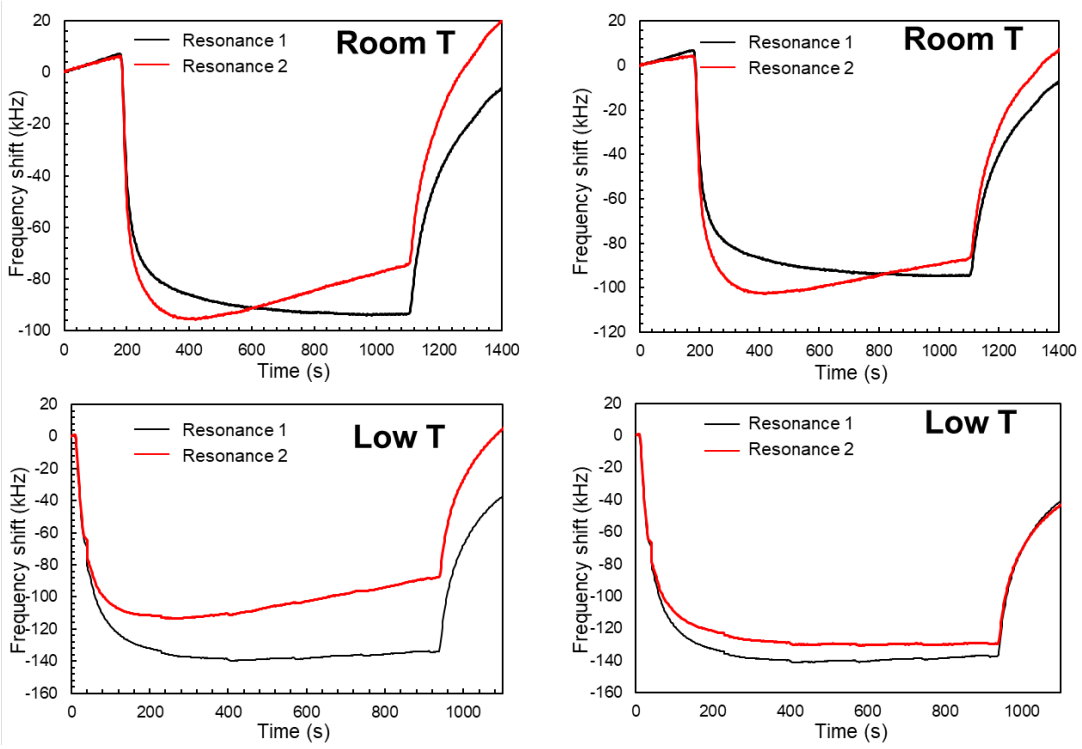

Figure 4.9. (a) Frequency shifts for a relative humidity variation of ~50% taken at room temperature and at low temperature (~ − 2 °C), respectively, without keeping temperature constant; (b) same measurements after subtracting the temperature variation contribution to the frequency shifts.

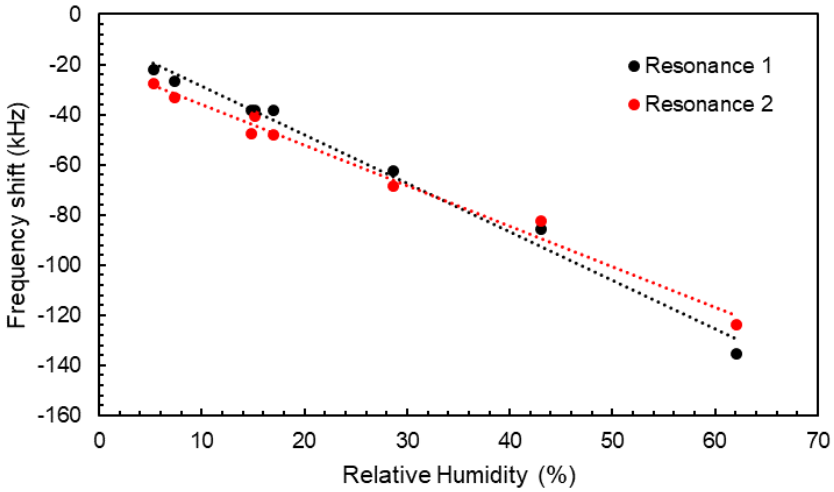

Figure 4.10. HCF measurements for resonance 1 and resonance 2 within the range between 0 and ~65% RH together with their linear regression fits. The error bars represent the standard error of the fit.

As HCF_1 and HCF_2 are similar to each other, we can decouple the influence of relative humidity from the response of the resonator taking advantage of this phenomena. So, starting from eq. 4.1 and assuming HCF_1=HCF_2 we get the following equation:

$$\Delta T = \frac{\Delta f_2 - \Delta f_1}{\mathrm{TCF}_2 - \mathrm{TCF}_1} \tag{4.5}$$

which gives us a linear dependence between the temperature variations and the difference of frequency shifts between the two modes.

Figure 4.11 shows a series of measurements where temperature variations were recorded while the experimental conditions were set between 13 and 17.5°C. The plotted frequency shifts represent the differences in resonant frequency between resonance 1 and resonance 2. Additionally, arbitrary relative humidity concentrations between 0 and ~65% were injected to the testing chamber to force humidity-related frequency shifts to the two modes. Good linear dependence is observed between the frequency and temperature variations despite the variation in humidity atmospheres, leaving a linear regression parameter $a = 0.02783 \pm 0.0011$°C/kHz with a regression correlation coefficient $R^2 = 0.99$. The calculated slope of this dependence from the TCF measured values would be $(\mathrm{TCF}_2 - \mathrm{TCF}_1)^{-1} = 0.0317$ °C/kHz, which would lead to a difference of just 0.0039 °C/kHz, proving a good agreement between the derived expression and the experimental results is found. The same experiment was carried out at a larger range of

temperatures, going from 17 to −18°C and applying different humidity concentrations, too. The results are gathered in Figure 4.12 together with their linear fit. In this case, the regression parameter is $a = 0.0331 \pm 0.0022$ °C/kHz with a correlation coefficient $R^2 = 0.99$. This parameter differs with the calculation from the TCF in 0.0014 °C/kHz. The good correlation found in this case proves that this relation is independent from the temperature range and the humidity conditions in where the device is operating.

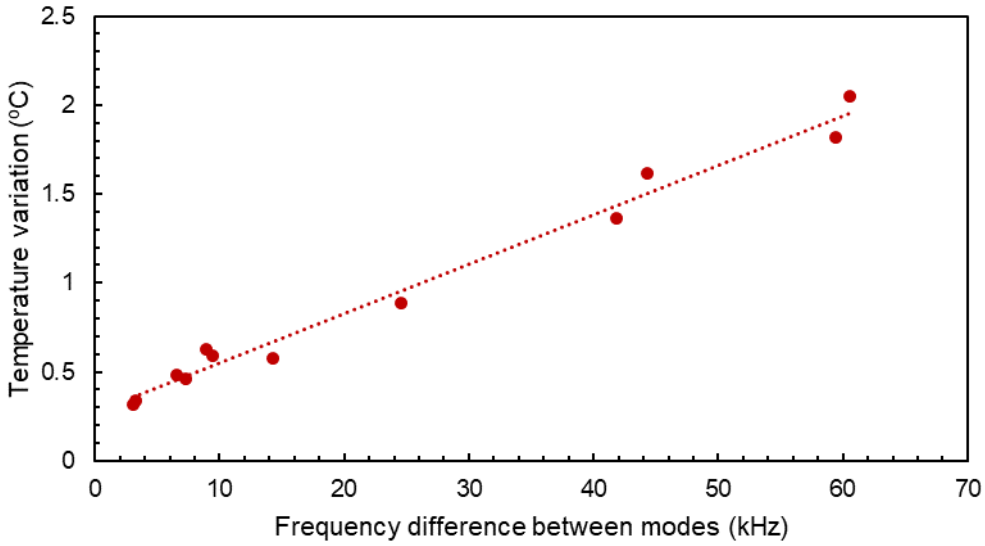

Figure 4.11. Difference in resonant frequency shift between resonance 1 and 2 for different temperature variations in the 11.5 to 13 °C under arbitrary relative humidity concentrations.

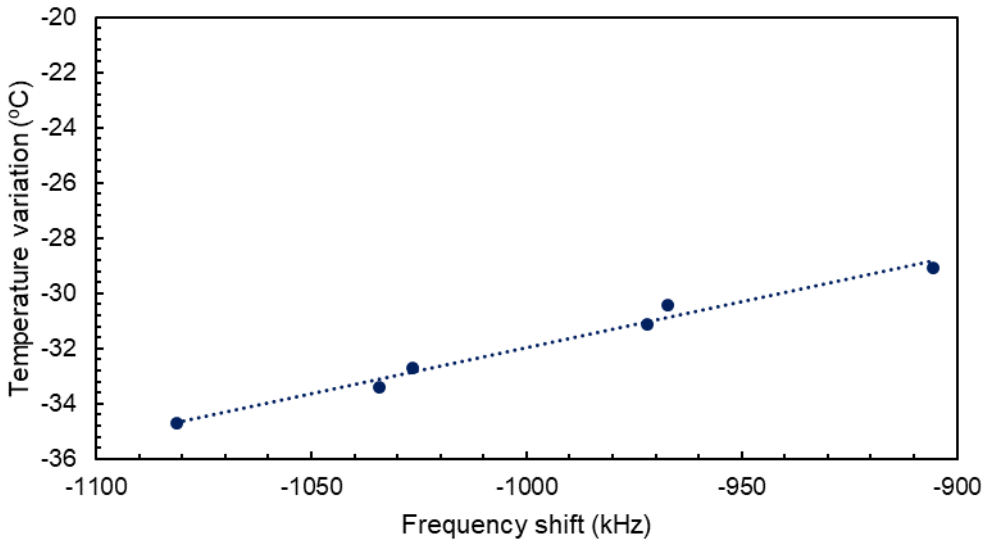

Figure 4.12. Difference in resonant frequency shift between resonance 1 and 2 for different temperature variations in the 17 to −18 °C range under arbitrary relative humidity concentrations.

Since different humidity variations at different temperatures imply different water concentration in atmosphere, finding a similar behavior at room temperature and lower temperatures for different humidity conditions suggest that the frequency variations measured for the two resonances are linked to this relative humidity changes and not only to the absolute concentration of water in the air. This behavior has also been reported for higher temperatures in [27], where the detection mechanism is not entirely gravimetric but based on the Young's modulus variation of the sensing layer. For a gravimetric detection process with negative frequency shifts upon humidity exposure, a similar response for a higher temperature range is reported in [28].

To summarize, the frequency response to both temperature and humidity changes was evaluated and calibrated for a dual mode SMR sensor. Since the two modes react in the same way to relative humidity changes, one can decouple this effect from the sensor response from other potential target magnitudes, as it was demonstrated with temperature changes. This behavior was proven at room temperature and under a below 0°C environment, demonstrating that the two modes are indeed sensitive to relative humidity changes and not purely to water concentration changes in air. This also opens the possibility of just needing a humidity calibration at any given temperature to work in any desired temperature conditions.

As a potential application, the proven behavior of the SMRs in this work suggest that a single SMR could be enough to be used as a gravimetric sensor after decoupling both temperature and humidity effects from its frequency response.

4.3. HIGH TEMPERATURE

After testing the behavior of AlN-based SMRs at high temperatures and proving they offer a sustainable performance [29], the devices were ready to be functionalized through a non-harming process. This section covers the experiments conducted to assess the performance of functionalized AlN-based SMR sensors operating at high temperature. In this case, the devices were functionalized with WO_3 thin films. Metal oxides have been widely studied as active layers for chemiresistive sensors. In particular, WO_3 films offer great sensitivity and high selectivity towards oxidizing gases such as NO and NO_2 [30], [31]. Moreover, sensors based on metal oxide thin films usually need high operation temperatures ($T_{op} > 150°C$). These two

properties can be exploited to fabricate a NO sensor with the ability to operate at high temperatures, which falls within the scope of one of the main objectives stated at the beginning of the thesis.

4.1.4. AlN-based SMRs functionalized with WO_3 films for nitric oxide detection[3]

4.1.4.1. Frequency response of the SMR

The electrical response of AlN-based SMR sensors functionalized with WO_3 thin films described in previous chapter was characterized. The corresponding modulus of impedance, together with a top view of the sensor, are shown in Figure 4.13.

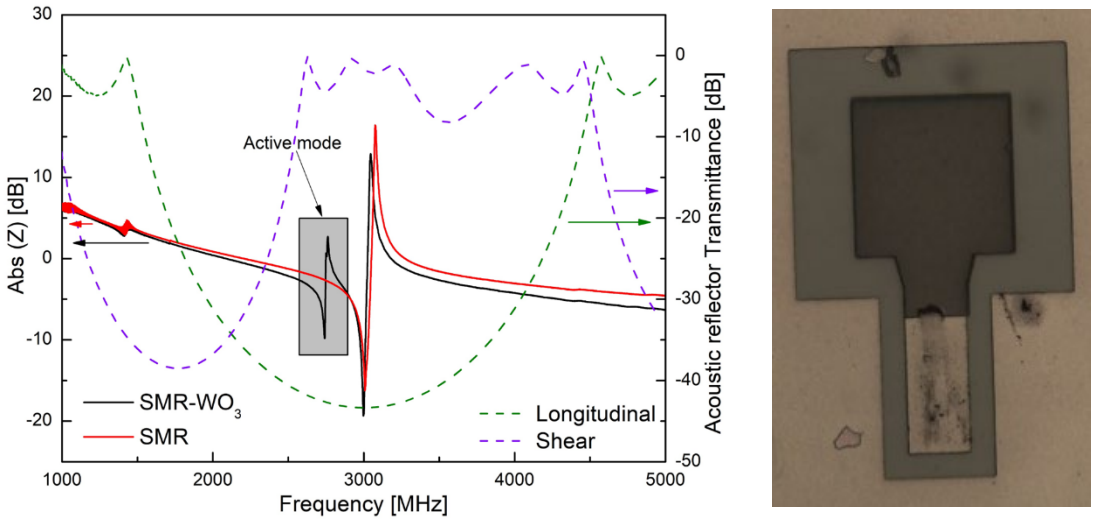

(a) (b)

Figure 4.13. (a) SMR response at room temperature and air before and after the deposition of WO_3 layer (solid lines) and transmittance of the acoustic reflector (dashed lines). (b) Optical microscope picture of the top electrode used to capacitively excite the SMRs displaying the WO_3 covered and uncovered areas.

Results from Figure 4.13 reveal that the addition of the patterned WO_3 layer significatively affected the performance of the resonator performance. Specifically,

[3] This section is a partial reproduction of J. M. Carmona-Cejas, T. Mirea, J. Olivares, R. Hervás-García and M. Clement, "AlN-based Solid Mounted Resonators functionalized with WO3 films for NO detection," *Sens. and Actuators B: Chem.*, 2024 (under review).

the longitudinal mode of the original uncovered resonator splits into two modes after the addition of the WO_3 layer. Mode 1 remains close to the initial resonant frequency, representing the resonator defined by the uncovered portion of the top electrode. Meanwhile, Mode 2 appears at lower frequencies, corresponding to the WO_3/AlN-SMR stack [32]. The shift to lower frequencies of mode 2 is proportional to the thickness (or weight) of the WO_3 layer. This mode, which we will hereinafter refer to as "active mode", is crucial for sensing. It is worth noting that the two modes fall within the region of lowest transmittance for longitudinal modes generated by the Mo/SiO_2 acoustic reflector, ensuring effective acoustic insulation. It is also interesting to highlight that Mode 1, representing the unaltered SMR, was not sensitive to the analyte studied in this work but could be influenced by ambient factors such as temperature and humidity. Conversely, Mode 2 (the active mode), appeared to be highly responsive to the analyte and provided the sensor response during each exposure cycle by displaying changes in both resonant and anti-resonant frequencies. For all the devices manufactured, the modes of the unmodified SMRs were located approximately at 3 GHz, whereas the WO_3-SMR active modes were positioned in the range of 2.1 to 2.7 GHz region, depending on the thickness of the WO_3 layer.

An essential part of the characterization of the resonators was to verify whether, after the heat treatment they undergo to enhance the crystallinity of the WO_3 layer, the resonators remained suitable for use as sensors. A critical criterion for resonator viability as a sensor is the maintenance of a reasonable Q factor, indicative of its ability to preserve energy within the piezoelectric capacitor. The Q factor of the resonators was deduced from the frequency response through [33]:

$$Q_{r,a} = \frac{f_{r,a}}{2}\left(\frac{d\phi(Z)}{df}\right)_{f_{r,a}} \tag{4.6}$$

where $f_{r,a}$ are the resonant and anti-resonant frequency values and $\phi(Z)$ is the phase of the impedance. The Q factors for the NO-active modes exhibited values within the 100 to 270 range, for both resonant and anti-resonant frequencies. This indicates that the resonators maintained sufficiently high Q-factors for sensor applications. Previous research on the high temperature performance of SMRs similar to those employed in this study [34] indicate that the annealing temperature remained well below the threshold from which the resonance is significantly degraded. To illustrate mode behavior under high temperature operation, Figure 4.14 shows anti-resonant frequency measurements at room temperature, 200 °C

and 300 °C. As evident, the response of the resonators degrades as operation temperature increases, although still hold good Q values that allow for gas detection experiments.

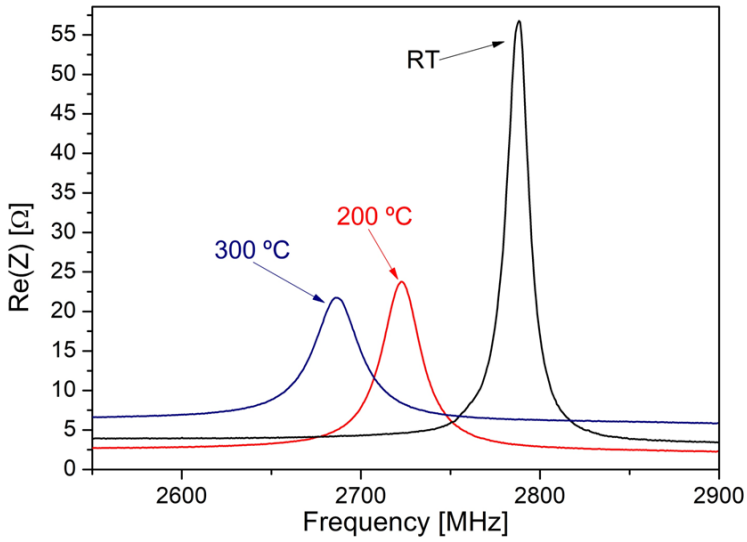

Figure 4.14. Anti-resonant frequency measured at room temperature (black), at 200 °C (red) and at 300 °C (blue).

Another important aspect of the resonator characterization involved evaluating the impact ambient factors, specifically temperature. The TCFs of the different resonant modes, defined as:

$$\mathrm{TCF}_{r,a} = \frac{\Delta f_{r,a}}{\Delta T} \tag{4.7}$$

were obtained by measuring the frequency response with the previously described experimental setup under ambient temperatures ranging from 20 °C and 100 ºC. The TCFs for the unaltered SMR modes always stayed in the −35 kHz/°C range, for both resonant and antiresonant frequencies. As for the WO_3-SMR active modes, they showed a dependence on the thickness of the sensing layer. Specifically, for the 190 nm WO_3 layers, the TCF values were -62 kHz/°C and -67 kHz/°C for resonant and anti-resonant frequencies, respectively. For the 330 nm WO_3 layers, the corresponding TCF values increased to -128 kHz/°C and -134 kHz/°C for resonant and anti-resonant frequencies, respectively.

4.1.4.2. NO detection experiments

The performance of the SMR-sensors was evaluated using a custom-designed and constructed setup. A schematic of the design is illustrated in Chapter 2. The devices were placed inside the test chamber, and the gas flow maintained at 700 sccm throughout process. The heating system was then activated to achieve the desired operating temperature, and the sensor was allowed to stabilize overnight under these conditions to ensure a consistent frequency response during measurements. Subsequently, the sensor performance was assessed through cycles of NO gas exposure lasting approximately 20 minutes using dry air as carrier gas, followed by 20 minutes of pure dry air flow to purge the atmosphere of the analyte. These cycles were repeated at least three times for each device for every operating temperature.

The performance of the sensors was evaluated at 200 °C, 250 °C and 300 °C. Two of the sensors also showed good sensitivity at 350 °C (H-1 and Tilted-3). The rest of the sensors did not show sensitivity at 350 °C due to frequency modes becoming too deteriorated. The temperature range used is within the already proven range of optimum sensitivity of metal oxide functionalization layers [30]. All the measurements were conducted using 50 ppm NO exposure cycles diluted in dry air. A typical sensor response is shown in Figure 4.15.

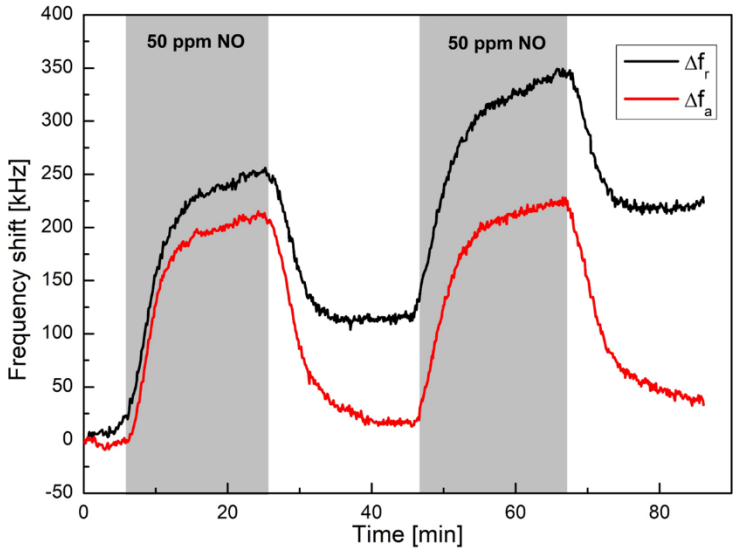

Figure 4.15. Transient response of the WO_3-SMR sensor (H-1) upon two 50 ppm NO exposure cycles at 250 °C for resonant (black) and anti-resonant (red) frequencies.

Both resonant and anti-resonant frequency experience a strong response to NO exposure. However, recovering baseline values proved challenging, due to a

linear increase of frequency over time alongside the NO response, which had a more pronounced impact on the resonant frequency. Apparently, this frequency drift could not be attributed to a temperature decrease, as the temperature was maintained constant via PID control. Moreover, the different drifts experienced by the two modes cannot be justified by their corresponding TCF values determined previously. Nevertheless, since the drift is linear over time it barely affects the calculation of the sensors' sensitivities.

To explore the detection limit of the sensors, detection experiments were carried out at decreasing NO concentrations of 25, 15 and 5 ppm. All exposure cycles were carried out at 200 °C, temperature that proved maximum sensitivity within the measurement range. As shown in Figure 4.16, significant detection capability was observed across all cases; the observed shifts suggest that lower even concentrations, conserving linearity, could be effectively detected. The observed response and recovery times are consistent for resonant and anti-resonant frequencies and fall within the same ranges as those reported in the literature for WO_3-based chemiresistive NO_x sensors [35]. These times range from 12-16 min at 200 °C to 4-8 min at 300 °C, indicating that temperature accelerates the adsorption/desorption process of the NO molecules on WO_3 surface.

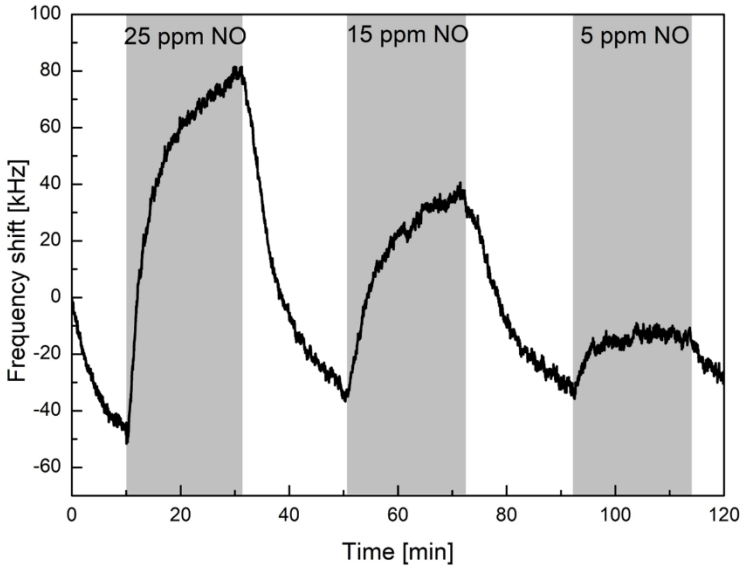

Figure 4.16. Transient response of the WO_3-SMR sensor (H-1) upon 25 ppm, 15 ppm and 5 ppm NO exposure cycles at 200°C for anti-resonant frequency shift.

The sensitivity of the sensors, defined as the ratio of the frequency shift experienced by the resonant or anti-resonant frequency to the NO concentration, through the equation:

$$S_{r,a} = \frac{\Delta f_{r,a}}{[\mathrm{NO}]}. \tag{4.8}$$

was determined for all the operation temperatures. The corresponding results are depicted in Figure 4.17. As evident, the sensitivities to NO for both resonant and anti-resonant frequencies are very similar in each instance. If the sensitivities and TCF values are known, a simultaneous measurement of the resonant and anti-resonant frequencies can provide analyte concentrations while decoupling temperature effects, as reported in [36]. The highest sensitivity was achieved with H-1 sensor operating at 200 °C, with a nearly 300 kHz shift for 50 ppm value, resulting on 5.32 kHz/ppm shift for the resonant frequency and a 5.48 kHz/ppm shift for the anti-resonant frequency. However, its performance degraded at higher temperatures, yielding sensitivity values of 3.62 kHz/ppm and 3.87 kHz/ppm at 250 °C, 1.22 kHz/ppm and 1.20 kHz/ppm at 300 °C, and 1.14 kHz/ppm and 1.49 kHz/ppm at 350 °C. The Tilted-3 sensor, although initially showing lower sensitivity at 200 °C (3.51 kHz/ppm and 3.36 kHz/ppm), offered the best performance at high temperature, with a sensitivity of 1.5 kHz/ppm at 350 °C. Other evaluated sensors, while demonstrating good response to the analyte, specially at 200 °C, showed poorer sensitivities compared to the aforementioned sensors. The superior performance observed in the H-1 sensors, despite displaying the lower surface roughness, could be attributed to the 50% O_2 partial pressure used during sputtering process, which has been reported to be optimal for enhancing sensing behavior [37]. Another possible cause could be the thickness of the sensing layers, as thicknesses below 200 nm and above 250 nm provide a reduced response compared to the obtained in the H-1 sensors, corresponding to 220 nm. No significant variation in sensitivity was observed between the tilted non-tilted WO_3.

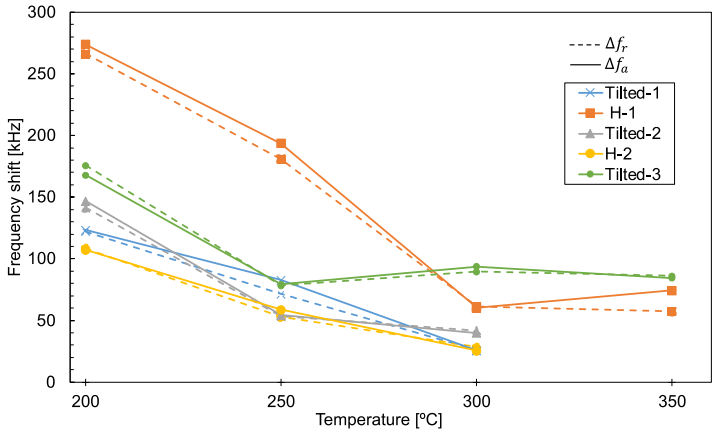

Figure 4.17. Sensitivities towards 50 ppm of NO for the studied sensors at the different operating temperatures for resonant (dashed lines) and anti-resonant (solid lines) frequencies. The lines are plotted to guide the eye.

In all scenarios the sensors' response decreased with increasing temperature. This trend can be attributed to the higher rate of oxygen adsorption on the WO_3 surface at higher temperatures [38]. Since the sensing mechanism relies on analyte adsorption at oxygen vacancy sites [39], if O_2 molecules dissociate in these sites, NO molecules must compete with them, potentially resulting in a weaker overall sensor response. However, at higher temperatures, the response and recovery times enhanced, indicating that the higher kinetic energy of NO molecules helped to speed up the adsorption/desorption process. Furthermore, increasing the operation temperature produced some degradation of the resonators' performance, with significant lowering of the Q factors in some cases. Since the Q factors are closely related to the limit of detection of the sensor, this could explain why some sensors failed to detect at 350 °C.

Contrary to the typical behavior observed in BAW/SAW gravimetric sensors, the adsorption of NO molecules resulted in a positive frequency shift for both resonant and anti-resonant frequencies across all the sensors examined. This indicates that following NO exposure, the frequencies tended to rise relative to the baseline frequency. It is known that when NO_x molecules adsorb onto WO_3 surfaces, the electrical resistance of the films increases due to oxidation, contrary to what happens when they are exposed to reducing gases [30]. Furthermore, this oxidation process can induce alterations in the elastic properties of the sensing layer [40]. In this case, following NO adsorption, the acoustic velocity of the longitudinal mode experiences an increase. As resonant frequency is directly proportional to the acoustic velocity [15], a positive shift in acoustic velocity would consequently lead to a positive shift in frequency. In this case, this shift would be greater than the negative shift induced by mass incorporation. This effect has been already reported in SAW devices [13], [41] and in FBAR-based sensors [42]. Figure 4.18 shows a simulation using Mason's model to investigate the influence of variations in the acoustic velocity of the WO_3 on the resonant frequency of the devices. The SMR configuration corresponded to that of the devices fabricated for this study. The WO_3 material properties were taken from [43]. As evident in Figure 4.18, the frequency shift is clearly influenced by the acoustic velocity and significantly increases with the thickness of the WO_3 layer. It is evident that for thicknesses of 100 nm or less, a change in acoustic velocity and, therefore, in stiffness, does not lead to an appreciable shift in frequency. However, for thicknesses ranging from 200 to 300 nm, the effect becomes more pronounced and a remarkable shift in frequency is induced.

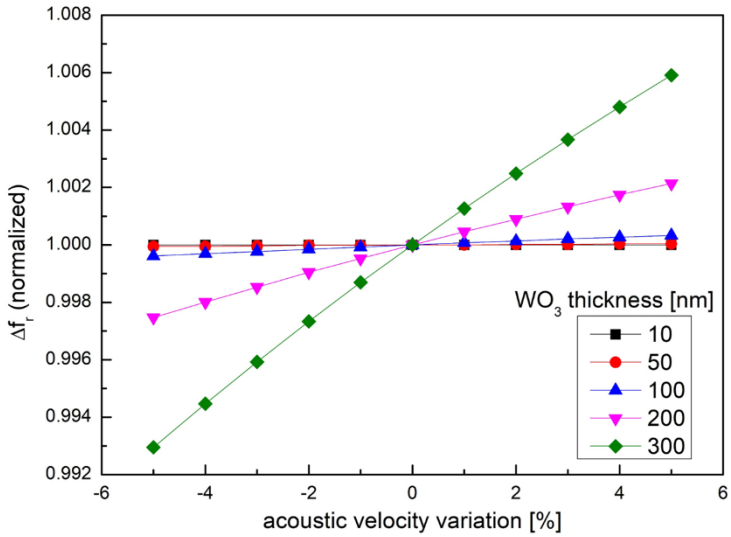

Figure 4.18. Frequency shifts due to longitudinal acoustic velocity changes for different WO_3 film thicknesses using Mason's model simulations.

AlN-based piezoelectric resonators were fabricated on Mo/SiO_2 acoustic reflectors to operate in the 2-3 GHz range. These resonators were tested as a potential transduction method for NO gas sensors. The full sensor consisted of dc pulsed sputtered WO_3 thin films integrated on the top electrode of the resonators, leaving part of it uncoated to allow electrical contact. Two different $Ar:O_2$ gas mixtures were used during sputtering process. After all the fabrication steps, a 12 hour, 350 °C annealing process in air was performed to improve crystalline quality of the WO_3 films.

From material characterization techniques, Raman spectra showed that WO_3 films were practically amorphous before annealing and presented a monoclinic structure after, with rather improved crystalline quality. The films also presented relatively large surface roughness and great dispersion in grain size values, indicating good surface ratio. The electrical characterization showed that the resonance modes generated after integrating the sensing layers had good enough Q factors to perform as sensors even after the annealing process.

To test the performance of the WO_3-SMR sensors, 50 ppm NO exposure cycles were carried out for all the fabricated devices at 200, 250 and 300 °C. They all showed great sensitivity, higher than 1 kHz/ppm in most of the cases, and two of them also showed good performance at 350 °C. The highest sensitivity measured was 5.32 kHz/ppm and 5.48 kHz/ppm for a device with 220 nm WO_3 layer at 200 °C, meaning that sub-ppm levels of detection could be achieved. However, frequency

drifts during sensing performance measurements were almost unavoidable in many cases and thus further research needs to be carried out on that. Moreover, an improvement in Q factor values for the WO_3-SMR modes would lead to higher resolution and lower limits of detection.

References

[1] T. Mirea, "Thin film electroacoustic resonators for physical and chemical sensing," Ph.D. dissertation, Electronic Engineering Department, Universidad Politécnica de Madrid, 2017. doi: 10.20868/UPM.thesis.45713.

[2] M. de Miguel Ramos, "High sensitivity biosensors based on shear mode AIN resonators for in liquid operation," Ph.D. dissertation, Electronic Engineering Department, Universidad Politécnica de Madrid, 2015. doi: 10.20868/UPM.thesis.39314.

[3] X. Zhuang, S. Han, B. Huai, W. Shi, and Y. Junsheng, "Sub-ppm and high response organic thin-film transistor NO_2 sensor based on nanofibrillar structured TIPS-pentacene," *Sens. Actuators B Chem.*, vol. 279, pp. 238–244, Jan. 2019, doi: 10.1016/j.snb.2018.10.002.

[4] W. Shi, J. Yu, and H. E. Katz, "Sensitive and selective pentacene-guanine field-effect transistor sensing of nitrogen dioxide and interferent vapor analytes," *Sens. Actuators B Chem.*, vol. 254, pp. 940–948, Jan. 2018, doi: 10.1016/j.snb.2017.07.198.

[5] T. Mirea, J. Olivares, M. Yañez-Mó, M. Valés-Gómez, and E. Iborra, "First Steps Towards Simultaneous Isolation and Detection of Exosomes with Carbon Nanotube-Based SMRs," *IEEE Intern. Ultrason. Symp., IUS*, vol. 2018-Janua, pp. 1–4, 2018, doi: 10.1109/ULTSYM.2018.8579718.

[6] T. Mirea, J. Olivares, M. Clement, J. Sangrador, and E. Iborra, "Direct integration of CNT forests on solidly mounted resonators and their influence on device performance," *2017 Joint Conf. of the European Freq. and Time Forum and IEEE Intern. Freq. Control Symp., EFTF/IFC 2017 - Proceedings*, pp. 353–356, 2017, doi: 10.1109/FCS.2017.8088890.

[7] T. Mirea *et al.*, "Carbon nanotube growth on piezoelectric AlN films: Influence of catalyst underlayers," *RSC Adv.*, vol. 5, no. 98, pp. 80682–80687, 2015, doi: 10.1039/c5ra16840f.

[8] A. Firouzi, S. Sobri, F. M. Yasin, and F. Ahmadun, "Synthesis of Carbon Nanotubes by Chemical Vapor Deposition and their Application for CO_2 and CH4 Detection," *Intern. Conf. on Nanotech. and Biosensors*, vol. 2, no. January 2015, pp. 169–172, 2010.

[9] S. Fatemi, M. Vesali-Naseh, M. Cyrus, and J. Hashemi, "Improving CO_2/CH_4 adsorptive selectivity of carbon nanotubes by functionalization with

nitrogen-containing groups," *Chem. Engineering Res. and Design*, vol. 89, no. 9, pp. 1669–1675, 2011, doi: 10.1016/j.cherd.2010.10.002.

[10] J. Xiang, A. Singhal, R. Divan, L. Stan, Y. Liu, and I. Paprotny, "Selective volatile organic compound gas sensor based on carbon nanotubes functionalized with ZnO nanoparticles," *J. of Vacuum Sci. & Tech. B*, vol. 39, no. 4, p. 042803, Jul. 2021, doi: 10.1116/6.0000992.

[11] H. U. Khan, M. E. Roberts, W. Knoll, and Z. Bao, "Pentacene based organic thin film transistors as the transducer for biochemical sensing in aqueous media," *Chem. of Mater.*, vol. 23, no. 7, pp. 1946–1953, Apr. 2011, doi: 10.1021/cm103685c.

[12] H. Klauk, D. J. Gundlach, J. A. Nichols, and T. N. Jackson, "Pentacene organic thin-film transistors for circuit and display applications," *IEEE Trans. Electron. Devices*, vol. 46, no. 6, pp. 1258–1263, 1999, doi: 10.1109/16.766895.

[13] S. H. Wang, C. Y. Shen, Z. J. Lien, and J. H. Wang, "Nitric oxide sensing properties of a surface acoustic wave sensor with copper-ion-doped polyaniline/tungsten oxide nanocomposite film," *Sens. Actuators B Chem.*, vol. 243, pp. 1075–1082, May 2017, doi: 10.1016/J.SNB.2016.12.101.

[14] K. Hashimoto, *RF Bulk Acoustic Wave Filters for Communications*. Artech House, 2009.

[15] D. Ballantine Jr. ;Robert White; S. Martin; Antonio Ricco; E. Zellers; G. Frye; H. Wohltjen, *Acoustic Wave Sensors*. Academic Press Inc., 1996.

[16] S. Zhgoon *et al.*, "SAW temperature sensor on Quartz," *IEEE Trans. Ultrason. Ferroelectr. Freq. Control*, vol. 62, no. 6, pp. 1066–1075, Jun. 2015, doi: 10.1109/TUFFC.2014.006840.

[17] C. Gu *et al.*, "Temperature calibrated on-chip dual-mode film bulk acoustic resonator pressure sensor with a sealed back-trench cavity," *J. of Micromech. and Microengineering*, vol. 28, no. 7, p. 075010, Apr. 2018, doi: 10.1088/1361-6439/AAB935.

[18] C. Lim, W. Wang, S. Yang, and K. Lee, "Development of SAW-based multi-gas sensor for simultaneous detection of CO_2 and NO_2," in *Sens. and Actuators, B Chem.*, Elsevier, May 2011, pp. 9–16. doi: 10.1016/j.snb.2010.02.057.

[19] X. Wang, F. Cui, J. Lin, B. Ding, J. Yu, and S. S. Al-Deyab, "Functionalized nanoporous TiO_2 fibers on quartz crystal microbalance platform for

formaldehyde sensor," *Sens. Actuators B Chem.*, vol. 171–172, pp. 658–665, Aug. 2012, doi: 10.1016/j.snb.2012.05.050.

[20] D. Chen, J. J. Wang, D. H. Li, and Y. Xu, "Hydrogen sensor based on Pd-functionalized film bulk acoustic resonator," *Sens. and Actuators, B: Chem.*, vol. 159, no. 1. pp. 234–237, 2011. doi: 10.1016/j.snb.2011.06.078.

[21] C. Han *et al.*, "Solidly mounted resonator sensor for biomolecule detections," *RSC Adv.*, vol. 9, no. 37, pp. 21323–21328, Jul. 2019, doi: 10.1039/C9RA01695C.

[22] Y. Zhang, J. Luo, A. J. Flewitt, Z. Cai, and X. Zhao, "Film bulk acoustic resonators (FBARs) as biosensors: A review," *Biosens. and Bioelectron.*, vol. 116, pp. 1–15, Sep. 30, 2018. doi: 10.1016/j.bios.2018.05.028.

[23] J. Weber *et al.*, "Shear mode FBARs as highly sensitive liquid biosensors," *Sens. Actuators A Phys.*, vol. 128, no. 1, pp. 84–88, 2006, doi: 10.1016/j.sna.2006.01.005.

[24] "Sorex Sensors, Ltd." Accessed: May 04, 2023. [Online]. Available: www.sorexsensors.com

[25] T. Mirea, N. Chiodarelli, M. Moreno, and M. Demiguel-Ramos, "Portable Network Analyzers For Full Characterization of FBAR Sensors: Influence of Readout Parameters On Sensor Performance," *2021 Joint Conf. of the European Freq. and Time Forum and IEEE Intern. Freq. Control Symp., EFTF/IFCS 2021 - Proceedings*, 2021, doi: 10.1109/EFTF/IFCS52194.2021.9604278.

[26] L. García-Gancedo *et al.*, "Dual-mode thin film bulk acoustic wave resonators for parallel sensing of temperature and mass loading," *Biosens. Bioelectron.*, vol. 38, no. 1, pp. 369–374, Oct. 2012, doi: 10.1016/j.bios.2012.06.023.

[27] J. Liu, Z. Zhao, Z. Fang, Z. Liu, Y. Zhu, and L. Du, "High-performance FBAR humidity sensor based on the PI film as the multifunctional layer," *Sens. Actuators B Chem.*, vol. 308, p. 127694, Apr. 2020, doi: 10.1016/j.snb.2020.127694.

[28] W. Xuan *et al.*, "A film bulk acoustic resonator oscillator based humidity sensor with graphene oxide as the sensitive layer," *J. of Micromech. and Microengineering*, vol. 27, no. 5, p. 055017, Apr. 2017, doi: 10.1088/1361-6439/AA654E.

[29] T. Mirea, J. Olivares, M. Clement and J. Sangrador, “AlN-based solidly mounted resonators at 400°C: In-situ performance monitoring,” *IEEE Intern. Ultras. Symp., IUS*, 1700–1702, Oct. 2019 https://doi.org/10.1109/ULTSYM.2019.8925697.

[30] B. Urasinska-Wojcik, T. A. Vincent, M. F. Chowdhury, and J. W. Gardner, “Ultrasensitive WO_3 gas sensors for NO_2 detection in air and low oxygen environment,” *Sens. Actuators B Chem.*, vol. 239, pp. 1051–1059, Feb. 2017, doi: 10.1016/J.SNB.2016.08.080.

[31] V. V. Ganbavle, S. V. Mohite, G. L. Agawane, J. H. Kim, and K. Y. Rajpure, “Nitrogen dioxide sensing properties of sprayed tungsten oxide thin film sensor: Effect of film thickness,” *J. Colloid Interface Sci.*, vol. 451, pp. 245–254, Aug. 2015, doi: 10.1016/J.JCIS.2015.04.001.

[32] E. Wajs, G. Rughoobur, K. Burling, A. George, A. J. Flewitt, and V. J. Gnanapragasam, “A novel split mode TFBAR device for quantitative measurements of prostate specific antigen in a small sample of whole blood,” *Nanoscale*, vol. 12, no. 17, pp. 9647–9652, May 2020, doi: 10.1039/D0NR00416B.

[33] J. Rosenbaum, *Bulk Acoustic Wave Theory and Devices*. Artech House, 1988.

[34] T. Mirea, J. Olivares, M. Clement, J. L. Olivera, J. Sangrador, and E. Iborra, “AlN-solidly mounted resonators sustaining up to 1000°C with TCF compensation,” *2017 Joint Conf. of the European Freq. and Time Forum and IEEE Intern. Freq. Control Symp., EFTF/IFC 2017 - Proceedings*, pp. 519–522, 2017, doi: 10.1109/FCS.2017.8088947.

[35] L. Yang, A. Marikutsa, M. Rumyantseva, E. Konstantinova, N. Khmelevsky, and A. Gaskov, “Quasi similar routes of NO_2 and NO sensing by nanocrystalline WO_3: Evidence by in situ DRIFT spectroscopy,” *Sensors (Switzerland)*, vol. 19, no. 15, Aug. 2019, doi: 10.3390/s19153405.

[36] T. Mirea, M. Clement, J. Olivares, and E. Iborra, “Assessment of the Absolute Mass Attachment to an AlN-Based Solidly Mounted Resonator Using a Single Shear Mode,” *IEEE Electron Device Lett.*, vol. 41, no. 4, pp. 609–612, Apr. 2020, doi: 10.1109/LED.2020.2976490.

[37] C. Bittencourt *et al.*, “Effects of Oxygen Partial Pressure and Annealing Temperature on the Formation of Sputtered Tungsten Oxide Films,” *J. Electrochem. Soc.*, vol. 149, no. 3, p. H81, 2002, doi: 10.1149/1.1448821.

[38] H. G. Moon *et al.*, "Extremely sensitive and selective NO probe based on villi-like WO_3 nanostructures for application to exhaled breath analyzers," *ACS Appl. Mater. Interfaces*, vol. 5, no. 21, pp. 10591–10596, Nov. 2013, doi: 10.1021/am402456s.

[39] L. Saadi, C. Lambert-Mauriat, V. Oison, H. Ouali, and R. Hayn, "Mechanism of NO_x sensing on WO_3 surface: First principle calculations," *Appl. Surf. Sci.*, vol. 293, pp. 76–79, Feb. 2014, doi: 10.1016/J.APSUSC.2013.12.095.

[40] L. Fan *et al.*, "Influence of surface conductivity on sensitivity of acoustic wave gas sensors based on multilayered structures," *IEEE Trans. Ultrason. Ferroelectr. Freq. Control*, vol. 58, no. 2, pp. 451–460, Feb. 2011, doi: 10.1109/TUFFC.2011.1822.

[41] S. H. Wang, C. Y. Shen, J. M. Su, and S. W. Chang, "A Room Temperature Nitric Oxide Gas Sensor Based on a Copper-Ion-Doped Polyaniline/Tungsten Oxide Nanocomposite," *Sensors*, vol. 15, no. 4, pp. 7084–7095, Mar. 2015, doi: 10.3390/S150407084.

[42] R. Hoffmann, M. Schreiter, and J. Heitmann, "The concept of thin film bulk acoustic resonators as selective CO_2 gas sensors," *J. of Sensors and Sensor Systems*, vol. 6, no. 1, pp. 87–96, Feb. 2017, doi: 10.5194/jsss-6-87-2017.

[43] M. Demiguel-Ramos *et al.*, "Tungsten oxide layers of high acoustic impedance for fully insulating acoustic reflectors," *IEEE Trans. Ultrason. Ferroelectr. Freq. Control*, vol. 63, no. 7, pp. 938–944, 2016, doi: 10.1109/TUFFC.2015.2498968.

5

CONCLUSIONS

The final goal of this work is summed up in its title: to design, fabricate and manufacture *AlN-based Solidly mounted resonator gas sensors for harsh environment applications*. However, this was broken down into several objectives, as stated at the end of Chapter 1. So, to summarize the findings throughout the original work presented and discussed in this thesis, it is interesting to analyze the conclusions obtained for each individual objective.

Study of the properties and behavior of the materials involved in the fabrication process.

- We performed a comparative study of the properties and performance of four fully dielectric acoustic reflector configurations: ZnO/SiO_2, Ta_2O_5/SiO_2, AlN/SiO_2 and HfN/SiO_2. All the configurations displayed good Q factor values, suitable for sensor applications. High temperature exposure deteriorated their performance, although maintaining acceptable performance. However, resonators on HfN/SiO_2 reflectors were the most affected and got destroyed in some cases. Mo/SiO_2 reflectors were also studied. This configuration displayed higher stability after high temperature exposure, which is why we concluded they were the most suitable for the manufacture of SMRs intended to work as gas sensors in high temperature environments.
- The electrodes of the resonators are an important component since they are employed for the electrical excitation of the piezoelectric film. For the bottom electrodes, Ir was the material of choice as it is a good substrate for sputtering of high quality AlN piezoelectric films. Top electrodes for high temperature operation were made of Mo/Au. The top Au thin film was sputtered as protective layer in sensing applications, since bare Mo

electrodes are highly sensitive to oxidation processes, especially at high temperatures.

- For sensing applications, we chose AlN as piezoelectric material. AlN-based resonators usually display higher Q factor values, which is essential in this type of application. Moreover, the piezoelectric films were deposited with high c-axis orientation so the resulting SMRs could present high quality longitudinal modes. Shear mode devices were manufactured to assess the performance of the different fully dielectric reflector configurations but were not required for sensor applications since in-liquid operation is out of the scope of this thesis.
- Additionally, we studied $Al_{0.7}Sc_{0.3}N$ thin films and their performance as piezoelectric materials in SMRs. Although some of the devices showed great piezoelectric performance, the observed Q factors and lack of stability after high temperature exposure do not make them better candidates for sensor applications than AlN films.

To have completely functional gas sensors, the final proposed task was to **study the potential functionalization layers and their integration in order to obtain already operating devices with good response for sensing applications:**

- Following an already established process, we were able to grow CNT forests on the top electrode of the SMRs via CVD technique. The outcome devices showed Q factors in the range of 50-350, making them suitable for sensing applications at room temperature.
- We employed thermal evaporation techniques to deposit pentacene thin films on the SMRs to act as functionalization layer. The resulting devices displayed Q factors in the 50-330 range, suitable for room temperature sensing applications.
- Finally, we developed a reproducible method of SMR functionalization with WO_3 thin films, sputtered at very low power and defined within the active layer of the Mo/Au top electrode by lift-off process. In order to enhance sensitivity to NO molecules, the films underwent annealing at final conditions of 350 °C for 12 hours, aiming to mitigate potential damage to the resonators. After this process, the observed Q factors of the SMR sensors stayed in the 100-300 range, making them suitable for high temperature sensing applications.

Design, development, and testing of a sensor characterization setup.

- We successfully developed a sensor characterization setup, provided with two chambers: one for low temperature and one for high temperature experiments. Each chamber receives input from four gas lines regulated by MFCs, supplying dry air, CO_2, and NO. The fourth gas line is employed in a bubbling system to produce humidity and/or VOC vapors. Considering the two chambers, the setup can operate in the -40 to 450 °C range.

Fabrication and characterization of SMR-based sensors for gas detection under harsh conditions.

- In the low temperature range, we tested dual mode SMRs to detect temperature and humidity changes. This configuration proved to be useful for discriminating temperature and humidity contributions to the observed frequency shifts. This behavior, initially tested at room temperature, was reproducible at temperatures below 0 °C, independently from the temperature variation to which the device is subjected.
- Regarding high temperature conditions, we demonstrated high sensitivity detection of NO achieved with AlN-based SMRs functionalized with sputtered WO_3 thin films. Film thicknesses from 190 nm to 330 nm were tested in the 200 to 350 °C range. All devices demonstrated sensitivity to NO, with the highest measured values of 5.32 kHz/ppm and 5.48 kHz/ppm for resonant and anti-resonant frequencies, respectively. These peak sensitivities were observed in sensors featuring 220 nm thick WO_3 films at 200 °C. The achieved sensitivities, showing good linearity upon exposure to various analyte concentrations, enable sub-ppm range detection, which is in the state of the art within NO chemical sensors at high temperatures. Concerning sensing mechanisms, the study revealed that the frequency shifts caused by NO adsorption could not be explained by a purely gravimetric approach, but rather by a change in the elastic properties of the sensing layer. In this case, the adsorbed molecules increased the acoustic longitudinal velocity of the material, inducing a positive frequency shift used to detect the target gas.

Although beyond the main scope of the thesis, yet in agreement with its thematic focus, we also conducted some gas sensor characterization experiments at room temperature, leading to the following conclusions:

- We detected ethanol vapor using SMRs functionalized with CNT forests, enhancing the device's sensitivity by almost 5 times. This experiment also served the extra purpose of verifying the completion of a primary thesis objective: the successful construction and operation of a gas sensor characterization setup.
- Using pentacene functionalized SMRs, we were able to detect NO concentrations of 33.3 ppm at room temperature. The sensors exhibited a net sensitivity towards the analyte of 0.88 kHz/ppm.

6

FUTURE WORK

The objectives proposed for this thesis are a consequence of the previous research carried out by our group. In the same way, the work conducted to achieve these objectives can lead to new research. The envisioned research lines further explore optimization of processes and integration of new materials for the already studied devices. Moreover, some of the suggested lines are intended to combine tools from other fields of knowledge to enhance the properties of the sensors and to bring them closer to a state of market readiness.

The suggested lines are:

- **Optimization of dielectric acoustic reflectors.** Conduct further experiments to optimize manufacturing processes and improve Q factor values of the resonators, which would help delivering better sensor performance. Start testing processes of SMR sensors on dielectric acoustic reflectors at high temperatures.
- **Electrode materials for high temperature applications.** Conduct an extensive study of diverse electrode materials, such as Pt and alloys tailored for high-temperature sensor applications [1]–[3]. Perform a comparative analysis, specifically focusing on the already developed Mo/Au electrodes, to point out which materials show superior performance in high temperature environments.
- **Comparative analysis of AlN vs AlScN based SMR sensors.** Perform a detailed comparative study between AlN and AlScN based SMR sensors. Explore their respective advantages and limitations, considering factors such as sensitivity, stability, and response characteristics under different environmental conditions.
- **Optimization of WO_3 annealing process.** Study of the annealing times and temperatures influence in the performance of the sensors. The ideal

outcome of this study would be to reach shorter annealing times without compromising the performance, since the already proposed ones are hardly compatible with fabrication routes at an industrial level.

- **Additional functionalization steps for CNT forests.** Implement extra functionalization steps for CNT forests to make them suitable for both high and low-temperature sensing applications [4], [5]. For instance, explore the decoration of CNTs with nanoparticles (NPs) to enhance their sensing capabilities.
- **Functionalization layers for high temperature applications.** In parallel to the optimization of WO_3 layers for NO_x detection, extend the study of functionalization layers to other gases at high temperatures, such as CO and CO_2. Explore new materials and surface treatments to develop sensors with increased sensitivity and selectivity towards these specific gases.
- **Electronic readout circuit development.** From a final prototype perspective, the sensor should incorporate dedicated readout electronics to streamline device usage. Designing electronic circuits for high frequencies and high temperature environments can suppose a significant challenge. Various designs will be explored, covering options based on oscillators with Pierce or Colpitts topologies [6]. The objective is to develop two types of readout circuits: one relying on discrete components and another utilizing silicon chips with CMOS technology. After integration of the sensor and electronics, the characterization of the final sensing configuration will be possible, especially in terms of resolution and LOD.
- **Packaging of SMR gas sensors.** Progress to the packaging phase for already functional SMR sensors. This process will be addressed first for the individual sensor and then for the sensor and electronic readout system. To ensure practical application of the sensors, durability, environmental protection, and long-term stability will be considered. Additional specifications for high temperature applications will be required.
- **Integration of Machine/Deep Learning models.** Develop advanced Machine/Deep Learning tools to improve sensor properties such as sensitivity, selectivity, and limit of detection. Generate a database consisting of sensor response measurements under different

environmental conditions and gas concentrations. Then, perform the training and optimization phase for carefully selected models, complying with the possible specifications of each model in terms of data pre-processing. Some of the potential models are Gradient Boosting and random tree-based models, as well as recurrent and convolutional neural networks [7]. For cross-sensitivity studies, clustering algorithms like KNN and K-means will be explored [8].

And of course, the final goal is to continuously explore and integrate new research directions as these studies progress, adapting the focus based on emerging materials, technologies, and applications in the field of sensor technology.

References

[1] D. Richter, S. Sakharov, E. Forsén, E. Mayer, L. Reindl, and H. Fritze, "Thin Film Electrodes for High Temperature Surface Acoustic Wave Devices," *Procedia Eng.*, vol. 25, pp. 168–171, Jan. 2011, doi: 10.1016/J.PROENG.2011.12.042.

[2] F. Liu *et al.*, "High-temperature NO_2 gas sensor based on stabilized zirconia and $CoTa_2O_6$ sensing electrode," *Sens. Actuators B Chem.*, vol. 240, pp. 148–157, Mar. 2017, doi: 10.1016/J.SNB.2016.08.134.

[3] E. Çiftyürek, K. Sabolsky, and E. M. Sabolsky, "Platinum thin film electrodes for high-temperature chemical sensor applications," *Sens. Actuators B Chem.*, vol. 181, pp. 702–714, 2013, doi: 10.1016/j.snb.2013.02.058.

[4] J. Xiang, A. Singhal, R. Divan, L. Stan, Y. Liu, and I. Paprotny, "Selective volatile organic compound gas sensor based on carbon nanotubes functionalized with ZnO nanoparticles," *J. of Vacuum Sci. & Tech. B*, vol. 39, no. 4, p. 042803, Jul. 2021, doi: 10.1116/6.0000992.

[5] A. Abdelhalim, M. Winkler, F. Loghin, C. Zeiser, P. Lugli, and A. Abdellah, "Highly sensitive and selective carbon nanotube-based gas sensor arrays functionalized with different metallic nanoparticles," *Sens. Actuators B Chem.*, vol. 220, pp. 1288–1296, Dec. 2015, doi: 10.1016/j.snb.2015.06.138.

[6] J.-Y. Park and J.-W. Choi, "Review—Electronic Circuit Systems for Piezoelectric Resonance Sensors," *J. Electrochem. Soc.*, vol. 167, no. 3, p. 037560, Jan. 2020, doi: 10.1149/1945-7111/ab6cf7.

[7] V. Corsino, V. Ruiz-Díez, J. M. Gilpérez, M. Ramírez-Palma, and J. L. Sánchez-Rojas, "Machine learning techniques for the estimation of viscosity and density of aqueous solutions in piezo-actuated 3D-printed cells," *Sens. Actuators A Phys.*, vol. 363, p. 114694, Dec. 2023, doi: 10.1016/J.SNA.2023.114694.

[8] P. E. Jebarani, N. Umadevi, H. Dang, and M. Pomplun, "A Novel Hybrid K-Means and GMM Machine Learning Model for Breast Cancer Detection," *IEEE Access*, vol. 9, pp. 146153–146162, 2021, doi: 10.1109/ACCESS.2021.3123425.